

Summer 2014

# Experimental characterization of the PT asymmetry with balanced inflow and outflow at different Reynolds numbers

Zijie Qu  
*Purdue University*

Follow this and additional works at: [https://docs.lib.purdue.edu/open\\_access\\_theses](https://docs.lib.purdue.edu/open_access_theses)



Part of the [Mechanical Engineering Commons](#)

---

## Recommended Citation

Qu, Zijie, "Experimental characterization of the PT asymmetry with balanced inflow and outflow at different Reynolds numbers" (2014). *Open Access Theses*. 670.

[https://docs.lib.purdue.edu/open\\_access\\_theses/670](https://docs.lib.purdue.edu/open_access_theses/670)


This document has been made available through Purdue e-Pubs, a service of the Purdue University Libraries. Please contact [epubs@purdue.edu](mailto:epubs@purdue.edu) for additional information.

**PURDUE UNIVERSITY  
GRADUATE SCHOOL  
Thesis/Dissertation Acceptance**

This is to certify that the thesis/dissertation prepared

By Qu, Zijie

Entitled  
EXPERIMENTAL CHARACTERIZATION OF THE PT ASYMMETRY WITH  
BALANCED INFLOW AND OUTFLOW AT DIFFERENT REYNOLDS NUMBERS

For the degree of Master of Science in Mechanical Engineering 

Is approved by the final examining committee:

Jun Chen

Paul E. Sojka

Huidan (Whitney) Yu

\_\_\_\_\_

\_\_\_\_\_

\_\_\_\_\_

\_\_\_\_\_

\_\_\_\_\_

To the best of my knowledge and as understood by the student in the *Thesis/Dissertation Agreement, Publication Delay, and Certification/Disclaimer (Graduate School Form 32)*, this thesis/dissertation adheres to the provisions of Purdue University's "Policy on Integrity in Research" and the use of copyrighted material.

Jun Chen

Approved by Major Professor(s): \_\_\_\_\_

\_\_\_\_\_

Approved by: David Anderson 05/08/2014

Head of the Department Graduate Program

Date



EXPERIMENTAL CHARACTERIZATION OF THE  $\mathcal{PT}$  ASYMMETRY WITH  
BALANCED INFLOW AND OUTFLOW AT DIFFERENT REYNOLDS  
NUMBERS

A Thesis

Submitted to the Faculty

of

Purdue University

by

Zijie Qu

In Partial Fulfillment of the

Requirements for the Degree

of

Master of Science in Mechanical Engineering

August 2014

Purdue University

West Lafayette, Indiana

To my family

## ACKNOWLEDGMENTS

First and foremost, I would like to thank my advisor, Dr. Jun Chen, for giving this wonderful opportunity to me and fostering my intellectual growth throughout my time at Purdue University. The preliminary computational results of this work is done by Dr. Whitney Yu and her students and I would like to express my deepest gratitude to all of the people working in Dr. Yu's research team especially to Xi Chen who has helped me understand the project better.

I would also like to thank Dr. Paul E. Sojka for serving on my advisory committee and of course I would like to thank my labmates. Jian, Fangyuan, Nicholas and Weichao have been with me and I thank you all for the discussions about experimental fluid dynamics. Thank you also to Xiongfeng, Lingxuan, Yucheng, Wenbin and Yixuan for your friendship and assistance. I owe a huge thank you to my parents, Ying and Chunsheng, who always encouraged me and taught me that I can finish any tough job as long as I insist.

Finally, the biggest thank you of all goes to Ying. You have been with me and encourage me when times were easy and difficult. Your support means the world to me.

## TABLE OF CONTENTS

	Page
LIST OF TABLES . . . . .	vi
LIST OF FIGURES . . . . .	vii
SYMBOLS . . . . .	ix
ABBREVIATIONS . . . . .	xi
ABSTRACT . . . . .	xii
1. INTRODUCTION . . . . .	1
1.1 Operators in Quantum Mechanics . . . . .	1
1.1.1 Linear Operator . . . . .	1
1.1.2 Eigenvalues and Eigenfunctions of Operators . . . . .	1
1.1.3 Fundamental Operators . . . . .	2
1.1.4 Hamiltonian . . . . .	2
1.1.5 Hermitian . . . . .	4
1.1.6 The Commutation of Operators . . . . .	6
1.2 $\mathcal{PT}$ Quantum Theory . . . . .	7
1.2.1 Fundamentals of $\mathcal{PT}$ Quantum Theory . . . . .	7
1.2.2 $\mathcal{PT}$ -Symmetric Hamiltonian . . . . .	9
1.3 Background of $\mathcal{PT}$ -Symmetric Experiment . . . . .	11
1.3.1 $\mathcal{PT}$ Symmetry Breaking in Complex Optical Potentials . . . . .	12
1.3.2 Stochastic $\mathcal{PT}$ -symmetric Coupler . . . . .	13
1.3.3 $\mathcal{PT}$ -Symmetries in Active LRC Circuits . . . . .	14
1.3.4 $\mathcal{PT}$ Phase Transition in Mechanical System . . . . .	14
1.3.5 $\mathcal{PT}$ Asymmetry in Viscous Fluid with Balanced Inlet/Outlet Flow . . . . .	15
1.4 Motivation . . . . .	16
1.5 $\mathcal{PT}$ -symmetric Fluid System . . . . .	17
2. EXPERIMENTAL FACILITY . . . . .	22
2.1 Test Section . . . . .	22
2.1.1 Inlet/Outlet Tubing Design . . . . .	23
2.2 Syringe Pump . . . . .	24
2.2.1 Pumping Flow Rate Calculation . . . . .	24
3. INSTRUMENTATION . . . . .	33
3.1 Fundamentals of Particle Image Velocimetry . . . . .	33

	Page
3.1.1 Image Acquisition . . . . .	34
3.1.2 Image Processing . . . . .	34
3.1.3 Post-Processing . . . . .	35
3.2 Continuous PIV System . . . . .	36
3.2.1 High-Speed CMOS Camera . . . . .	37
3.2.1.1 Software Development . . . . .	39
3.2.2 Frame Rate Estimation . . . . .	41
3.3 Pulsed PIV System . . . . .	42
3.3.1 Nd:YAG Laser . . . . .	43
3.4 Optical System . . . . .	44
3.5 Measuring Velocity Field using PIV . . . . .	46
4. FLOW FIELD WITH SYMMETRIC INLET AND OUTLET . . . . .	58
4.1 Formalism . . . . .	58
4.2 Results . . . . .	62
4.3 Discussion . . . . .	64
5. $\mathcal{PT}$ -SYMMETRIC FLOW FIELD WITH MAIN FLOW . . . . .	86
5.1 Experimental Condition . . . . .	86
5.2 Formalism . . . . .	87
5.3 Results . . . . .	88
5.4 Discussion . . . . .	89
6. SUMMARY AND CONCLUSIONS . . . . .	106
6.1 Overview of Experiments and Discussion . . . . .	106
6.2 Recommendation for Future Research . . . . .	107
LIST OF REFERENCES . . . . .	109
APPENDIX . . . . .	112



## LIST OF TABLES

Table	Page
2.1 Geometry of the test section. . . . .	26
2.2 Geometry of the inlet/outlet tubing. . . . .	26
2.3 Entrance lengths at different Reynolds numbers. . . . .	26
2.4 Volumetric flow rates and averaged velocities at different Reynolds numbers. . . . .	27
3.1 Fps for different Reynolds number. . . . .	47
3.2 Focal length for lenses using in the experiment. . . . .	47
3.3 Focal length ( $F_{total}$ ) and laser sheet length at distance $F_{total}$ of optical system. . . . .	47
5.1 Boundary condition for $\mathcal{PT}$ -symmetric flow field with main flow. . . . .	90
5.2 Fitting constant for velocity asymmetry about y-axis. . . . .	91
5.3 Fitting constant for velocity asymmetry to origin. . . . .	91
5.4 Fitting constant for vorticity asymmetry about y-axis. . . . .	91
5.5 Fitting constant for vorticity asymmetry to origin. . . . .	92
5.6 Fitting constant for kinetic energy asymmetry about y-axis. . . . .	92
5.7 Fitting constant for kinetic energy asymmetry to origin. . . . .	92

## LIST OF FIGURES

Figure	Page
1.1 Energy levels of the Hamiltonian $\mathcal{H} = p^2 + x^2(ix)^\varepsilon$ as a function of parameter $\varepsilon$ [2]. . . . .	19
1.2 Demonstration of $\mathcal{PT}$ -symmetric flow field. . . . .	20
1.3 The power law scaling between asymmetries and Reynolds number from preliminary computational results [19]. . . . .	21
2.1 Schematics of the system, (a)Without main flow, (b)With main flow. . .	28
2.2 Schematics of test section. . . . .	32
3.1 Experimental arrangement for particle image velocimetry [23]. . . . .	48
3.2 PIV double exposure recording process: (top) particle patterns moving at displacement $(U, V)$ , and (bottom) particle pattern images recorded by the digital camera [51]. . . . .	49
3.3 Single frame/multi-exposure PIV [23]. . . . .	50
3.4 Multi-frame/single exposure PIV [23]. . . . .	51
3.5 Sample pair of interrogation windows and the corresponding distribution of the cross correlation function $\phi(m, n)$ [51]. . . . .	52
3.6 Schematics for pulsed PIV system. PTU stands for Programmable Timing Unit. $L_1$ is “Flashlamp” trigger for laser 1, $Q_1$ is the “Q-switch” trigger for laser 1; $L_2$ is “Flashlamp” trigger for laser 2, $Q_2$ is the “Q-switch” trigger for laser 2. . . . .	53
3.7 Typical layout of a dual oscillator Nd:YAG. rod1, rod2: laser crystal, M1, M2, M3: mirrors, P: beam combining polarizer, SHG: second harmonic generator [46]. . . . .	54
3.8 The Q-Switch allows the cavity to resonate in the most energetic point during the flashlamp cycle [46]. . . . .	55
3.9 Intensity profile of a Gaussian beam. . . . .	56
3.10 Schematics of optical system. . . . .	57
4.1 Two distinct balanced inflow/outflow system. . . . .	65
4.2 Coordinate system data analysis. . . . .	66

Figure	Page
4.3 Snapshots of velocity fields, (a)Re=60, (b)Re=600. . . . .	67
4.4 Velocity fields and streamlines for different Reynolds numbers, (a)Re=60, (b)Re=80, (c)Re=100, (d)Re=200, (e)Re=300, (f)Re=400, (g)Re=500, (h)Re=600, (i)Re=700. . . . .	68
4.5 Vorticity fields for different Reynolds numbers, (a)Re=60, (b)Re=80, (c)Re=100, (d)Re=200, (e)Re=300, (f)Re=400, (g)Re=500, (h)Re=600, (i)Re=700. . . . .	73
4.6 Kinetic energy fields for different Reynolds numbers, (a)Re=60, (b)Re=80, (c)Re=100, (d)Re=200, (e)Re=300, (f)Re=400, (g)Re=500, (h)Re=600, (i)Re=700. . . . .	78
4.7 Velocity asymmetry at different Reynolds number. . . . .	83
4.8 Vorticity asymmetry at different Reynolds number. . . . .	84
4.9 Kinetic energy asymmetry at different Reynolds number. . . . .	85
5.1 Snapshots for velocity field with main flow, (a) Main flow individually Re=500, (b) Symmetric flow Re=300 combined with main flow Re=500. . . . .	93
5.2 Velocity field, vorticity field and kinetic energy field of main flow at Reynolds number 500, (a1)Velocity field, (a2)Vorticity field, (a3)Kinetic energy field. . . . .	94
5.3 Velocity field, vorticity field and kinetic energy field of combined flow, main flow Re=500, symmetric inflow and outflow Re=300, (b1)Velocity field, (b2)Vorticity field, (b3)Kinetic energy field. . . . .	96
5.4 Velocity field, vorticity field and kinetic energy field subtracted flow, (c1)Velocity field, (c2)Vorticity field, (c3)Kinetic energy field. . . . .	98
5.5 Velocity asymmetry for $\mathcal{PT}$ -symmetric flow field with main flow. . . . .	100
5.6 Vorticity asymmetry for $\mathcal{PT}$ -symmetric flow field with main flow. . . . .	102
5.7 Kinetic energy asymmetry for $\mathcal{PT}$ -symmetric flow field with main flow. . . . .	104

## SYMBOLS

<b>Symbol</b>	<b>Description</b>
$m$	Mass ( $kg$ )
$U$	Velocity ( $m/s$ )
$\mu$	Viscosity ( $Pas$ )
$\rho$	Density ( $kg/m^3$ )
$\mathcal{H}$	Hamiltonian
$\mathcal{PT}$	Combined parity reflection and time reversal
$\hat{V}$	Potential energy operator
$\hat{T}$	Kinetic energy operator
$\hat{p}$	Momentum operator
$\hbar$	Planck's constant
$i$	Imaginary symbol
$\lambda$	Eigenvalue
$W$	Inlet/outlet tubing width
$U_p$	Averaged velocity
$\phi$	Eigenfunction
$\Delta t$	Time difference
$\rho_{\mathcal{PT}}$	$\mathcal{PT}$ -symmetric transition number
$Re$	Reynolds number
$Le$	Entrance length
$d$	Diameter
$Q$	Volumetric flow rate
$A$	Area
$L$	Characteristic length
$s$	Object distance

<b>Symbol</b>	<b>Description</b>
$s'$	Image distance
$f$	Focal length
$F_{total}$	Focal length of the optical system
$\mathcal{P}_O$	Odd parity operator
$\mathcal{P}_y$	Even parity operator
$\rho^u$	Velocity asymmetry number
$\rho^K$	Kinetic energy asymmetry number
$\rho^\omega$	Vorticity asymmetry number

## ABBREVIATIONS

<b>Abbreviation</b>	<b>Description</b>
PIV	Particle image velocimetry
fps	Frames per second
LDV	Laser Doppler Velocimetry
PTU	Programmable Timing Unit
CCD	Charge-coupled Device
CMOS	Complementary Metal Oxide Semiconductor
GB	Gigabyte
MB	Megabyte
SATA	Serial Advanced Technology Attachment
RAM	Random-Access Memory
MIL	Matrox Imaging Library
DCF	Digital configuration file
PC	Personal computer

## ABSTRACT

Qu, Zijie M.S.M.E, Purdue University, August 2014. Experimental characterization of the  $\mathcal{PT}$  asymmetry with balanced inflow and outflow at different Reynolds numbers. Major Professor: Jun Chen, School of Mechanical Engineering, School of Mechanical Engineering.

This research focused on characterizing the  $\mathcal{PT}$  asymmetry with balanced inflow and outflow conditions at different Reynolds number using experimental method. The characterization process utilized PIV data to explore the relationship between  $\mathcal{PT}$  asymmetry and Reynolds number in two different experiments. In the first experiment, balanced inflow and outflow are used to generate the flow field in a cuboid test section with different Reynolds number, the inflow and outflow are located at the central of left side and right side of the test section. In the second experiment, a main flow is introduced to the first experiment by adding another inflow and outflow which locate at a symmetric position on the bottom side of the test section. The flow field is generated by the two inflows and outflows with different Reynolds number. The results show that there is a linear relationship between  $\mathcal{PT}$  asymmetry and Reynolds number when Reynolds number is less than 200 for a balanced inflow/outflow situation. They also show that there is a decreasing trend of  $\mathcal{PT}$  asymmetry when Reynolds number increases for balanced inflow/outflow combined with main flow.

## 1. INTRODUCTION

### 1.1 Operators in Quantum Mechanics

#### 1.1.1 Linear Operator

An operator  $\hat{A}$  is a linear operator as long as it satisfies that

$$\hat{A}(cf(x)) = c\hat{A}f(x) \quad (1.1)$$

and

$$\hat{A}(f(x) + g(x)) = \hat{A}f(x) + \hat{A}g(x) \quad (1.2)$$

where  $c$  is a complex constant, and  $f(x)$  and  $g(x)$  are two properly defined function.

#### 1.1.2 Eigenvalues and Eigenfunctions of Operators

An operator is simply defined as a mathematical symbol and as it is applied to a function, a new function will be generated. For instance, if we have an operator  $\hat{A}$  and a function  $f(x)$ , then a new function  $g(x)$  could be defined as

$$g(x) = \hat{A}(f(x)). \quad (1.3)$$

In some a special case where the function  $g(x)$  is proportional to  $f(x)$ , we have

$$g(x) = \lambda f(x) \rightarrow \hat{A}(f(x)) = \lambda f(x) \quad (1.4)$$

where  $\lambda$  is a constant. In this case  $f(x)$  is the eigenfunction of the operator  $\hat{A}$  and  $\lambda$  is the corresponding eigenvalue.



### 1.1.3 Fundamental Operators

There are two fundamental operators in quantum mechanics. One is the position operator  $\hat{r}$ , in three-dimensional case the operator  $\hat{r}$  is defined as

$$\hat{r}\psi = \mathbf{r}\psi. \quad (1.5)$$

Here  $\psi$  is the wave function which is a function of position vector  $\mathbf{r}$  and time  $t$ ,  $\psi = \psi(\mathbf{r}, t)$ . The position operator is the operator that corresponds to the position observable of a particle. The eigenvalue of the operator is the position vector of the particle.  $\hat{x}$ ,  $\hat{y}$  and  $\hat{z}$  are denoted as position operators for a wave function in x, y and z direction separately. Another one is the momentum operator  $\hat{p}$  which is defined as

$$\hat{p} = -i\hbar \nabla. \quad (1.6)$$

Here  $\nabla$  is the gradient operator. The momentum operator acts on the wave function will extract the momentum eigenvalue which is the momentum vector a particle would have when measured in an experiment.

### 1.1.4 Hamiltonian

In quantum mechanics, the Hamiltonian  $\mathcal{H}$  is the operator corresponding to the total energy, including kinetic energy of all particles and potential energy of the particles associated with the system. The Hamiltonian is different for different situation or different number of particles because it includes the kinetic energy of all particles and the potential energy is also different under different situation. The spectrum of  $\mathcal{H}$  is the set of possible outcomes when one measures the total energy of a system. Since it relates closely to the time-evolution of a system, Hamiltonian is of the fundamental importance in most formulations of quantum theory [8,9,10].

For a system that contains only one particle, the Hamiltonian  $\mathcal{H}$  could be represented by

$$\mathcal{H} = \hat{V} + \hat{T}. \quad (1.7)$$

$\hat{V}$  is the potential energy operator and could be further represented by

$$\hat{V} = \hat{V}(\mathbf{r}, t) \quad (1.8)$$

and  $\hat{T}$  is the kinetic energy operator.

$$\hat{T}(\mathbf{r}, t) = \frac{\hat{p}^2}{2m} = -\frac{\hbar^2}{2m} \nabla^2. \quad (1.9)$$

Here  $m$  is the mass of the particle and  $\hat{p}$  is the momentum operation. Combine the equations together will lead to

$$\mathcal{H} = -\frac{\hbar^2}{2m} \nabla^2 + \hat{V}(\mathbf{r}, t). \quad (1.10)$$

The dot product of  $\nabla$  with itself is the Laplacian  $\nabla^2$ . In three-dimensional Cartesian system the Laplace operator is

$$\nabla^2 = \frac{\partial^2}{\partial x^2} + \frac{\partial^2}{\partial y^2} + \frac{\partial^2}{\partial z^2}. \quad (1.11)$$

In addition, for a system that contains  $N$  particles ( $N > 1$ ) instead of a single one the Hamiltonian  $\mathcal{H}$  is

$$\mathcal{H} = \sum_{i=1}^N \hat{T}_i + \hat{V} \quad (1.12)$$

where

$$\hat{V} = \hat{V}(\mathbf{r}_1, \mathbf{r}_2 \cdots \mathbf{r}_N, t), \quad (1.13)$$

is the potential energy function, now a function of the spatial configuration of the system and time and

$$\hat{T}_i = \frac{\hat{p}_i^2}{2m_i} = -\frac{\hbar^2}{2m_i} \nabla_i^2 \quad (1.14)$$

is the kinetic energy of the  $i$ -th particle of the system where  $m_i$  is the mass of the  $i$ -th particle,  $\hat{p}_i$  is the momentum operator for  $i$ -th particle.  $\nabla_i$  is the gradient for particle  $i$ ,  $\nabla_i^2$  is the Laplacian for particle using the coordinates:

$$\nabla_i^2 = \frac{\partial^2}{\partial x_i^2} + \frac{\partial^2}{\partial y_i^2} + \frac{\partial^2}{\partial z_i^2}. \quad (1.15)$$

Combine these together yields the Hamiltonian for a system contains  $N$  particles.

$$\mathcal{H} = - \sum_{i=1}^N \frac{\hbar^2}{2m_i} \nabla_i^2 + \hat{V}(\mathbf{r}_1, \mathbf{r}_2 \cdots \mathbf{r}_N, t). \quad (1.16)$$

Finally the eigenvalues of  $\mathcal{H}$  is the energy spectrum of the system and this can be shown in form

$$\mathcal{H}\psi_i = E_i\psi_i \quad (1.17)$$

where the specific values of energy is called energy eigenvalues.

### 1.1.5 Hermitian

Hermitian operator is another important operator widely used in quantum mechanics. An operator  $\hat{A}^\dagger$  is the Hermitian conjugate or adjoint of  $\hat{A}$  as long as

$$\int (\hat{A}^\dagger \psi)^* \psi dr = \int \psi^* \hat{A} \psi dr. \quad (1.18)$$

(Note: Here the operator  $*$  denotes the complex conjugate.) An operator  $\hat{A}$  could be called Hermitian if

$$\int (\hat{A} \psi)^* \psi dr = \int \psi^* \hat{A} \psi dr. \quad (1.19)$$

One can prove that operator  $\hat{r}$  is Hermitian, i.e.

$$\int (\hat{r} \psi)^* \psi dx = \int (\mathbf{r} \psi)^* \psi dx = \int \psi^* \mathbf{r} \psi dx = \int \psi^* \hat{r} \psi dx. \quad (1.20)$$

Here we consider a one-dimensional case and the result remains the same for three-dimensional case. In addition one can prove that the momentum operator  $\hat{p}$  is also Hermitian (one-dimensional case),

$$\int (\hat{p}\psi)^*\psi dx = \int (-i\hbar \frac{d\psi}{dx})^*\psi dx = i\hbar \int (\frac{d\psi}{dx})^*\psi dx = i\hbar([\psi^*\psi] - \int \frac{d\psi}{dx}\psi^* dx). \quad (1.21)$$

Now notice that after integration by parts the first term on right hand side tends to 0 as  $x$  approaches to infinite because wave functions of finite systems vanish at  $x = \pm\infty$ . Then the right hand side yields

$$-i\hbar \int \psi^* \frac{d\psi}{dx} dx = \int \psi^* \hat{p}\psi dx. \quad (1.22)$$

Therefore, operator  $\hat{p}$  is Hermitian.

In addition, the kinetic energy operator  $\hat{T}$  can also be proven to be Hermitian.

$$\int (\hat{T}\phi)^*\phi dx = \frac{1}{2m} \int (\hat{p}^2\phi)^*\phi dx = \frac{1}{2m} \int \phi^* \hat{p}^2\phi dx = \int \phi^* \hat{T}\phi dx. \quad (1.23)$$

$\hat{r}$  is Hermitian and several functions like  $1/r$  that depend on them and which appear as potential energy terms in the Hamiltonian is also Hermitian. Although this is not a complete argument its results strongly suggest that the Hamiltonian operator is Hermitian and it is commonly believed that the Hamiltonian must be Hermitian in order to ensure that the energy spectrum (the eigenvalues of the Hamiltonian) is real. To prove that the eigenvalues of Hermitian operators are real, first we assume that  $\phi$  is an eigenfunction of  $\hat{A}$  with eigenvalue  $\lambda$

$$\hat{A}\phi = \lambda\phi, \quad (1.24)$$

then we have

$$\int (\hat{A}\phi)^*\phi dx = \int (\lambda\phi)^*\phi dx = \lambda^* \int \phi^*\phi dx, \quad (1.25)$$

when  $\hat{A}$  is Hermitian, we also have

$$\int (\hat{A}\phi)^* \phi dx = \int \phi^* \hat{A}\phi dx = \lambda \int \phi^* \phi dx, \quad (1.26)$$

thus

$$(\lambda^* - \lambda) \int \phi^* \phi dx = 0, \quad (1.27)$$

and since  $\int \phi^* \phi dx \neq 0$ , we will have

$$\lambda^* - \lambda = 0 \leftrightarrow \lambda^* = \lambda \quad (1.28)$$

which indicates that  $\lambda$  is purely real.

Therefore, the eigenvalues of Hamiltonian  $\mathcal{H}$  is real. In fact, since Hamiltonian describes the energy level of a system so the eigenvalues of Hamiltonian  $\mathcal{H}$  are the energies of the system described by the wave function [11].

### 1.1.6 The Commutation of Operators

First of all, the product of two operators should be defined before the commutation is introduced. Let the operators be  $\hat{A}$  and  $\hat{B}$ , and let them operate on a function  $f(x)$  (one-dimensional for simplicity of notation). Then the expression

$$\hat{A}\hat{B}(f(x)) \quad (1.29)$$

is a new function. Therefore, by the definition of operators,  $\hat{A}\hat{B}$  is an operator which can be denoted by  $\hat{C}$ :  $\hat{C}$  is the product of  $\hat{A}$  and  $\hat{B}$ . The meaning of  $\hat{A}\hat{B}f(x)$  should be that  $\hat{B}$  is first operating on  $f(x)$ , giving a new function, and then  $\hat{A}$  is operating on that new function.

In quantum mechanics the commutator of  $\hat{A}$  and  $\hat{B}$  is defined as

$$[\hat{A}, \hat{B}] \equiv \hat{A}\hat{B} - \hat{B}\hat{A}. \quad (1.30)$$

If  $[\hat{A}, \hat{B}] \neq 0$ , then one says that  $\hat{A}$  and  $\hat{B}$  do not commute, if  $[\hat{A}, \hat{B}] = 0$ , then  $\hat{A}$  and  $\hat{B}$  are said to commute with each other. For a one-dimensional case one can prove that

$$[\hat{x}, \hat{p}](f(x)) = (\hat{x}\hat{p} - \hat{p}\hat{x})(f(x)) = -i\hbar\left(x\frac{df(x)}{dx} - \frac{d}{dx}(xf(x))\right) \quad (1.31)$$

and hence by product rule of differentiation:

$$[\hat{x}, \hat{p}](f(x)) = i\hbar f(x), \quad (1.32)$$

and this equation yields

$$[\hat{x}, \hat{p}] = i\hbar. \quad (1.33)$$

This is the canonical commutation relation and it is the fundamental relation in quantum mechanics.

## 1.2 $\mathcal{PT}$ Quantum Theory

### 1.2.1 Fundamentals of $\mathcal{PT}$ Quantum Theory

$\mathcal{PT}$  denotes a combined parity reflection and time reversal operation and  $\mathcal{PT}$  quantum theory is recently seen in many papers. Ordinarily, the sufficient condition to ensure that the Hamiltonian  $\mathcal{H}$  has a real energy spectrum (the eigenvalues of  $\mathcal{H}$ ) is that  $\mathcal{H}$  is Hermitian. It is true that this condition of Hermiticity is sufficient to guarantee the desired properties, it is not necessary. The physical basis of this condition is obscure since it is only a mathematical condition. Recent researches pointed out that this Hermitian condition could be replaced by a weaker and more physical requirement  $\mathcal{H} = \mathcal{H}^{**}$ . \*\* denotes a time reversal combined with parity reflection  $\mathcal{PT}$ , i.e. space-time reflection. The complex Hamiltonian whose energy spectrum under this  $\mathcal{PT}$  symmetric condition are still real and positive. This condition also leads to a probability that a non-Hermitian complex Hamiltonian could have a real and positive eigenvalues. In addition, by using this new  $\mathcal{PT}$ -symmetric condition

an infinite number of Hamiltonian could be constructed which would be rejected in past since they were not Hermitian. Take  $\mathcal{H} = p^2 + ix^3$  as an example. It should be emphasized that this new condition does not conflict with the traditional Hermitian condition or regard it as a wrong condition. Rather,  $\mathcal{PT}$ -symmetric brings us a new aspect of studying quantum mechanics [6].

To start with, the basic properties of  $\mathcal{P}$  and  $\mathcal{T}$  operators are introduced. In  $\mathcal{PT}$ -symmetric operation,  $\mathcal{P}$  stands for the parity reflection (space reflection) and  $\mathcal{T}$  stands for time reversal. These operators are defined by their action on position ( $\mathbf{x}$ ) and momentum ( $\mathbf{p}$ ) [6].

$$\mathcal{P} : \mathbf{x} \rightarrow -\mathbf{x}, \mathbf{p} \rightarrow -\mathbf{p}; \quad (1.34)$$

$$\mathcal{T} : \mathbf{x} \rightarrow \mathbf{x}, \mathbf{p} \rightarrow -\mathbf{p}; i \rightarrow -i. \quad (1.35)$$

Note that the operator  $\mathcal{T}$  changes the sign of  $i$  and it preserves the fundamental commutation relation of quantum mechanics between  $\hat{x}$  and  $\hat{p}$ ,  $[\hat{x}, \hat{p}] = i\hbar$ , like  $\mathcal{P}$  does. One can prove this by

$$[-\hat{x}, -\hat{p}] = (-\hat{x})(-\hat{p}) - (-\hat{p})(-\hat{x}) = [\hat{x}, \hat{p}] = i\hbar; \quad (1.36)$$

$$[\hat{x}, -\hat{p}] = (\hat{x})(-\hat{p}) - (-\hat{p})(\hat{x}) = -[\hat{x}, \hat{p}] = -i\hbar. \quad (1.37)$$

This is known as Heisenberg algebra. Moreover, when  $\hat{x}$  and  $\hat{p}$  are real, the canonical commutation relation  $[\hat{x}, \hat{p}] = i\hbar$  remains the same under both time reversal and parity reflection. Even if  $x$  and  $p$  are not purely real it could be proved that the canonical commutation relation could still be invariant under  $\mathcal{PT}$  operation. If the position ( $\mathbf{x}$ ) and momentum ( $\mathbf{p}$ ) are complex,  $\mathcal{PT}$  operators are defined as

$$\mathcal{P} : \text{Real}\mathbf{x} \rightarrow -\text{Real}\mathbf{x}; \text{Im}\mathbf{x} \rightarrow -\text{Im}\mathbf{x}; \text{Real}\mathbf{p} \rightarrow -\text{Real}\mathbf{p}; \text{Im}\mathbf{p} \rightarrow -\text{Im}\mathbf{p}, \quad (1.38)$$

$$\mathcal{T} : \text{Real}\mathbf{x} \rightarrow \text{Real}\mathbf{x}; \text{Im}\mathbf{x} \rightarrow -\text{Im}\mathbf{x}; \text{Real}\mathbf{p} \rightarrow -\text{Real}\mathbf{p}; \text{Im}\mathbf{p} \rightarrow \text{Im}\mathbf{p}. \quad (1.39)$$

*Real* denotes the real part and *Im* denotes the imaginary part. Under this new class of quantum mechanical Hamiltonians, a real and positive energy spectrum is caused by  $\mathcal{PT}$  invariance [6].

### 1.2.2 $\mathcal{PT}$ -Symmetric Hamiltonian

Recently a class of quantum mechanical Hamiltonians with form

$$\mathcal{H} = p^2 + x^2(ix)^\varepsilon \quad (1.40)$$

is investigated. Here  $\mathcal{H}$  is a function of  $\varepsilon$  and  $\varepsilon$  is real. It is obvious that in this form the Hamiltonian does not satisfy time-reversal or parity-reflection separately but it is invariant under their combined operation. Recall equation (1.17) the eigenvalues of  $\mathcal{H}$  consist the energy spectrum of the system and the eigenvalues are real and positive despite that lacks of conventional Hermiticity. As shown in Figure 1.1 it is obvious that the energy spectrum is discrete and each of the energy level is increasing as  $\varepsilon$  goes up typically for  $\varepsilon \geq 0$ . And it can also be shown that for  $-1 < \varepsilon < 0$  there are finite number of purely real eigenvalues while the rest are their complex conjugate [2].

There are three regions in Figure 1.1. The first one is when  $\varepsilon \geq 0$ , in this region the energy level goes up when  $\varepsilon$  increases and the spectrum is positive and real. The second region is when  $-1 < \varepsilon < 0$ , in this region the real and positive eigenvalues are finite while its complex conjugate is infinite. The number of real eigenvalues decreases as long as  $\varepsilon$  goes from 0 to  $-1$  and the only real eigenvalues is the ground state energy when  $\varepsilon \leq -0.57793$ . The last one is when  $\varepsilon < -1$  where no real eigenvalues exist [2].

Moreover, there are several other complex Hamiltonian that satisfies  $\mathcal{PT}$ -symmetric condition, for example,  $\mathcal{H} = p^2 + x^4(ix)^\varepsilon$  and  $\mathcal{H} = p^2 + x^6(ix)^\varepsilon$ .  $\mathcal{PT}$ -symmetric condition is more general and universal than Hermiticity and it consists the real symmetric Hermitians. For each and every real symmetric Hamiltonian,  $\mathcal{PT}$ -symmetric condition is simultaneous satisfied. Taking  $\mathcal{H} = p^2 + x^2 + 2x$  as an example, in this real



symmetric Hamiltonian time-reversal is preserved. Based on general definition of parity reflection for operator  $\mathcal{P}$ ,  $x \rightarrow -x, p \rightarrow -p$ , the parity reflection is not preserved which indicates this Hamiltonian is not  $\mathcal{PT}$ -symmetric. However the Hamiltonian can be written in form of  $\mathcal{H} = p^2 + (x + 1)^2 - 1$  and in this form the Hamiltonian is  $\mathcal{PT}$ -symmetric as long as the space reflection operate on  $x = -1$  instead of  $x = 0$  [1]. In addition, it can be proved that all Hermitian Hamiltonian have parity. For Hamiltonian with a form of  $\mathcal{H} = p^2 + V(x)$ ,  $V(x)$  is a real function in this form,  $\mathcal{PT}$ -symmetric is generally guaranteed which means that the Hermitian Hamiltonians with this form must be included in  $\mathcal{PT}$ -symmetric Hamiltonians [6]. In other words if a Hamiltonian with this form is Hermitian, it possesses parity reflection and time reversal.

If all the eigenfunctions of Hamiltonian  $\mathcal{H}$  is simultaneously eigenfunctions of  $(\mathcal{PT})^2$ , the  $\mathcal{PT}$  symmetry of  $\mathcal{H}$  is unbroken by definition. In addition, if the  $\mathcal{PT}$  symmetry of Hamiltonian  $\mathcal{H}$  is unbroken then it could be proved that the energy spectrum of  $\mathcal{H}$  is real. Assume  $\mathcal{H}$  possesses  $\mathcal{PT}$  symmetry which means  $\mathcal{H}$  commutes with  $\mathcal{PT}$  operator, assume  $\theta$  is an eigenfunction of Hamiltonian  $\mathcal{H}$  and the eigenvalue of  $\mathcal{H}$  is  $E$ , then  $\theta$  will simultaneously be the eigenstate of  $\mathcal{PT}$  and the eigenvalue is  $\lambda$ .

$$\mathcal{H}\theta = E\theta, \tag{1.41}$$

$$\mathcal{PT}\theta = \lambda\theta. \tag{1.42}$$

It can be proved that the eigenvalue  $\lambda$  in equation (1.42) is a pure phase by multiplying  $\mathcal{PT}$  on left hand side of the equation.  $\mathcal{P}^2 = \mathcal{T}^2 = 1$  since  $\mathcal{P}$  and  $\mathcal{T}$  commute. It is obvious that  $\theta = \lambda^*\lambda\theta$  and thus  $\lambda = e^{i\alpha}$  for some real  $\alpha$ . Next, by replacing the eigenstate  $\theta$  by  $\exp(\frac{-i\alpha}{2\theta})$ , the eigenvalue of  $\mathcal{PT}$  operator will be unitary which means  $\mathcal{PT}\theta = \theta$ . Then multiplying the equation (1.41) by  $\mathcal{PT}$  on the left hand side will obtain  $E\theta = E^*\theta$  since  $[\mathcal{PT}, \mathcal{H}] = 0$ . Thus from this equation we will have  $E = E^*$  which indicates that  $E$  is purely real. There is a paramount assumption

to draw this conclusion which is  $\theta$  is simultaneously an eigenstate of  $\mathcal{PT}$  and  $\mathcal{H}$ . It is true that the eigenstate of an operator  $\hat{A}$  is also an eigenstate of Hamiltonian  $\mathcal{H}$  in quantum mechanics as long as  $\hat{A}$  commutes with  $\mathcal{H}$  and  $\hat{A}$  is a linear operator, however  $\mathcal{PT}$  operator is not a linear operator. Rather,  $\mathcal{PT}$  is antilinear. Therefore some extra assumptions must be made to ensure that  $\mathcal{PT}$  symmetry of  $\mathcal{H}$  is unbroken. This extra assumption is that  $\theta$  is simultaneously eigenstate of  $\mathcal{H}$  and  $\mathcal{PT}$ . However since it is very hard to examine a priori whether  $\mathcal{PT}$  symmetry of a Hamiltonian is broken or not, this assumption might be nontrivial. Recently, Dorey *et al* proved rigorously that the energy spectrum of Hamiltonian  $\mathcal{H}$  in equation (1.40) is real and positive for  $\varepsilon \geq 0$ . Lots of other Hamiltonian  $\mathcal{H}$  with unbroken space-time reflection is investigated and their spectra have been proved to be real and positive [1].

In addition, the converse of this operation has been recently proved that if the energy spectrum of non-Hermitian Hamiltonian is purely real, then it must be  $\mathcal{PT}$ -symmetric with appropriately defined  $\mathcal{P}$  operator  $\mathcal{P}^2 = 1$ . For a  $\mathcal{PT}$ -symmetric system, the  $\mathcal{PT}$ -symmetric phase is defined as the region of parameter space where all the eigenvalues are real and eigenfunctions are of combined PT operator. The  $\mathcal{PT}$ -symmetric breaking is defined as when the system leaves  $\mathcal{PT}$ -symmetric phase. In other words, the eigenvalues of the Hamiltonian are no longer purely real (complex conjugate occurs). Technically, the transition from  $\mathcal{PT}$ -symmetric phase to  $\mathcal{PT}$ -symmetric breaking is defined by a parameter  $\rho_{\mathcal{PT}}$ .

$$\rho_{\mathcal{PT}} = \sum_{\lambda} \int |\Phi_{\lambda}(x) - \Phi_{\lambda}^*(-x)| dx. \quad (1.43)$$

$\mathcal{PT}$ -symmetric phase is maintained only when  $\rho_{\mathcal{PT}}$  equals zero. As long as non-zero  $\rho_{\mathcal{PT}}$  occurs,  $\mathcal{PT}$ -symmetric phase is breaking [19].

### 1.3 Background of $\mathcal{PT}$ -Symmetric Experiment

$\mathcal{PT}$ -symmetric Hamiltonian is not only a mathematical based theory. Recent experiments revealed that many physics models could fit this theory with open non-

equilibrium systems especially for optical system and electrical system [19]. As a physical condition for real energy spectrum of Hamiltonian  $\mathcal{H}$ ,  $\mathcal{PT}$  symmetry is much more concrete than Hermiticity. Since  $\mathcal{PT}$  symmetry condition has not been found out till decades ago, many of the physical observables do not take  $\mathcal{PT}$ -phase transition or  $\mathcal{PT}$ -symmetric condition into consideration before. Therefore, experiments related to  $\mathcal{PT}$  symmetry topic are new and much more work is needed for other research field besides optical and electrical system to reveal the physical basis of  $\mathcal{PT}$ -symmetric system.

### 1.3.1 $\mathcal{PT}$ Symmetry Breaking in Complex Optical Potentials

$\mathcal{PT}$ -symmetry breaking within the context of optics has been observed and this phase transition was found to lead to a loss induced optical transparency specially designed pseudo-Hermitian potentials. Based on Dirac-von Neumann formulation of quantum mechanics, in Hilbert space every observable, including Hamiltonian, must be represented by Hermitian operator because Hermitian operator will ensure the observable a real energy spectrum and the norm of the wave function remains invariant with time. However, since  $\mathcal{PT}$  symmetry condition has been proved to be new condition despite Hermiticity, non-Hermitian Hamiltonian with  $\mathcal{PT}$ -symmetric condition will have a real energy spectrum. In experimental world, one of the interesting effects associated with this kind of Hamiltonian  $\mathcal{H}$  is that the onset of a phase transition corresponding to the breakdown of  $\mathcal{PT}$  symmetry. The energy spectrum will become complex after  $\mathcal{PT}$  symmetry brokedown. Wave propagation in complex potentials has been deeply studied in the past. However the  $\mathcal{PT}$  phase transition was not taken into consideration before. A demonstration of a passive  $\mathcal{PT}$ -symmetry breaking down in optical complex potentials was precisely introduced in 2009. The  $\mathcal{PT}$ -symmetry breaking down will lead to a loss induced optical transparency in specially designed pseudo-Hermitian potentials is cited as a result of the experiment. In addition, this

work paves the way to study of other  $\mathcal{PT}$ -symmetric related observables and open quantum system [12].

### 1.3.2 Stochastic $\mathcal{PT}$ -symmetric Coupler

$\mathcal{PT}$  symmetry can be viewed as a special property of a system in which the loss/-gain is balanced. In optical system,  $\mathcal{PT}$ -symmetric condition is represented by the constraint imposed on refractive index. Even if the system is not exactly symmetric based on the requirement of  $\mathcal{PT}$ -symmetric condition, some unique features related to  $\mathcal{PT}$ -symmetric condition can still be observed as long as the system is linear and this is called passive  $\mathcal{PT}$ -system. In any experimental settings, the  $\mathcal{PT}$ -symmetric condition could be viewed as an averaged effect since perturbation and fluctuation thermal effect is somewhat inevitable. Even if the experimental condition is highly precise the random effect will ruin the delicate balanced gain and loss. Therefore to discuss the persistence of the properties for a deterministic  $\mathcal{PT}$ -symmetric system of which the parameters are subject to a small random variation become meaningful. V. V. Konotop and D. A. Zezyulin set up an experiment to address the behavior of  $\mathcal{PT}$ -symmetric coupler in 2014 to illustrate the random variation effect on  $\mathcal{PT}$ -symmetric system [14]. In their experiment broken and unbroken  $\mathcal{PT}$ -symmetry have been observed from a stochastic  $\mathcal{PT}$ -symmetric coupler operated by a dual-core waveguide. By inputting fluctuating parameters the gain and losses are balanced in average. Independently on whether the  $\mathcal{PT}$  symmetry of the underlying deterministic system is broken or not and independently on the type of fluctuations the statistically averaged intensity of the field grows. This growth is always observed in the waveguide with gain and depending on the system parameters may be observed or not in the absorbing waveguide. The evolution of the mean field preserves the properties of the  $\mathcal{PT}$ -symmetric dynamics where fluctuations of the gain/loss and of the coupling act respectively as the effect gain and dissipation. Their work also paves the way to study the effect of fluctuations of propagation constant or effective Kerr coefficient [14].

### 1.3.3 $\mathcal{PT}$ -Symmetries in Active LRC Circuits

Recently, it is found out that for a system that does not obey parity reflection ( $\mathcal{P}$ ) and time reversal ( $\mathcal{T}$ ) separately but do obey a combined  $\mathcal{PT}$ -symmetric condition. In addition, there was no experiment that investigates the  $\mathcal{PT}$ -system in spatiotemporal domain. In 2011,  $\mathcal{PT}$ -symmetry breaking has been observed in coupled electrical circuits [15]. Mutually coupled modes of a pair of LRC circuits, one with amplification and another with an equivalent amount of attenuation, realized an experiment of a wide class of systems where gain/loss mechanisms break the Hermiticity while preserving  $\mathcal{PT}$  symmetry. The experiment is simple and straightforward. It displays the entire universal phenomenon with generalized  $\mathcal{PT}$ -symmetric condition. Meanwhile the experimental results allow us to deeply investigate the  $\mathcal{PT}$ -symmetric system as well as make comparison with the theoretical result. The experimental results for active LRC circuits pave the way to the experimental analysis for a more complicated  $\mathcal{PT}$ -symmetric system in spatiotemporal domain and it will intrigue the studies for  $\mathcal{PT}$ -symmetric study in other fields instead of electric realm [15].

### 1.3.4 $\mathcal{PT}$ Phase Transition in Mechanical System

Generally speaking, Hamiltonian  $\mathcal{H}$  with  $\mathcal{PT}$ -symmetric condition usually exhibits two parametric regions. In one region the eigenvalues of  $\mathcal{H}$  are all real and this region is called unbroken  $\mathcal{PT}$  symmetry region while in the other the complex eigenvalues of  $\mathcal{H}$  emergence and it is called broken  $\mathcal{PT}$  symmetry region. Obviously there is a  $\mathcal{PT}$  phase transition between these two regions. Motivated by the experiment mentioned in 1.3.3, an analog mechanical experiment was constructed using a pair of a coupled driven pendula in 2012 [20]. Similar with the coupled electrical circuits (coupled modes of a pair of LRC circuits), coupled pendula could be viewed as mechanical oscillator and it has been used in lots of other experiment to demonstrate the complex physical phenomena. In this experiment, two coupled pendula are used, one with energy gain (driven) while the other one with energy loss (damped). To

simulate the energy-conserving mathematical oscillator model, two identical pendula are suspended to from a horizontal rope of total length 94cm. The coupling of the two pendula could be varied by adjusting the tension of the horizontal rope. The separation of two pendula is 34 cm and each of them consists a 50-gram cylindrical mass hanging from the string of 39cm in length. An electromagnet is set up to add and absorb energy from the pendulum. When the electromagnet is turned on, a small impulse is generated to the string which applied to the right pendulum moving towards the electromagnet by adding a small amount of kinetic energy on it while applied to the left pendulum moving away from the electromagnet by absorbing a small amount of kinetic energy on it. The electromagnet is triggered using an optical sensor which is precisely controlled to operate in a certain order. A video camera is used to document the movement of the coupled pendula. The tension of the string as well as the energy input/output is changed during the experiment to find the position where  $\mathcal{PT}$  symmetry breaks down and compare the data with theoretical result. To sum up, the  $\mathcal{PT}$  phase transition is easy to explain in an intuitive level in this experiment. The  $\mathcal{PT}$  phase change takes place at a critical point of coupling is observed [20].

### 1.3.5 $\mathcal{PT}$ Asymmetry in Viscous Fluid with Balanced Inlet/Outlet Flow

All the studies mentioned above revealed that open system with balanced sink and source transfer from  $\mathcal{PT}$ -symmetric state to asymmetric state while  $\rho_{\mathcal{PT}}$  goes from zero to non-zero. Generally speaking, the terminology source-sink and gain-loss are widely seen in many research field including optics, electrics and fluid dynamics etc. Typically for fluid dynamics the notion inflow-outflow is used to describe an open, non-equilibrium system. However, since most of the viscous fluid has the non-linear nature which is described by the Navier- Stokes equations, it is not straightforward to derive its symmetry properties. Superposition properties cannot be applied to specific symmetric system to construct solutions. Generally speaking, the symmetry

properties of flow fields with identical inlet and outlet velocity profile remain unexplored. In 2013, Dr. Yu and her students from Indiana University-Purdue University Indianapolis (IUPUI) did some preliminary computational investigation of a flow field with balanced inlet/outlet flow. Most of their work was done to analyze the asymmetries relationship between of velocity, kinetic energy density, and vorticity fields with low Reynolds number. The Reynolds number  $Re$  is defined as

$$Re = \frac{\rho UL}{\mu} \quad (1.44)$$

where  $\rho$  is the fluid density,  $U$  is the velocity,  $L$  is the characteristic length and  $\mu$  is the fluid dynamic viscosity. Their computational results showed  $\mathcal{PT}$ -symmetric flow field configurations offer a hitherto unexplored avenue to tune fluid flow properties [19]. Their preliminary computational results are shown in Figure 1.3.

#### 1.4 Motivation

As mentioned above, current experiments exploring  $\mathcal{PT}$ -symmetric system concern mostly about energy or electromagnetic. There were no experimental efforts on examining viscous fluid  $\mathcal{PT}$ -symmetric system. There are certain computational results but they are inadequate. Experiment is needed to improve the understanding of viscous  $\mathcal{PT}$ -symmetric system. Typically, for a viscous fluid system one must distinguish the mass flow, defined by  $\mathcal{PT}$ -symmetric boundary condition and energy flow properties, characterized by the fluid viscosity.

Earlier computational attempts were done to explore the relationship between kinetic energy density of the  $\mathcal{PT}$ -symmetric flow field and Reynolds number as well as vorticity and Reynolds number. Lattice Boltzmann method was used but it is inadequate to clarify the truth of the  $\mathcal{PT}$ -symmetric fluid problem by computational results only. Experiment concerning this problem is also needed to make the analysis comprehensive. Therefore, exploring the  $\mathcal{PT}$ -symmetric flow field experimentally will

be an interesting topic and it will be helpful on building up the fundamental concepts for understanding and application of  $\mathcal{PT}$ -symmetric theory in fluid dynamics.

### 1.5 $\mathcal{PT}$ -symmetric Fluid System

System that continuously exchange mass, energy or information with environment are open system and they have been well studied in the past because they intrigue a lot of interesting questions in both theoretical and practical world. Generally speaking, the exchange between open system and environment is a one-way transfer. Friction, viscous drag, and even Joule heating are transferred from the open system to the environment and they could be viewed as the energy loss (sink) of the system. However, seldom open systems exist with energy gain (source) except some optical system as mentioned in previous section. Open system with balanced gain and loss is predicted to exhibit several unique properties in the past few decades and such system is described as  $\mathcal{PT}$ -symmetric system. As mentioned in 1.3, most of the experiments to explore  $\mathcal{PT}$ -symmetry of a special designed system have dissipation and amplification of the energy. Since the systems are designed with balanced boundary condition, they showed a positive threshold for the loss/gain strength above which the solutions of equation of motion develop asymmetry. Technically a fluid system with small gain and loss is globally same as a closed system, the reflection-symmetry is preserved in. In contrast for a fluid system with large gain and loss is globally different from a closed system and the reflection-symmetry is not preserved. Thus it is not straightforward to design a flow field with  $\mathcal{PT}$ -symmetric boundary conditions. Traditionally, viscous flows are driven by upwind flow, pressure difference, or boundary movement and therefore the (steady-state) velocity profiles at the inlet and outlet are, in general, not related. Flow system with balanced inflow and outflow with identical velocity profile remains unexplored for a long time. It is true that flow field with porous wall which acts as inlet and outlet flow has been widely studied but the velocity profile is still not identical that  $\mathcal{PT}$ -symmetry is not preserved in those system.



As mentioned before,  $\mathcal{PT}$ -symmetric fluid system must be strictly balanced (inflow/outflow). This is not only for the geometric configuration but also for the boundary condition. For example there is a set of fluid system with certain geometric configuration and boundary condition shown in Figure 1.2, the blue circle represents the outflow (sink) while the red one represents the inflow (source). The only two balanced ( $\mathcal{PT}$ -symmetric) systems are the ones in (a) and (b) since they have a symmetric geometric configuration and boundary conditions are symmetric to x-axis or y-axis. The boundary conditions are not symmetric for the one in (c) while the geometry is not symmetric for the one in (d).

Moreover, the velocity profile must be ensured to be identical. Generally speaking, fully developed laminar flow is easy to control and generated. The velocity profile for a fully developed laminar flow within a pipe is fixed and it is the well-known Poiseuille flow. Poiseuille flow is one of the exact solution to Navier-Stokes equation. Several assumptions are made for Poiseuille flow including the flow is steady ( $\frac{d}{dt} = 0$ ); the radial and swirl components of the fluid velocity are zero ( $u_r = u_z = 0$ ) and fully developed ( $\frac{d}{dx} = 0$ ). In order to make the inlet/outlet velocity profile identical, the inlet/outlet flow rate must be fixed exactly same and both of them should be fully developed. Therefore the paths to both inlet and outlet must be long enough to ensure this critical condition. A cuboid test section is easier to fabricate than a cylindrical one. The computational work can be done on a same cuboid domain easily. The inlet/outlet tubing is chosen of a square cross section that best fit the test section. For Poiseuille flow in cylindrical tubing the velocity profile is parabolic curve and Poiseuille flow between parallel planes is also parabolic. It is true that the velocity profile of Poiseuille flow in square tubing is not parabolic. The mathematical expression for that velocity profile is quite complex, however, as long as the flow is fully developed with the same flow rate in same pipe, the velocity profiles are identical. This is why Poiseuille flow is chosen to set up the boundary conditions for  $\mathcal{PT}$ -symmetric flow field in the present study.

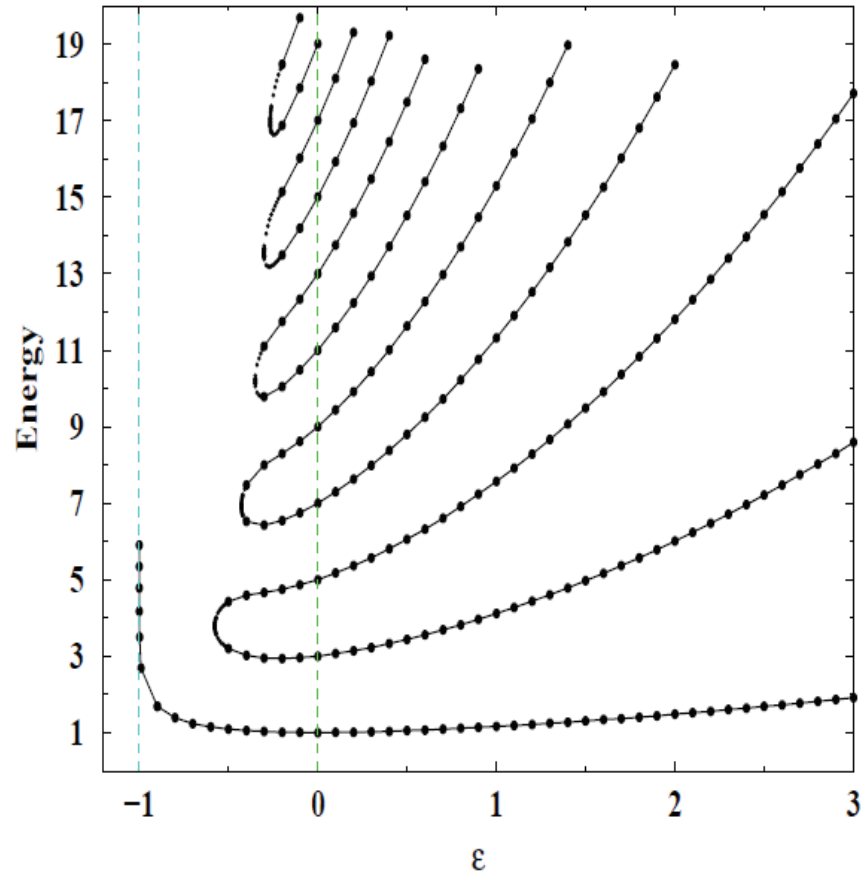


Figure 1.1. Energy levels of the Hamiltonian  $\mathcal{H} = p^2 + x^2(ix)^\varepsilon$  as a function of parameter  $\varepsilon$  [2].

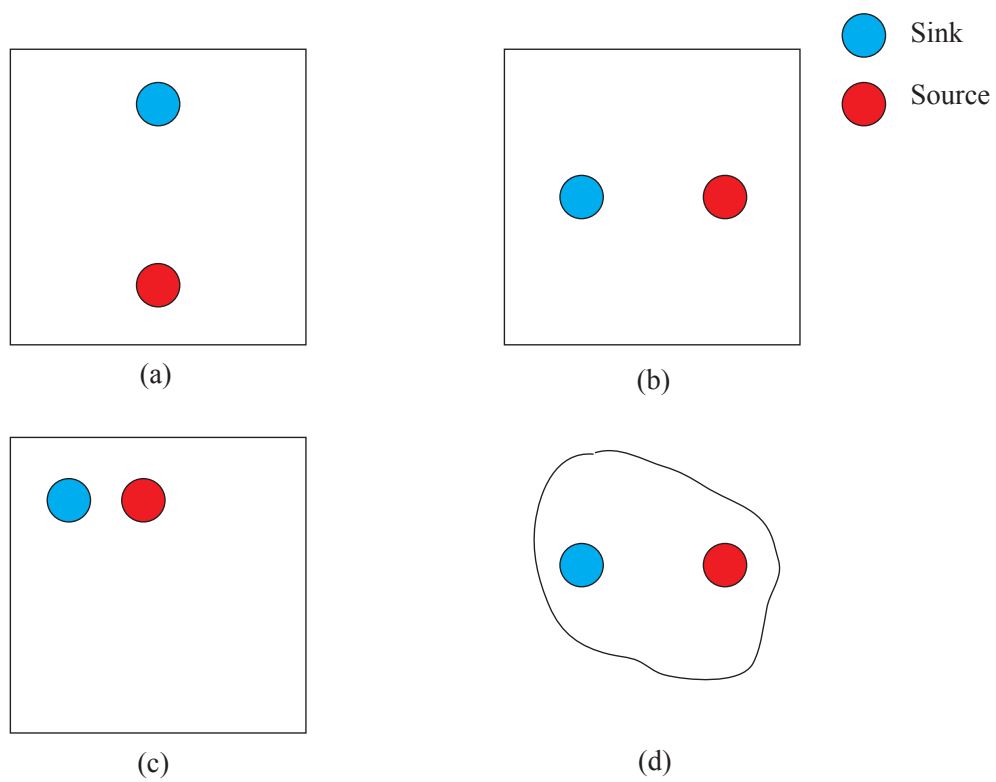


Figure 1.2. Demonstration of  $\mathcal{PT}$ -symmetric flow field.

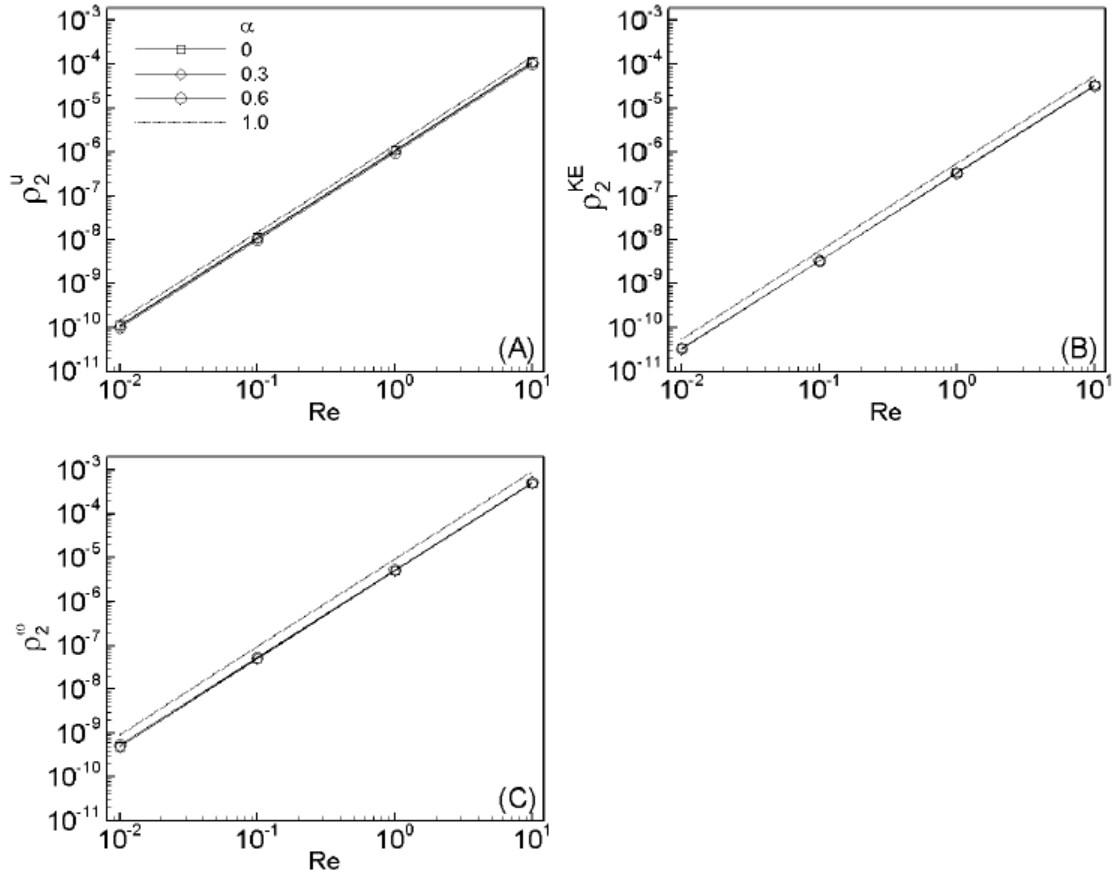


Figure 1.3. The power law scaling between asymmetries and Reynolds number from preliminary computational results [19].

## 2. EXPERIMENTAL FACILITY

As mentioned in the previous chapter, in order to create a symmetric flow field, symmetric geometric configuration and boundary condition are needed to be guaranteed at the same time. In the present study a cuboid test section with long inlet and outlet tubes is fabricated for the experiment. The long inlet and outlet create fully developed inflow and outflow so their velocity profiles are the same exactly. In this experiment, particle image velocimetry (PIV) is used to measure the detailed flow field. The sketches and photos for the experimental facility are shown in Figure 2.1.

### 2.1 Test Section

In this experiment, two test sections are designed to explore the unique features of  $\mathcal{PT}$ -symmetric flow field, one with a symmetric inlet/outlet flow while the other one adds a symmetric perturbation (main flow) based on the first one. The sketch for the test sections are shown in Figure 2.2. Water is used as fluid in the experiment.

The geometric configuration of the test section must be exactly symmetric. Since there are already some preliminary computational results the test section is designed based on that. The dimensions of the test section are listed in Table 2.1.

Since PIV method is applied in this experiment the test section must be optical clear which means its material should be able to let the laser pass through with little absorption and it cannot affect the CCD camera for image acquisition. Acrylic is chosen to manufacture the test section.

During image acquisition process the flow is illuminated by the laser sheet which is coming from the top of the test section and the camera will grab the images from the front direction which is perpendicular to the laser sheet.

### 2.1.1 Inlet/Outlet Tubing Design

For a  $\mathcal{PT}$ -symmetric system, the boundary condition should also be symmetric besides the geometric configuration, in other words, the velocity profile at the inlet and outlet should be exactly the same. However it is impossible to control the velocity profile at the inlet and outlet to make them identical if they are not fully developed. Therefore, an enough long inlet and outlet tubes are needed to produce an identical velocity profile.

Entrance length is that what the fluid need to be fully developed in a pipe flow. Consider a flow entering a pipe and assume the velocity profile is uniform at the beginning. As soon as the flow enters the pipe the velocity profile changes, due to viscous effect from pipe surface the flow adjacent to the wall will decelerate and the boundary layer will develop as a result. The boundary layer thickness will grow as moving to downstream. Finally the boundary layer will merge to the centerline so the velocity profile becomes parabolic, and the flow is fully developed. The length of tube that between the entrance and flow where fully developed occurs is defined as entrance length. For laminar flow, which is what the experiment focused on, the entrance length  $Le$  can be estimated by [49]

$$\frac{Le}{d} = 0.06Re \quad (2.1)$$

where  $d$  is diameter or height of the cross section.

The test section of the experiment is cuboid and the cross sections of the test sections where inlet and outlet locate are square. To make the system be symmetric, the cross sections of the inlet and outlet are also square. Thus aluminum tubings are used and their dimensions are listed in Table 2.2.

The Reynolds number of this experiment varies from 60 to 700 which is determined on the preliminary computational result and feasibility of the experiments. The entrance length for different Reynolds number is computed and shown in Table 2.3.

## 2.2 Syringe Pump

A pump is used in the experiment to drive the flow in the test section. Pumps can be classified into three main groups based on the mechanism they used to drive the fluid: direct lift, gravity and displacement pumps. In our application the scale is relatively small and the flow velocity is in a low range. Therefore a syringe pump is chose to drive the fluid for the experiment.

In addition, since the PT symmetric requires the boundary condition to be exactly symmetric. The best way to ensure this condition is to pump water at the inlet of the test section while withdraw water at the outlet of the test section with the same speed. Water can be assumed as incompressible fluid so as long the inlet velocity is fixed the outlet velocity should be the same as the inlet. Two syringe pumps will precisely ensure this requirement: one for injection and the other for withdraw. The two pumps are synchronized so that a symmetric fluid field could be generated.

From the aforementioned analysis, a Dual NE-1000 syringe pump system from NewEra Syringe Pump Company is chosen. The syringe pumps under NE-1000 Family are designed with different modes including operating stand alone or being controlled from a computer. They are able to perform infuses and withdraws, and detect motor stall, with a dispensing accuracy of  $+/- 1\%$ .

### 2.2.1 Pumping Flow Rate Calculation

The pumping flow rate is calculated for different Reynolds number. The velocity is calculated using different Reynolds number and with these velocities the flow rate, which is used to set syringe pump, can be computed

$$Q = U_p \times A \tag{2.2}$$

where  $Q$  stands for the volumetric flow rate,  $U_p$  the averaged velocity and  $A$  the area of the cross-section,

$$A = W^2. \quad (2.3)$$

The cross section of the inlet and outlet are square with a width of  $W = 2.54mm$ . Therefore the calculated pumping flow rates and averaged velocities at different Reynolds number is used to the input parameter of the syringe pumps. The result is shown in Table 2.4.



Table 2.1. Geometry of the test section.

<b>Length</b>	<b>Width</b>	<b>Height</b>
76.2mm	38.1mm	38.1mm

Table 2.2. Geometry of the inlet/outlet tubing.

<b>Length</b>	<b>Width (inner)</b>	<b>Height (inner)</b>
292.1mm	2.54mm	2.54mm

Table 2.3. Entrance lengths at different Reynolds numbers.

<b>Reynolds number</b>	<b>Le</b>
60	9.144mm
80	12.192mm
100	15.240mm
200	30.480mm
500	76.200mm
700	106.680mm

Table 2.4. Volumetric flow rates and averaged velocities at different Reynolds numbers.

<b>Re</b>	<b>Q (ml/min)</b>	<b><math>U_p</math> (mm/s)</b>
60	4.581	11.83
80	5.344	15.78
100	7.635	19.72
200	15.270	39.45
300	22.905	59.17
400	30.540	78.90
500	38.175	98.62
600	45.810	118.34
700	53.445	138.07

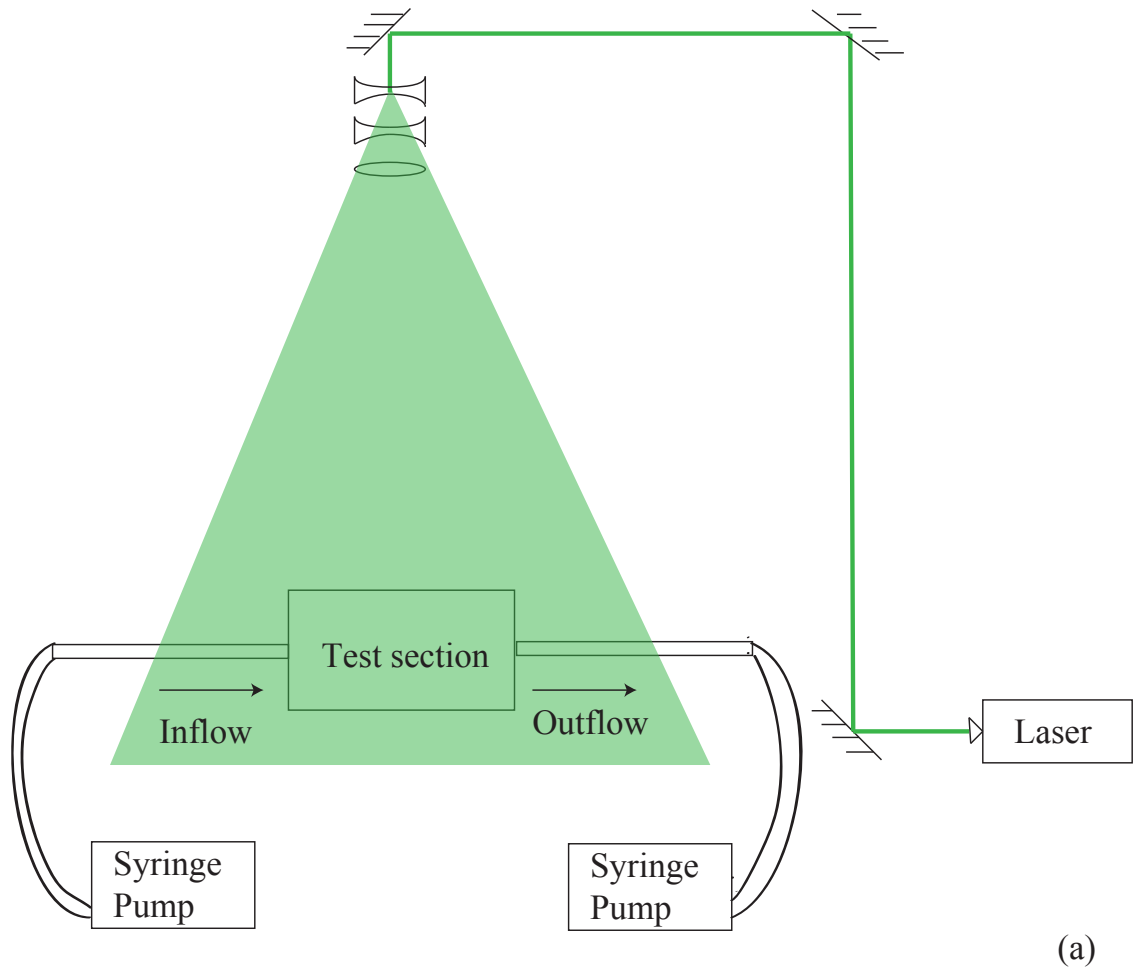
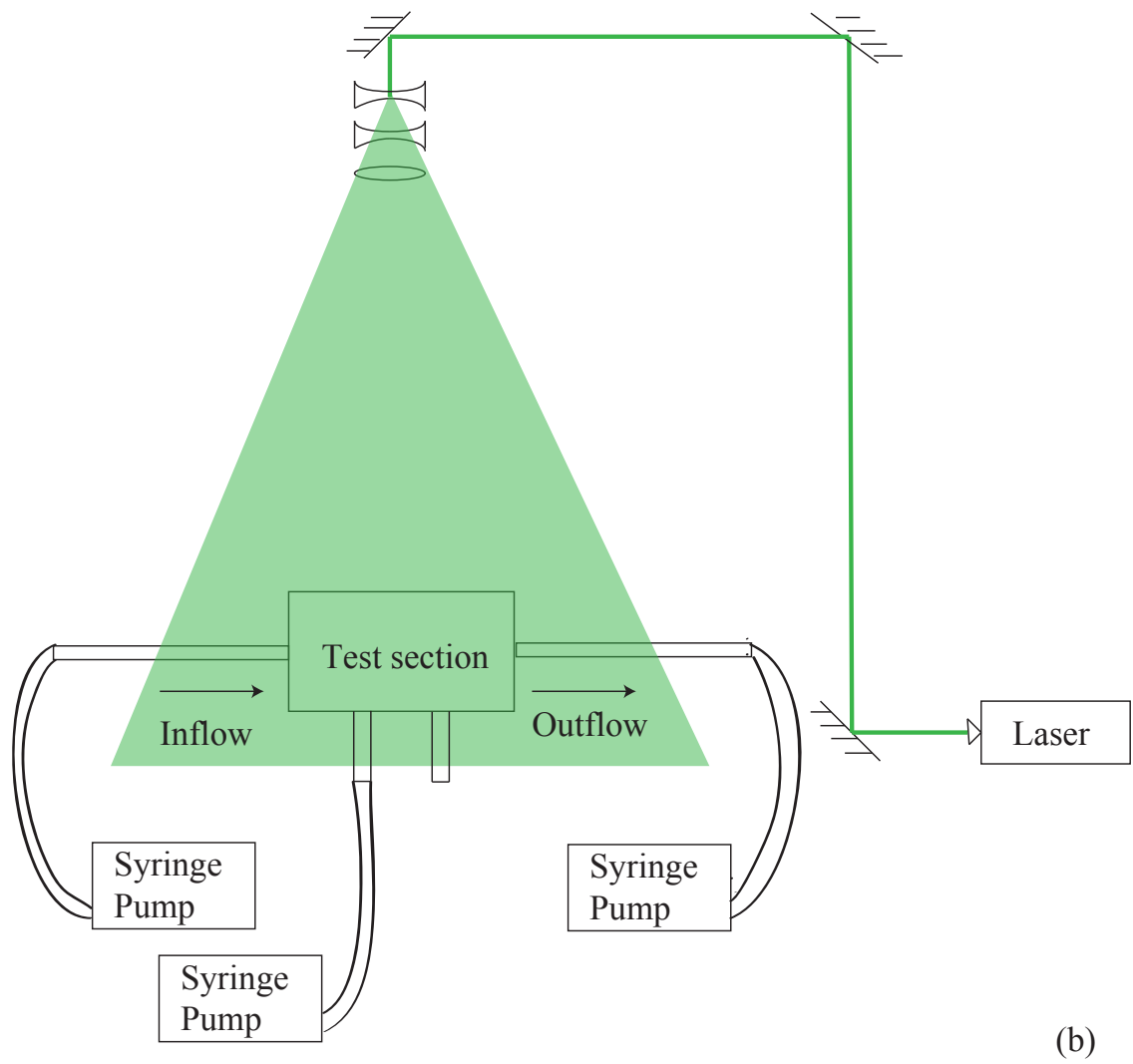


Figure 2.1. Schematics of the system, (a) Without main flow, (b) With main flow.



(b)

Figure 2.1.Continued.

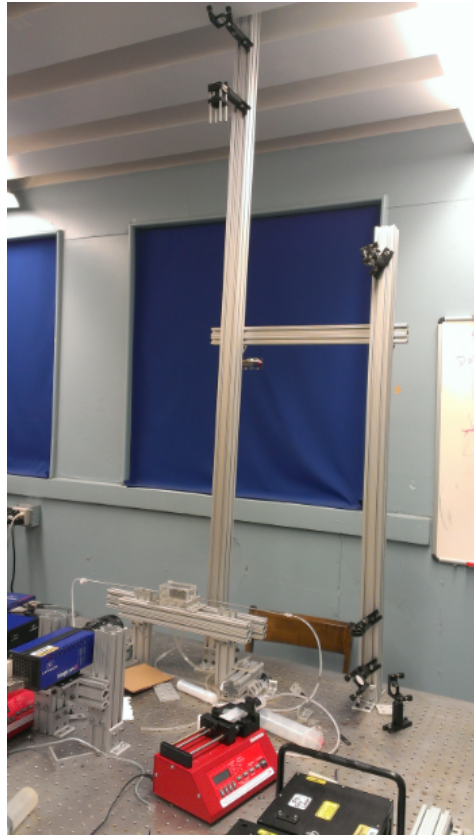


Figure 2.1.Continued.

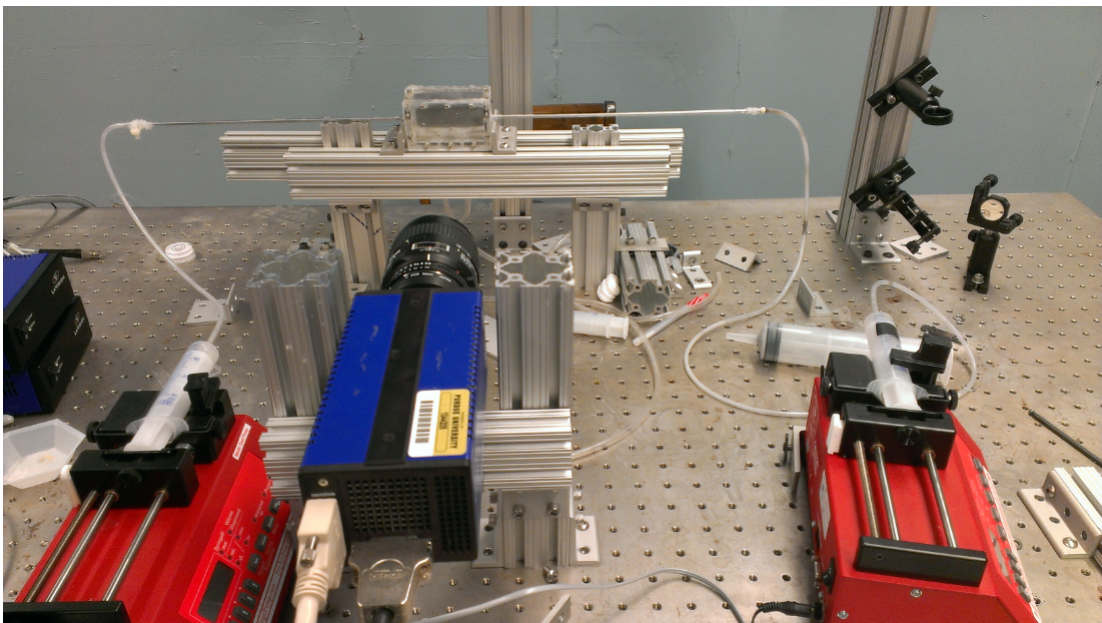
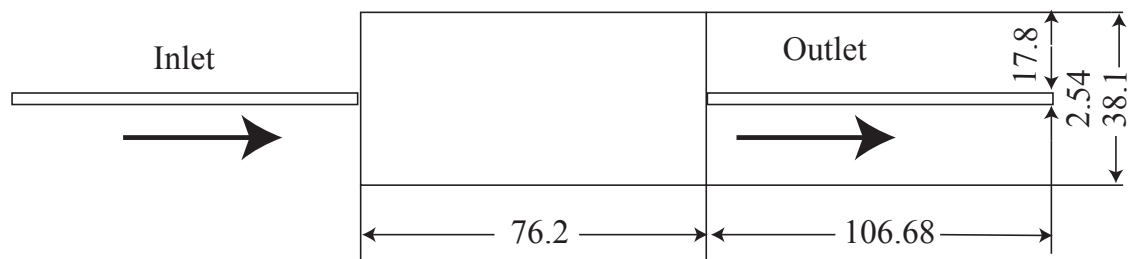
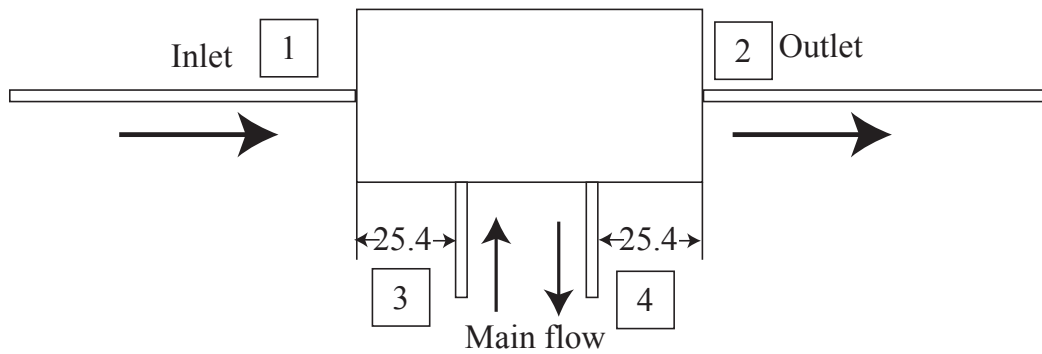


Figure 2.1.Continued.

Unit:mm



(a) Test section with symmetric inlet/outlet flow



(b) Test section with symmetric inflow/outflow under main flow

Figure 2.2. Schematics of test section.

### 3. INSTRUMENTATION

#### 3.1 Fundamentals of Particle Image Velocimetry

Particle image velocimetry method is laser-based optical method of flow diagnostics and it is used to measure the flow field in this experiment. An instantaneous two-dimensional velocity field can be measured by PIV. The fluid is usually seeded with tracer particles. They are sufficiently small so can follow the flow. The particles are illuminated by a laser sheet and their motions will be recorded by digital cameras. Velocity vectors are then analyzed by processing the particle images. Unlike the traditional probe-type method, PIV represents a non-invasive measurement technique, thus it creates no-interference to influence on the flow field. In addition it will be more applicable to small test section as well as the ones with complex geometric configuration.

Typical PIV system consists of a laser with optical system to generate the illuminating laser sheet. The optical system includes at least a cylindrical lens to diverge the circular laser beam into a sheet. In addition it may also include at least one lens to focus the laser beam along the direction that is perpendicular to the divergence direction. In this way the laser sheet could be thin enough to illuminate the flow field in test section. PIV system also has one or more digital cameras with CCD or CMOS chip. The cameras are used to record the images of seeding particles while the flow field is illuminated. An image acquisition system is to acquire and transfer the images from cameras to computer random-access memory (RAM), and save the images on hard drives for post-processing. A synchronizer is also needed to synchronize the timing events of cameras and laser. PIV software is used to post-process the particle images to obtain velocity field. A typical PIV system arrangement is shown in Figure 3.1.



### 3.1.1 Image Acquisition

In a typical PIV experiment, two digital images,  $G_1$  and  $G_2$  are recorded with a time delay  $\Delta t$  between them, as shown in Figure 3.2 [51]. The PIV recording modes can be classified into two main categories: (1) methods which capture the illuminated flow on to a single frame and (2) methods which provide a single illuminated image for each illumination pulse. These branches are referred to as single frame/multi-exposure PIV (Figure 3.3) and multi-frame/single exposure PIV (Figure 3.4), respectively. The principal distinction between the two categories is that the former method, without additional effort, does not retain information on their temporal order of the illumination pulse giving rise to a directional ambiguity in the recovered displacement vector. This method introduces a wide variety of schemes to account for the directional ambiguity. In contrast, multi-frame/single exposure PIV recording inherently preserves the temporal order of the particle images and hence is the method of choice if the technological requirements can be met. Also in terms of evaluation this approach is much easier to handle. In the present study, double-frame/single exposure PIV recording is used.

### 3.1.2 Image Processing

Typically, PIV recordings are subdivided into interrogation areas during evaluation. These areas are called interrogation spots in the case of optical interrogation or interrogation windows when digital recordings are considered. The main objective of the statistical evaluation of PIV recordings at medium image density is to determine the displacement between two patterns of particle images, which are stored as a two dimensional distribution of gray levels. To determine the displacement in a certain

interrogation windows  $g_1$  and  $g_2$ , the cross-correlation value  $\phi(m, n)$  between them is calculated,  $\phi(m, n)$  is defined as [51]:

$$\phi(m, n) = \sum_{i=1}^M \sum_{j=1}^N g_1(i, j)g_2(i + m, j + n). \quad (3.1)$$

Here M and N are the sizes of the interrogation window in pixels.

The distribution of correlation values, i.e. the correlation map, is obtained by varying values of m and n (or window shifting, as shown in Figure 3.5). The location of the peak in  $\phi(m, n)$  gives the mean particle displacement within  $g_1$ , the same procedure can be done on  $g_2$ . By subtracting the displacement of  $g_1$  from  $g_2$  and divided by  $\Delta t$ , the velocity field is obtained [51].

### 3.1.3 Post-Processing

Generally speaking, there are a great number of images which must be further processed using PIV technique. The recorded data can easily amount to some gigabytes, thus it is quite obvious that a fast, reliable and fully automatic post-processing of the PIV data is essential [23]. Post-processing of PIV data is characterized by the following steps:

**Validation of the raw data.** After automatic evaluation of the PIV recordings, a certain number of obviously incorrectly determined velocity vectors (outliers) can usually be found by visual inspection of the raw data. In order to detect these incorrect data, the raw flow field data have to be validated. For this purpose, special algorithms have to be developed, which works automatically [23].

**Replacement of incorrect data.** For most post-processing algorithms it is required to have complete data fields as is quite naturally the case for numerically obtained data. Such algorithms will not work if gaps (data drop-outs) are present in the experimental data. Thus, means to fill the gaps in the experimental data must be developed [23].

**Data reduction.** It is quite difficult to inspect several hundred velocity vector maps and to describe their fluid mechanical features. Usually techniques like averaging (in order to extract the information about the mean flow and its fluctuations), conditional sampling (in order to distinguish between periodic and non-periodic parts of the flow) and vector field operators (e.g. vorticity, divergence in order to detect structures in the flow) are applied [23].

**Analysis of the information.** At present this is the most challenging task for the user of the PIV, technique. PIV being the first technique to offer information about complete instantaneous velocity vector fields, allows new insights in old and new problems of fluid mechanics. Tools for analysis such as proper orthogonal decomposition (POD) or neural networks are applied to PIV data.

**Presentation and animation of the information.** A number of software packages commercial as well as in-house developed ones are available for the graphical presentation of the PIV field data. It is also very important to support the easier understanding of a human observer of the main features of the flow field. This can be done by contour plotting, color coding, etc. Animation of the PIV data is very useful for better understanding in the case of time series of PIV recordings or 3D data.

### 3.2 Continuous PIV System

In the present study, two separate PIV systems are developed for measuring flow fields at different Reynolds number. For low Reynolds number case ( $Re < 300$ ), a continuous PIV system is used. For high Reynolds number case ( $300 < Re < 700$ ), a pulsatile PIV system is used.

The continuous PIV system used in this experiment includes a continuous-wave laser (peakpower<500mW, wavelength 500-600nm), a high-speed CMOS camera (Flare 2M360-CL) and optical system. The laser continuously illuminate the test section while the CMOS camera grabs the images at a specific frame rate. The time interval between consecutive images is determined by the frame rate. Thus it is easier to op-

erate than pulsed system and it is enough for a low Reynolds number case where the flow is slow. However, as the Reynolds number and the velocity increases, continuous PIV system will meet some limitations. The higher the speed of the velocity field, the shorter time interval of the particles images is required and the frame rate of Flare 2M360-CL is at most 300 which is not enough as Reynolds number goes beyond 300 and it is not capable for collecting data.

Technically two images with a certain time difference are used for PIV software to do post-processing, i.e. to compute the velocity field. The  $\Delta t$  should be determined before the data is collected. If it is too short it is difficult to distinguish the motions of particles accurately. If it is too long it may not find enough particle pairs due to out-of-plane motion. Thus the time interval is very important for PIV post-processing. For example, in order to have a time interval during which takes the particles move 10 pixels on the recorded images if the estimated velocity is  $1mm/s$  and the test section is  $1024mm \times 1024mm$ , the resolution of the camera is  $1024 \times 1024$  pixels, the physical scale of each pixel is then  $1 mm$ , the estimated time interval is  $10s$ . Based on the estimation one set  $\Delta t$  for a pulsed PIV system or the frames per second (fps) for a continuous system where  $\Delta t = \frac{1}{fps}s$ .

### 3.2.1 High-Speed CMOS Camera

In the continuous PIV system a high speed CMOS camera (Flare 2M360-CL) is used for image acquisition. The resolution of this CMOS camera is  $2048(horizontal) \times 1088(vertical)$  pixels. It can run up to 300 fps under 8-bit mode. Unlike pulsed PIV system, continuous PIV system generates a PIV time-series sequence. Since the images are collected continuously, every image could be compared with its consecutive one. In other words, if images in a time series are named *Image1*, *Image2*, *Image3* etc. *Image1* and *Image2* could be used for calculation while *Image2* and *Image3* could also be used for calculation.

The only parameter that is needed to set in this experiment is the fps of the camera. The fps is  $\frac{1}{\Delta t}$ . For different Reynolds number and for a certain fluid, water in this experiment for example, the density and viscosity are assumed as constants. The mean velocity and maximum velocity can be calculated and the fps can be easily estimated. Since the resolution of the camera is  $2048 \times 1088$  pixels which is similar to the scale ratio of the length and height of the test section, the camera is set up to grab the images in the direction which is towards the rectangular face. In the PIV processing session, a user defined mask is added to avoid the pixels outside the area-of-interest.

Theoretically the fps for Flare 2M360-CL can be set up to 300 in full mode. However it is only for the speed of grabbing images into camera, not the speed of transferring images to computers. Thus image acquisition hardware and software are needed to save the images to hard disk. Flare 2M360-CL relies on a Matrox Solios eV-CLF image board to interact with computer to save the acquired images to hard drive. Matrox Solios eV-CLF is a value-packed PCIe $\times$ 4 frame grabber that supports the full-range of Camera Link interfaces (dual-Base, single/Medium/Full mode, 10-tap and PoCL) and offloads typical pixel pre-processing tasks [44].

A PCIe $\times$ 4 host interface provides the throughput necessary to ensure the continuous flow of pixels from the frame grabber to RAM. The peak bandwidth can be up to 1GB/s. The highest fps for Flare 2M360-CL is 300 and every acquired image is of 2.5MB of memory therefore the bandwidth should be at least 750MB/s for the camera to operate under full mode and highest speed [44]. Matrox Solios eV-CLF is qualified for this requirement.

Matrox Imaging Company provides examples in their software development tools and there is one for a real-time image acquisition. However this program and this operation only allows to grab the images from camera and save them on hard drive directly, but it requires the processing speed of CPU be fast enough. In addition since an image is saved on hard drive directly after it is grabbed, the write in speed of hard disk must be fast enough too so the computer is able to manage the next

image acquisition request. As mentioned above, the needed data transfer rate is up to 750MB/s. The computer used in this experiment is a DELL OPTIPLEX 760 that uses SATA II cable hard drive and the maximum write in speed for this kind of hard drive is 300MB/s which is much lower than the need of the present continuous PIV system.

Technically there are two solutions to overcome this limitation, one in hardware and the other in software. For the hardware solution, a hard drive can be changed to a faster one, SATA III or solid-state drive for example. Once the computer has a fast enough hard drive the image acquisition software will be able to manage the high speed image acquisition. The software solution requires customization of the program provide by Matrox Imaging Company. The fundamental idea concept is to save the acquired images to the RAM in the first place. After the entire image grabbing process is finished, the images will be transferred from RAM to hard drive in batch. This method is feasible because the speed of writing images in RAM is much faster than the speed of writing in hard drive. It takes longer for finishing the entire image acquisition process than the aforementioned hardware solution but it does not require a high-performance in hardware, which saves cost significantly.

To overcome the limitation of hardware, a new image acquisition software is developed in the present study.

### **3.2.1.1 Software Development**

From Matrox Imaging Company software development kits, several examples are available in building up software that could achieve the functions mentioned in the previous section. In addition most of the functions appeared in the examples are available by referring in the Matrox Imaging Library (MIL) Version9.0 with Processing Pack 1 User Guide [39].

All functions in MIL are grouped into modules. Each function is named by their functionality and module. Their name is prefixed with M, which stands for Matrox,

then followed by several letters representing its module name and ended with a word that describes its functionality. Taking **MbufSave()**, as an example, it saves a data buffer in a file.

Matrox Imaging Library consists a large number of functions including image grabbing, image saving, image analyzing and image processing. The software developed for this study utilizes important functions (sorted in category) like:

**M...Free()** these functions free an allocated MIL object and its requested resources.

**M...Alloc()** these function allocates the specified MIL object (for example, buffer, display, or context) and its required resources. The user must request these resources before using them. After finishing using them, they will be released using **M...Free()**.

**M...GetHookInfo()** these functions retrieve information about the event that causes the hook-handler function to be called. These functions should only be called within the scope of a hook-handler function call.

**M...Save** these functions save the specified MIL object (for example, the specified context or buffer) to a specified file.

**M...HookFunction** these functions allow the user to attach or detach a user-defined function to a specified event. Once an event-handler function is defined and hooked to an event, it is automatically called when the event occurs. The event-handler function is also referred to as a hook-handler function.

**MdigGrabContinuous()** this function allows the user to grab images continuously from the same buffer which is allocated the digital configuration file(DCF) until the user issued **MdigHalt()**. Since this function allows the grab continuously from the same buffer it is only useful when the buffer selected to display.

**MdigProcess()** this function allows the user to grab the images sequentially, store them into a list of image buffers, and process them as they are being grabbed. This function has the same requirements as **MdigGrabContinuous()** except it ac-

cepts an array of grab image buffers and can cause a user-defined function to be called after an image has been grabbed into any of the image buffers.

The software can be developed using Visual Basic,  $C\#$  or  $C++$ . The coding is done using  $C++$  in the present study. To fulfill the high speed image acquisition requirement. The code is attached in Appendix. In the code a few parameters can be changed including  $\#$  define BUFFERING SIZE MAX. The users could change the number of images they want to grab, and the maximum number of images depends on the available RAM. If the RAM on the computer is not enough to store all the images, some of them will be missing. Therefore a suitable number is important for the application. Another parameter is located at the end of the code MosPrintf (Text, STRING LENGTH MAX, MIL TEXT (*Image%ld.tif*)). In this line the users can define the name for the images as well as format. In this experiment the images is names as *Image1*, *Image2*, *Image3* etc. and the *tiff* format is used.

### 3.2.2 Frame Rate Estimation

The frame rate of the camera can be estimated from the velocity of flow field. In order to estimate the frame rate of the high speed camera, the pixels of the camera and scale of the test section is needed. It will be easier for the PIV software the match a particle pair when the distance between them is around 10 pixels when a  $32 \times 32$  pixels interrogation window is used. Therefore the time interval between consecutive images should is set to allow a seeding particle to move 10 pixels pair in general.

As mention above, the resolution of the camera is  $2048 \times 1088$  pixels and the dimension of the test section facing the camera is  $76.2mm \times 38.1mm$ . Thus the scale/pixel factor is calculated shown in equation (3.1):

$$\frac{76.2mm}{2048pixels} = \frac{0.0372mm}{pixel} = \frac{0.372mm}{10pixels}. \quad (3.2)$$



Base on the scale/pixel factor calculation the seeding particle should ideally move 0.372mm during the time interval set by the frame rate. In addition from the velocity computed above the time interval is estimated by

$$\Delta t = 0.372mm/U_{max} \quad (3.3)$$

where  $U_{max}$  is the maximum velocities in the flow filed. For laminar pipe flow where the geometry of the pipe cross section is square, the ratio between the maximum velocity and averaged velocity is not two which is true for cylindrical pipe. However, we still use ratio two here for estimation.  $U_p$  calculated before and the results are shown in Table 2.4, and frame rate is then

$$fps = \frac{1}{\Delta t}. \quad (3.4)$$

The fps at different Reynolds numbers is summarized in table 3.1. As it is cited before that the highest frame rate of Flare camera is 300 thus the continuous PIV system can only effectively acquire the images for PIV analysis when Reynolds number less than 300. When Reynolds number is higher than 300, a pulsed PIV system should be used instead.

### 3.3 Pulsed PIV System

Compared with continuous PIV system, pulsed PIV system is able to grab images when Reynolds number is higher than 300 in this experiment. In continuous PIV system the images are grabbed by the high-speed camera continuously . For pulsed PIV system, the CCD camera is operated at a setting frequency and each time an image pair is grabbed for PIV post-processing. The time interval between the two images can be much shorter than that of continuous PIV system, because the PIV camera is designed to operate under a special double-exposure mode for PIV recording. Moreover, a synchronizer is indispensable in pulsed PIV system since the laser and

CCD camera must be synchronized to operate simultaneously. In this experiment, a LaVision PIV system is used and  $\Delta t$  is set as short as 10 microsecond [45].

The LaVision PIV system is composed of one ImagerProX camera to record the images, a twin-headed Nd:YAG to illuminate the test section, as well as image recording hardwares. The camera has  $2048 \times 2048$  pixels in the present experiment. It operates under double exposure mode with a sample rate of 6 Hz. The time delay between the two pulse is set based on frame rate estimation mentioned in the previous section. The schematics of pulsed PIV system is shown in Figure 3.6.

### 3.3.1 Nd:YAG Laser

Every laser consists of three main components: a laser material, a pump source and an oscillator, a typical layout of a dual oscillator Nd:YAG is shown in Figure 3.7. Nd:YAG is the the most important solid-state laser for PIV in which the beam is generated by  $Nd^{3+}$  ions. The  $Nd^{3+}$  ion is incorporated with YAG crystals (yttrium-aluminum-garnet). The pump usually is a krypton flashlamp or a smaller semiconductor laser. The resonator is a set of high reflective mirrors, usually in a stable configuration in order to generate a Gaussian beam profile. A quality switch (Q-switch) inside the cavity is introduced so the laser can be operated in a triggered mode. The Q-switch has the effect of altering the resonance characteristics of the optical cavity. If the Q-switch is operated, allowing the cavity to resonate at the most energetic point during the flash lamp cycle, a very powerful laser pulse, the giant pulse, can be achieved. At the beginning of the pump process (i.e. the start of one flashlamp pulse) the Q-Switch is closed, so no laser oscillation and amplification is possible. After the stored energy in the resonator reached its maximum the Q-Switch is opened and the laser oscillation begins immediately and the stored energy is extracted in a pulse of a few nanoseconds duration. The process is shown in Figure 3.8. Although Q-switches can be used to generate more than one giant pulse out of one resonator, PIV lasers are mostly designed as double oscillator systems. This enables

the user to adjust the separation time between the two illuminations of the tracer particles independently of the pulse strength. For PIV the fundamental wavelength of 1064nm is frequency doubled using a nonlinear crystal as second harmonic generator (SHG) which converts the IR (Infrared Radiation) light to visible green light of 532nm [23, 46].

### 3.4 Optical System

In a PIV system optical system is used to expand a laser beam into laser sheet to illuminate the test section. In addition the laser sheet should be thin enough that the seeding particles within that plane are illuminated. There are at least two lenses, a cylindrical lens and spherical lens. Since cylindrical lens only affect the incoming light in one direction and has no influence in the perpendicular direction, it is used to expand the laser beam.

In order to determine how large the laser beam should be expanded the features of a laser beam are needed. A standard laser beams can be as Gaussian beams, which is a beam of electromagnetic radiation whose transverse electric field and intensity (irradiance) distributions are well approximated by Gaussian functions. When a lasers emits beam of a Gaussian profile, the laser is operated on the fundamental transverse mode, or “TEM00 mode” of the laser’s optical resonator. A typical intensity profile of a Gaussian beam is shown in Figure 3.9.

Thus it is obvious the intensity of the beam is not a normal distribution. The seeding particles may not be illuminated with a same luminance as a result and it will affect the accuracy of PIV measurement. Since the Gaussian profile is one feature of the laser and it cannot be adjusted. It is needed to expand the laser beam longer than the test section. So the seeding particles could be illuminated only by the central part of that laser sheet. In this experiment one cylindrical lens ( $f_1$ ), a concave spherical lens ( $f_2$ ) and a spherical convex lens ( $f_3$ ) are used to constitute the optical system and their optical parameters are listed in Table 3.2.

The cross area of the laser beam is circular with a diameter of 2 mm. On the one direction it is expanded to a line which is longer than the test section and on the perpendicular direction it is focused. In this way when the laser propagates in the test section it is long enough to illuminate the whole test section at an approximately constant luminance and thin enough that only the flow field in the middle of the test section is illuminated.

This optical system is designed using image formation equation of thin lens

$$\frac{1}{s} + \frac{1}{s'} = \frac{1}{f} \quad (3.5)$$

where  $s$  is the object distance and  $s'$  is the image distance. A positive number for  $s$  and  $s'$  indicates the image or object is real and a negative number indicates the image or object is virtual.

In order to determine the relative distance between the lenses, equation 3.4 is used to calculate the focal length of the optical system (combination of three lenses). Moreover any ray that enters parallelly to the axis on one side of the lens proceeds towards the focal point  $F$  on the other side; any ray that passes through the center of the lens will not change its direction; and any ray that arrives at the lens after passing through the focal point on the front side comes out parallelly to the axis on the other side. The optical system setup is shown in Figure 3.10.  $X$  is the distance between  $f_1$  and  $f_2$ ,  $Y$  is the distance between  $f_2$  and  $f_3$ .

From Table 3.2 we know that the focal length for cylindrical lens is much smaller than the concave spherical lens, therefore the cylindrical lens will be deterministic for the expanded laser width. There is only one convex lens that used in the experiment with a focal length of 175 mm. If the distance between optical system and the test section is 175 mm, the laser will be focused before it is expanded to a ideal length. The spherical concave lens is used to help the laser focus slower than with only the convex lens and give it enough optical path to expand. The longer the distance between the optical system and the test section, the spanning area of laser sheet will be larger.

The spherical lens is used to adjust the  $F_{total}$  of the system.  $F_{total}$  is defined as the distance over which initially collimated rays are brought to a focus. In addition,  $H$  is defined as the length of the laser sheet at distance  $F_{total}$ . Note that the space to arrange the instrument next to the facility is limited so an optimal optical system design is necessary. The estimation of optical system design is summarized in Table 3.3.

From Table 3.3, it is obvious that  $X$  could be viewed as irrelevant to  $F_{total}$  and  $H$ . A shorter  $y$  leads to a larger  $H$ . The test section is 76.2 mm long. Thus in the experiment we make the  $y$  value as smaller as possible. The computed result is only an estimated result and the detailed configuration during experiment process. In the present study,  $X$  is 3 mm and  $Y$  is 3 mm which are the shortest length available.

### 3.5 Measuring Velocity Field using PIV

The water is uniformly seeded with hollow glass beads (median diameter 11  $\mu\text{m}$ , specific gravity 1.1) for PIV measurement. Velocity field is retrieved by processing image pairs using PIV post-processing software DaVis 7.2. A one step process is applied: a  $32 \times 32$  pixels interrogation window and 50% overlap. A total of  $128 \times 68$  vectors are resolved for each image pair. The typical uncertainty estimate of the instantaneous PIV data is about 0.15 pixels, corresponding to an uncertainty of 1% [25].

Table 3.1. Fps for different Reynolds number.

<b>Re</b>	<b><math>U_{max}</math>(mm/s)</b>	<b><math>\Delta t</math>(ms)</b>	<b>fps</b>
60	23.6	15.74	64
80	31.5	12.79	85
100	39.4	9.43	106
200	78.9	4.72	212
500	197.2	1.89	530
700	276.1	1.35	742

Table 3.2. Focal length for lenses using in the experiment.

	<b>Focal length</b>
Cylindrical (Concave)	$f_1=-20\text{mm}$
Spherical (Concave)	$f_2=-200\text{mm}$
Spherical (Convex)	$f_3=175\text{mm}$

Table 3.3. Focal length ( $F_{total}$ ) and laser sheet length at distance  $F_{total}$  of optical system.

<b>X (mm)</b>	<b>Y (mm)</b>	<b><math>F_{total}</math> (mm)</b>	<b>H (mm)</b>
10	5	1195.8	116.7
10	7	1132.0	109.4
10	9	1075.7	102.9
5	10	1050.0	100.0
7	10	1050.0	100.0
9	10	1050.0	100.0

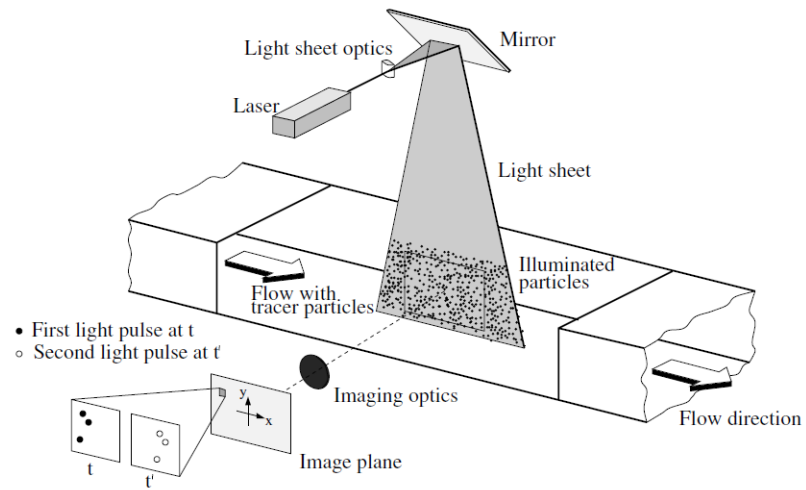


Figure 3.1. Experimental arrangement for particle image velocimetry [23].

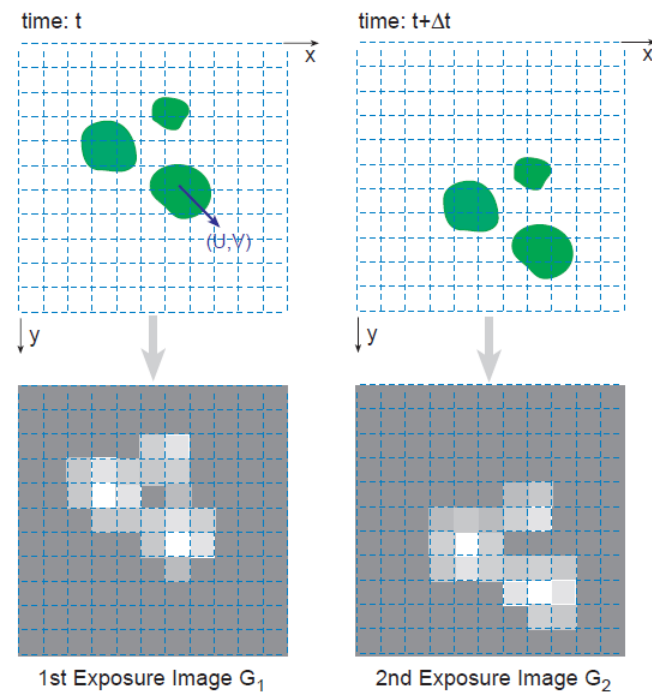


Figure 3.2. PIV double exposure recording process: (top) particle patterns moving at displacement  $(U, V)$ , and (bottom) particle pattern images recorded by the digital camera [51].



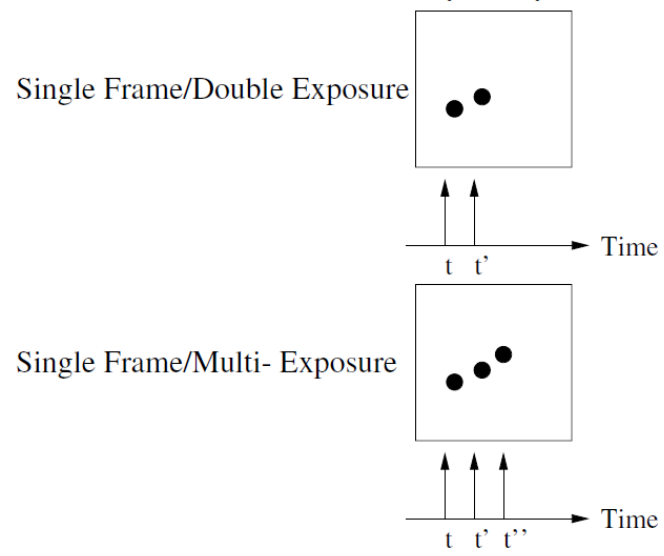


Figure 3.3. Single frame/multi-exposure PIV [23].

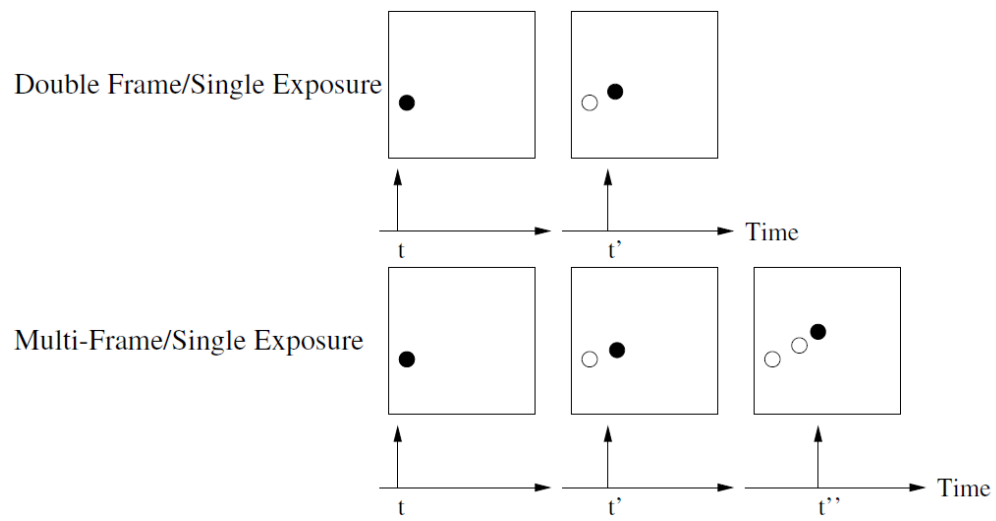


Figure 3.4. Multi-frame/single exposure PIV [23].

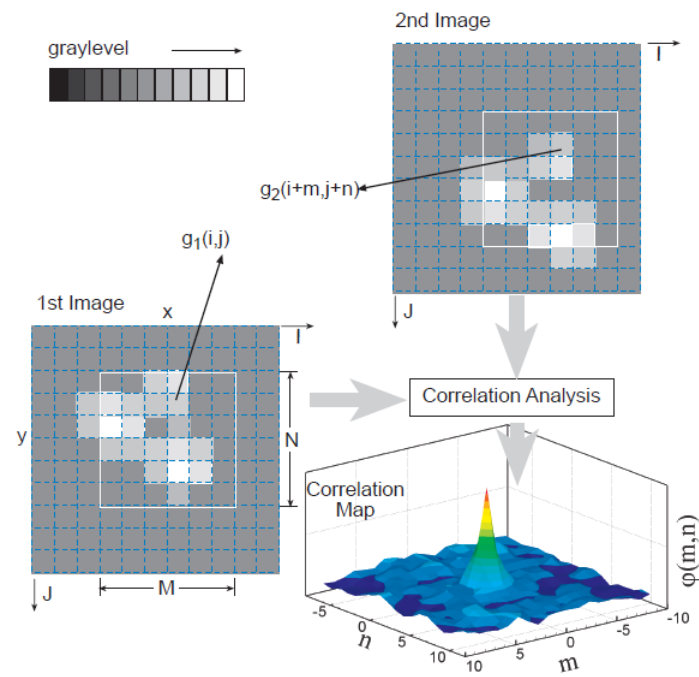


Figure 3.5. Sample pair of interrogation windows and the corresponding distribution of the cross correlation function  $\phi(m, n)$  [51].

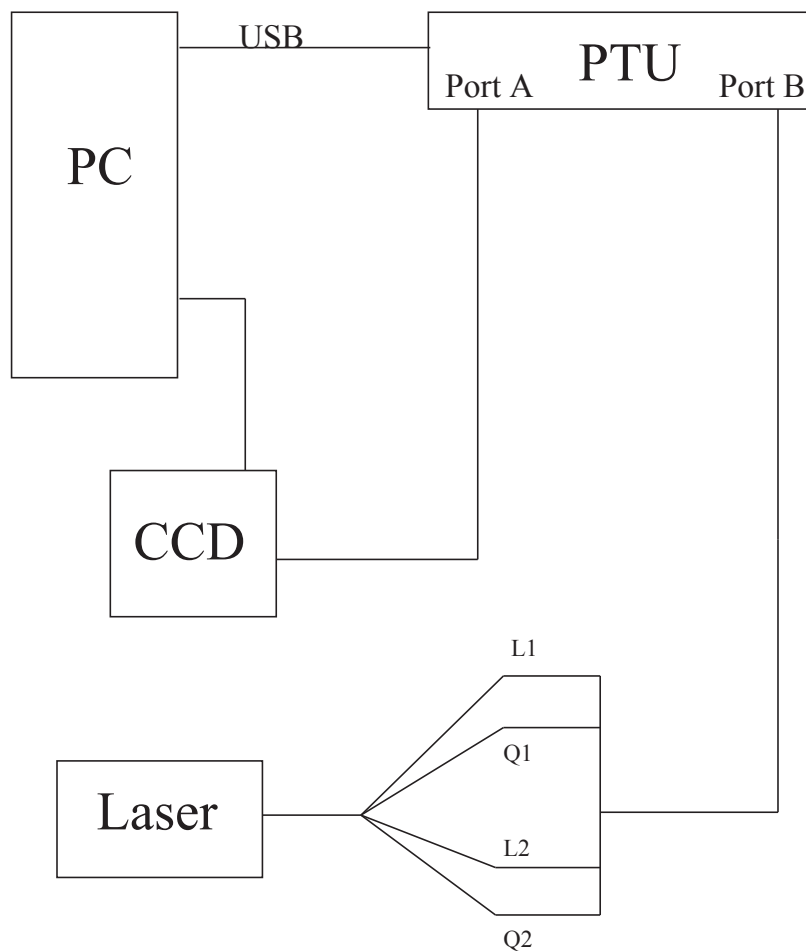


Figure 3.6. Schematics for pulsed PIV system. PTU stands for Programmable Timing Unit.  $L_1$  is “Flashlamp” trigger for laser 1,  $Q_1$  is the “Q-switch” trigger for laser 1;  $L_2$  is “Flashlamp” trigger for laser 2,  $Q_2$  is the “Q-switch” trigger for laser 2.

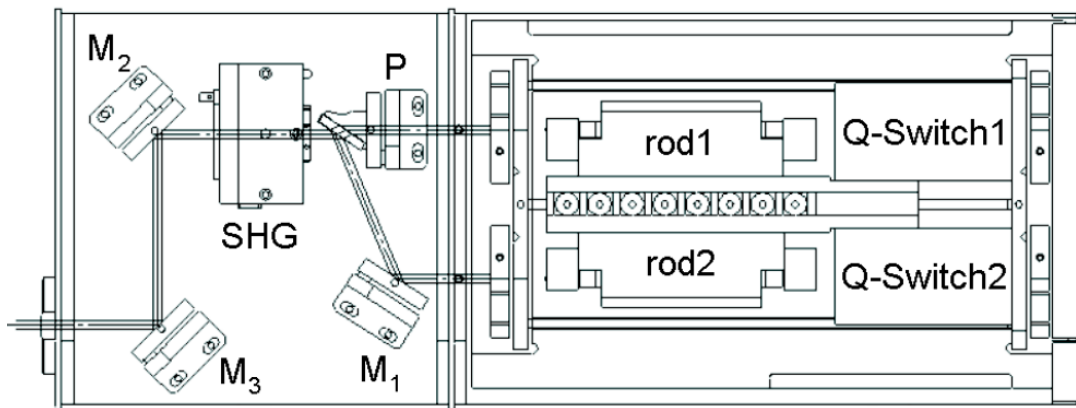


Figure 3.7. Typical layout of a dual oscillator Nd:YAG. rod1, rod2: laser crystal, M1, M2, M3: mirrors, P: beam combining polarizer, SHG: second harmonic generator [46].

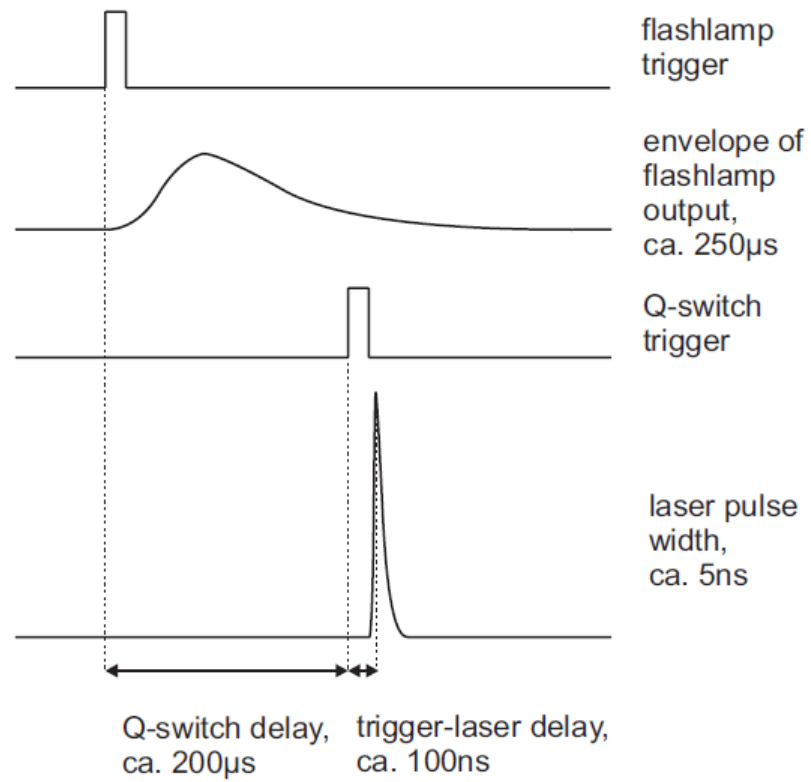


Figure 3.8. The Q-Switch allows the cavity to resonate in the most energetic point during the flashlamp cycle [46].

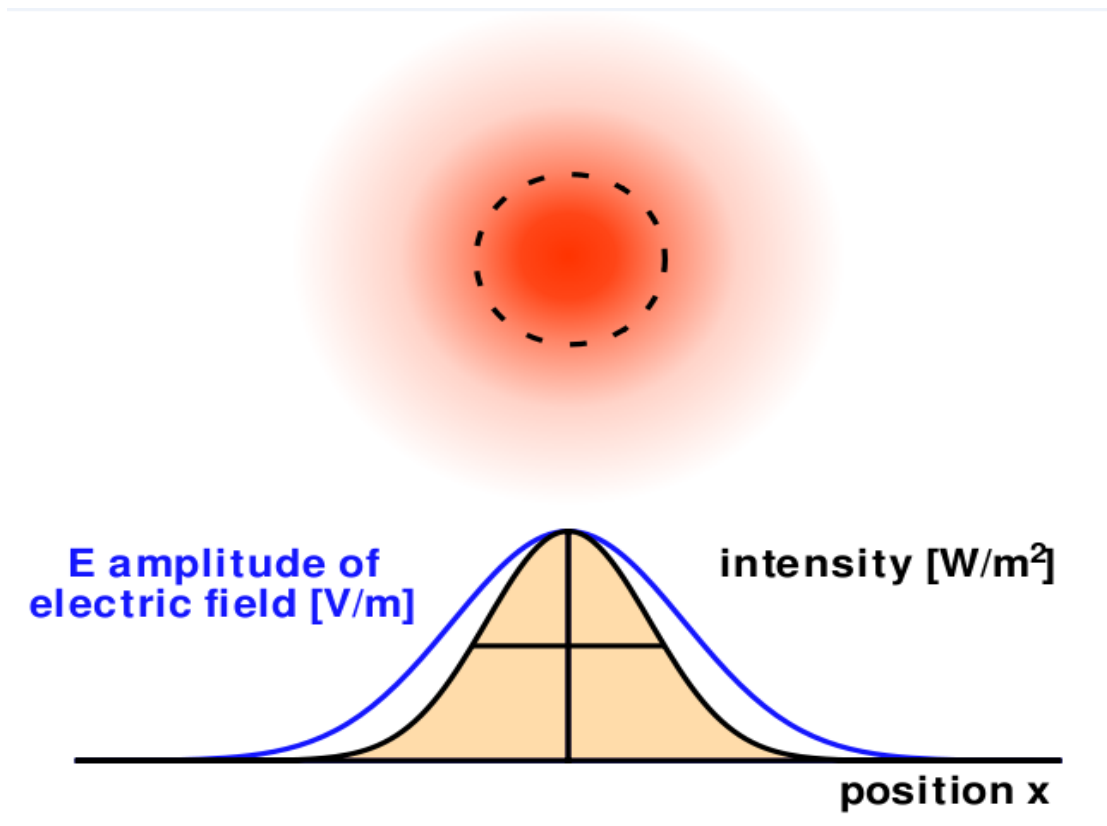


Figure 3.9. Intensity profile of a Gaussian beam.

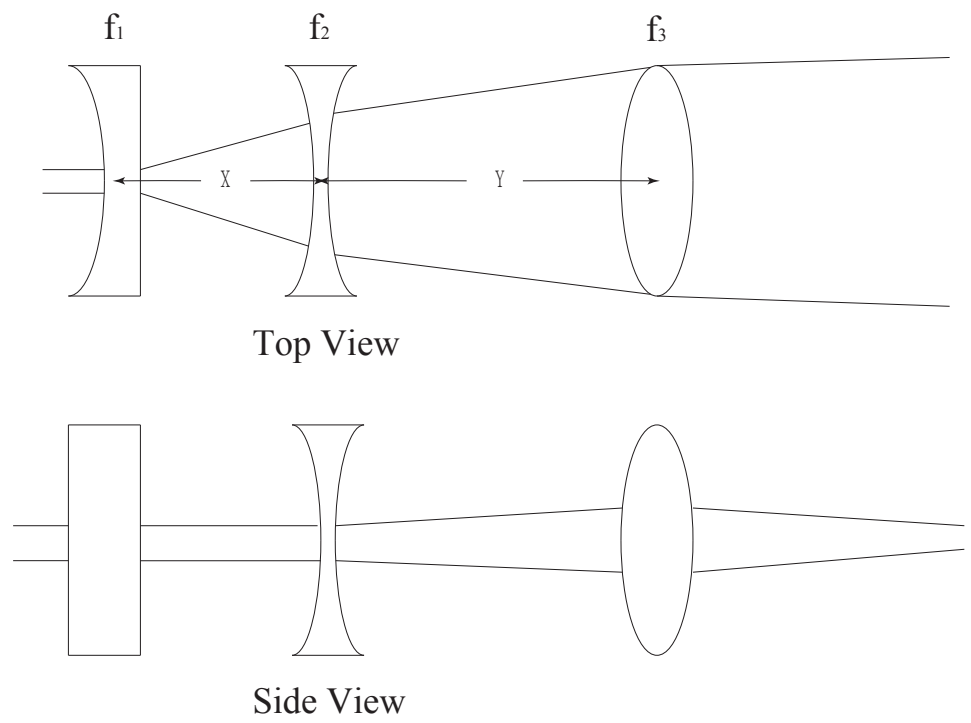


Figure 3.10. Schematics of optical system.



## 4. FLOW FIELD WITH SYMMETRIC INLET AND OUTLET

There are two test sections mentioned in the second chapter, one with symmetric inlet and outlet flow while the other one adds a symmetric perturbation on it. The velocity field could be acquired for both test sections under different Reynolds number. Moreover, in order to find the relationship between asymmetry of velocity, kinetic energy as well as vorticity, different dimensionless numbers are defined to apply  $\mathcal{PT}$ -symmetric theory. The flow field in test section shown in Figure 2.1 is analyzed in this chapter.

### 4.1 Formalism

First of all, we need to define the  $\mathcal{PT}$ -symmetry of fluids which is motivated by the balanced inlet/outlet flow. The fundamental requirement for  $\mathcal{PT}$ -symmetric flow field is that the total mass flux at the inlet and outlet must be identical. Moreover, balanced situation could be different based on different definitions that mainly concerns about the symmetric velocity profile. For example, in Figure 4.1, two distinct symmetric flow fields are introduced. The flow field is in a square domain with  $M$  side length. Their balanced situation is defined by different parity ( $\mathcal{P}$ ) operators. In plot (a) the parity operator  $\mathcal{P}_O$  is introduced for corresponding flow field

$$\mathcal{P}_O(\mathbf{r}) = \mathcal{P}_O(x, y) = (-y, -x) = \mathbf{r}_O, \quad (4.1)$$

$$\mathcal{P}_O(\mathbf{u}(\mathbf{r})) = \mathcal{P}_O(u_x(\mathbf{r}), u_y(\mathbf{r})) = (-u_y(\mathbf{r}_O), -u_x(\mathbf{r}_O)) = \mathbf{u}_O(\mathbf{r}_O). \quad (4.2)$$

Here  $\mathbf{r} = (x, y)$  represents the position of any point in flow field and  $\mathbf{r}_O$  represents the position after  $\mathcal{P}_O$  operation.  $\mathbf{u}(\mathbf{r}) = (u_x(\mathbf{r}), u_y(\mathbf{r}))$  represents the velocity field of the

original flow field and  $\mathbf{u}_O(\mathbf{r}_O)$  represents the velocity field after  $\mathcal{P}_O$  operation. The parity operator in plot (a) is an odd parity operator and this parity operator satisfies

$$\det \mathcal{P}_O = -1, \quad (4.3)$$

and

$$\mathcal{P}_O^2 = 1 \quad (4.4)$$

where *det* is the mathematical determinant.

In plot (b) the parity operator  $\mathcal{P}_y$  is defined as

$$\mathcal{P}_y(\mathbf{r}) = \mathcal{P}_y(x, y) = (-x, -y) = \mathbf{r}_y, \quad (4.5)$$

$$\mathcal{P}_y(\mathbf{u}(\mathbf{r})) = \mathcal{P}_y(u_x(\mathbf{r}), u_y(\mathbf{r})) = (-u_x(\mathbf{r}_y), -u_y(\mathbf{r}_y)) = \mathbf{u}_y(\mathbf{r}_y). \quad (4.6)$$

Here  $\mathbf{r}_y$  represents the position after  $\mathcal{P}_y$  operation and  $\mathbf{u}_y(\mathbf{r}_y)$  represents the velocity field after  $\mathcal{P}_y$  operation. The parity operator in plot (b) is an even parity operator and this parity operator satisfies

$$\det \mathcal{P}_y = 1, \quad (4.7)$$

and

$$\mathcal{P}_y^2 = 1. \quad (4.8)$$

In both cases the velocity field is odd under time reversal ( $\mathcal{T}$ ) operation

$$\mathcal{T}(\mathbf{u}(\mathbf{r})) = -\mathbf{u}(\mathbf{r}), \quad (4.9)$$

thus the combined parity reflection and time reversal lead to

$$\mathcal{P}_O \mathcal{T}(\mathbf{u}(\mathbf{r})) = \mathbf{u}(\mathbf{r}_O), \quad (4.10)$$

and

$$\mathcal{P}_y \mathcal{T}(\mathbf{u}(\mathbf{r})) = \mathbf{u}(\mathbf{r}_y). \quad (4.11)$$

Our first set experiments represent a special case for (b) where  $a = 0$ . It is commonly believed that the fluid will obey the non-slip boundary condition and for our one-dimensional special case the boundary conditions are  $\mathcal{PT}$ -symmetric for parity operator  $\mathcal{P}_y$ . A dimensionless characteristic number for  $\mathcal{PT}$  asymmetry in steady state flow field  $\mathbf{u}(\mathbf{r})$  is defined as [50]

$$\rho^u = \frac{1}{2M^2U_p^2} \int d\mathbf{r} [(\mathcal{PT}\mathbf{u})(\mathbf{r}) - \mathbf{u}(\mathcal{P}(\mathbf{r}))]^2. \quad (4.12)$$

The integral domain is the whole flow field, in plot (a) and (b) it is  $x = [-M/2, M/2]$ ,  $y = [-M/2, M/2]$ . The dimensionless number  $\rho^u$  gives the asymmetry for velocity field. The asymmetry can also be computed for kinetic energy field as well as vorticity field. The dimensionless number of  $\mathcal{PT}$  asymmetry for kinetic energy field and the dimensionless number of  $\mathcal{PT}$  asymmetry for vorticity field, are:

$$\rho^K = \frac{1}{2M^2U_p^2} \int d\mathbf{r} [(\mathcal{PT}K)(\mathbf{r}) - K(\mathcal{P}(\mathbf{r}))]^2, \quad (4.13)$$

and

$$\rho^\omega = \frac{1}{2M^2U_p^2} \int d\mathbf{r} [(\mathcal{PT}\omega)(\mathbf{r}) - \omega(\mathcal{P}(\mathbf{r}))]^2 \quad (4.14)$$

$\mathbf{K}(\mathbf{r})$  is the kinetic energy which is defined as  $\mathbf{K}(\mathbf{r}) = \frac{\rho \mathbf{u}^2(\mathbf{r})}{2}$ .  $\omega(\mathbf{r})$  is the vorticity which is defined as  $\omega(\mathbf{r}) = \nabla \times \mathbf{u}(\mathbf{r})$  where  $\nabla \times$  is the curl operation, in Cartesian coordinates the curl is defined as

$$\nabla \times \mathbf{F} = \left( \frac{\partial F_z}{\partial y} - \frac{\partial F_y}{\partial z} \right) \hat{i} + \left( \frac{\partial F_x}{\partial z} - \frac{\partial F_z}{\partial x} \right) \hat{j} + \left( \frac{\partial F_y}{\partial x} - \frac{\partial F_x}{\partial y} \right) \hat{k} \quad (4.15)$$

where  $\mathbf{F}$  is a vector field and  $\hat{i}, \hat{j}, \hat{k}$  are the unit vectors in x, y, z direction. Equation (4.12), (4.13) and (4.14) are applicable for both two-dimensional and three-dimensional velocity field. In the present study a two-dimensional velocity field is

measured for asymmetry calculation. There are two parity operators mentioned before, one is odd and the other one is even. Our experiment test section satisfies symmetric boundary condition only for even parity operator, thus asymmetry through origin is calculated. In addition, our test section is a special case for plot (b) where  $a = 0$ , the asymmetry about y-axis is calculated.

The velocity field measured by PIV is discrete instead of a continuous one. Equation (4.12), (4.13) and (4.14) are modified to calculate the asymmetry for velocity, kinetic energy and vorticity. Equation (4.16)-(4.21) shows how to retrieve the  $\mathcal{PT}$  asymmetries using discrete velocity data,  $\rho_1$  is the asymmetry through origin and  $\rho_2$  is the asymmetry about y-axis:

$$\rho_1^u = \frac{1}{U_p^2 \times N_x \times N_y} \sum_{x>0,y} [u_x(x, y) - u_x(-x, -y)]^2 + [u_y(x, y) - u_y(-x, -y)]^2, \quad (4.16)$$

and

$$\rho_1^K = \frac{1}{(0.5\rho U_p^2)^2 \times N_x \times N_y} \sum_{x>0,y} [K(x, y) - K(-x, -y)]^2, \quad (4.17)$$

and

$$\rho_1^\omega = \frac{1}{\left(\frac{U_p}{W}\right)^2 \times N_x \times N_y} \sum_{x>0,y} [\omega(x, y) + \omega(-x, -y)]^2, \quad (4.18)$$

and

$$\rho_2^u = \frac{1}{U_p^2 \times N_x \times N_y} \sum_{x>0,y} [u_x(x, y) - u_x(-x, y)]^2 + [u_y(x, y) + u_y(-x, y)]^2, \quad (4.19)$$

and

$$\rho_2^K = \frac{1}{(0.5\rho U_p^2)^2 \times N_x \times N_y} \sum_{x>0,y} [K(x, y) - K(-x, y)]^2, \quad (4.20)$$

and

$$\rho_2^\omega = \frac{1}{\left(\frac{U_p}{W}\right)^2 \times N_x \times N_y} \sum_{x>0,y} [\omega(x, y) - \omega(-x, y)]^2. \quad (4.21)$$

In equation (4.18) and (4.21),  $W$  is the width of inlet and outlet tubing which is 2.54 mm in our experiment,  $N_x$  the number of grid along x direction, and  $N_y$  the number of grid along y direction,  $\omega(x, y)$  the magnitude of vorticity at position  $(x, y)$ , and  $U_p$  the averaged flow velocity at the exit of inlet tubing. The coordinate system to define the position  $(x, y)$  is shown in Figure 4.2, where the origin of coordinate is located at the center of the test section. In the present study, a three-dimensional flow field is generate, however the PIV data can only describe a two-dimensional velocity field. The two-dimensional velocity field is the one located at the center of the test section and it is used to analyze the asymmetry of the flow field.

## 4.2 Results

The Reynolds number in this experiment ranges from 60 to 700 as mentioned before. The volumetric flow rate is controlled by the syringe pumps. An important factor that influences the measurement at low Reynolds number is density difference. We commonly believed that the density of water is a constant however this is true only when temperature is fixed. The density of water will fluctuate as temperature varies. If the water density at the inlet tubing is different from the water density in test section, this will result in differences in flow field. Since we will analyze the flow field under  $\mathcal{PT}$ -symmetric condition, the fluid itself must be homogeneous. If there is density difference of the fluid in the test section, the symmetric condition is not be guaranteed. At the beginning of this experiment, some interesting velocity fields were observed because of the density difference at very low Reynolds number ( $Re \leq 60$ ). The inlet flow went upwards or downwards beside from left to right. To further justify this phenomenon we first filled up the test section with room-temperature water and then injected iced water. The inlet flow went downwards besides went from left to right. In addition, we filled up the test section with iced water and injected room-temperature water. The inlet flow went upwards besides went from left to right. Therefore we drew a conclusion that the density difference can influence the flow field. Another factor

that will influence the result is the gas contained in the water. Tap water dissolves air in it and when temperature changes small bubbles are formed which will stick on the inner surface of the test section and the flow field will be influenced. Therefore to avoid their influence, first we use deionized water instead of tap water. Then we put the water in lab for enough long time, over night in general, to ensure the water stays at constant room temperature.

Figure 4.4 shows averaged velocity fields for our experiment as a function of inlet velocity, i.e. Reynolds number. In Figure 4.3, the contour is the non-dimensional velocity field and the streamlines are also plotted using Tecplot. Streamlines are a family of curves that are instantaneously tangent to the velocity vector of the flow. These show the direction a fluid element will travel in at any point in time. The mathematical description of two-dimensional streamline  $\mathbf{x}_s = (x_s, y_s)$  is

$$\frac{dx_s}{u_x} = \frac{dy_s}{u_y} \quad (4.22)$$

where  $u_x$  and  $u_y$  are the x and y component of velocity. The vorticity fields are shown in Figure 4.5. and the kinetic energy fields are shown in Figure 4.6. The kinetic energy fields and vorticity fields are calculated and plotted using TecPlot, in TecPlot one can choose Calculate Variables to retrieve the kinetic energy field and vorticity field. The vorticity is normalized using  $\omega W/U_p$  where  $\omega$  is Z vorticity calculated using TecPlot and kinetic energy is normalized using  $K/(U_p^2)$  where  $K = u_x^2 + u_y^2$ . The inlet fluid enters from left side and exit from the right side. Obviously the flow field is symmetric with respect to x-axis. Therefore our interest is focused on how the asymmetry situation between y-axis and origin. By using equation (4.16)-(4.21) we can obtain the dimensionless numbers that describe the asymmetry of the velocity field, kinetic energy field, and vorticity field. In this way we could quantitatively examine the asymmetries of viscous flows at different Reynolds number.

### 4.3 Discussion

Figure 4.7 shows the asymmetries of velocity ( $\rho_1^u$  and  $\rho_2^u$ ) at different Reynolds numbers. It is observed that when Reynolds number is less and equal to 100, there is a linear relationship in  $\rho_1^u$  and  $\rho_2^u$  with respect to Reynolds numbers. However, when the Reynolds number is larger than 200, the linear relationship breaks and the dimensionless asymmetry numbers decreases for  $\rho_2^u$  while increases for  $\rho_1^u$ . Moreover, when Reynolds number is less or equal to 100 the difference between  $\rho_1^u$  and  $\rho_2^u$  is significantly small, however, as Reynolds number increases the difference between them increases too. The linear relationship when Reynolds number is less than 100 is as the computational result predicted.

Figure 4.8 shows the asymmetries of vorticity ( $\rho_1^\omega$  and  $\rho_2^\omega$ ) at different Reynolds number. Unlike the trends shown in Figure 4.7. Vorticity asymmetries increase linear when Reynolds number increases. It can also be observed at low Reynolds number range ( $Re \leq 100$ ) the difference between  $\rho_1^\omega$  and  $\rho_2^\omega$  is significantly small, however the difference increases as Reynolds number increases. The linear relationship of  $\rho_1^\omega$  with respect to Reynolds number is strong.

Figure 4.9 shows the asymmetries of kinetic energy ( $\rho_1^k$  and  $\rho_2^k$ ) at different Reynolds number. Like the asymmetries of vorticity and velocity, the difference between  $\rho_1^k$  and  $\rho_2^k$  is small at low Reynolds number range and increases as Reynolds number increases. At high Reynolds number range there is an increasing trend for the asymmetry of kinetic energy to origin while the asymmetry of kinetic energy about y-axis remains at a relative constant level.

To sum up, the experimental results do not fit the computational result well in the low Reynolds number region but when Reynolds number goes beyond 200, the linear relationship of asymmetries with Reynolds number occur and more work is needed to reveal the physical nature of  $\mathcal{PT}$ -symmetric flow field.

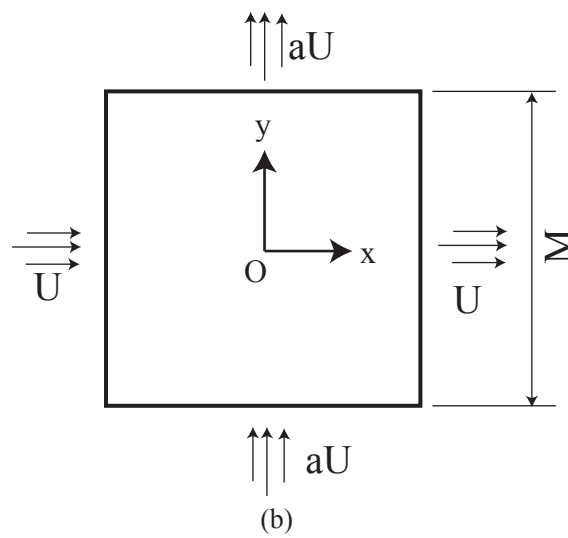
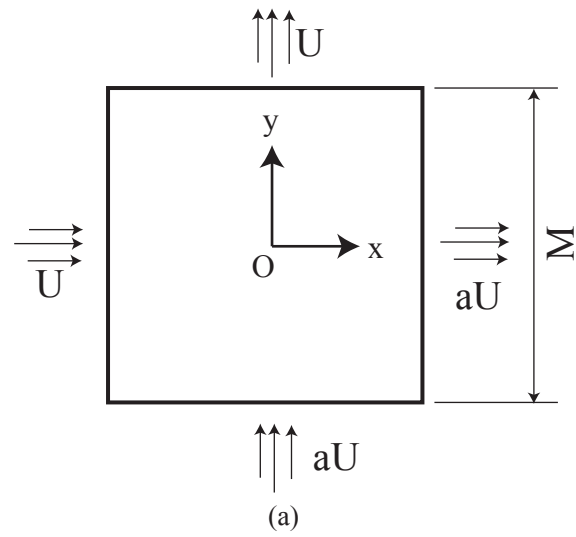


Figure 4.1. Two distinct balanced inflow/outflow system.



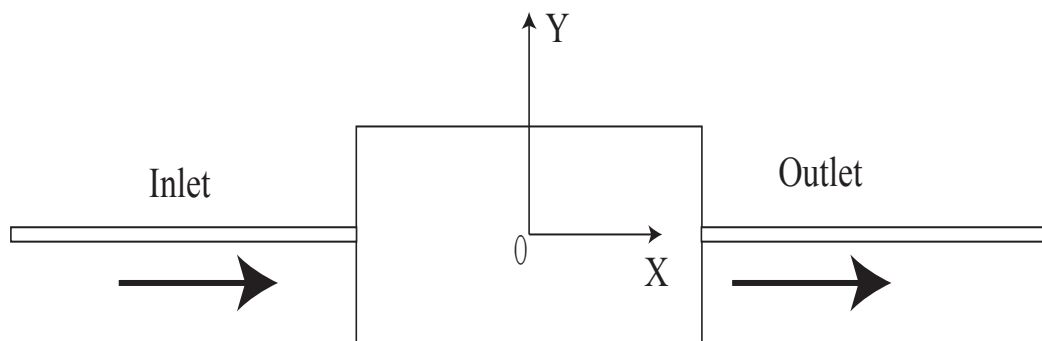


Figure 4.2. Coordinate system data analysis.

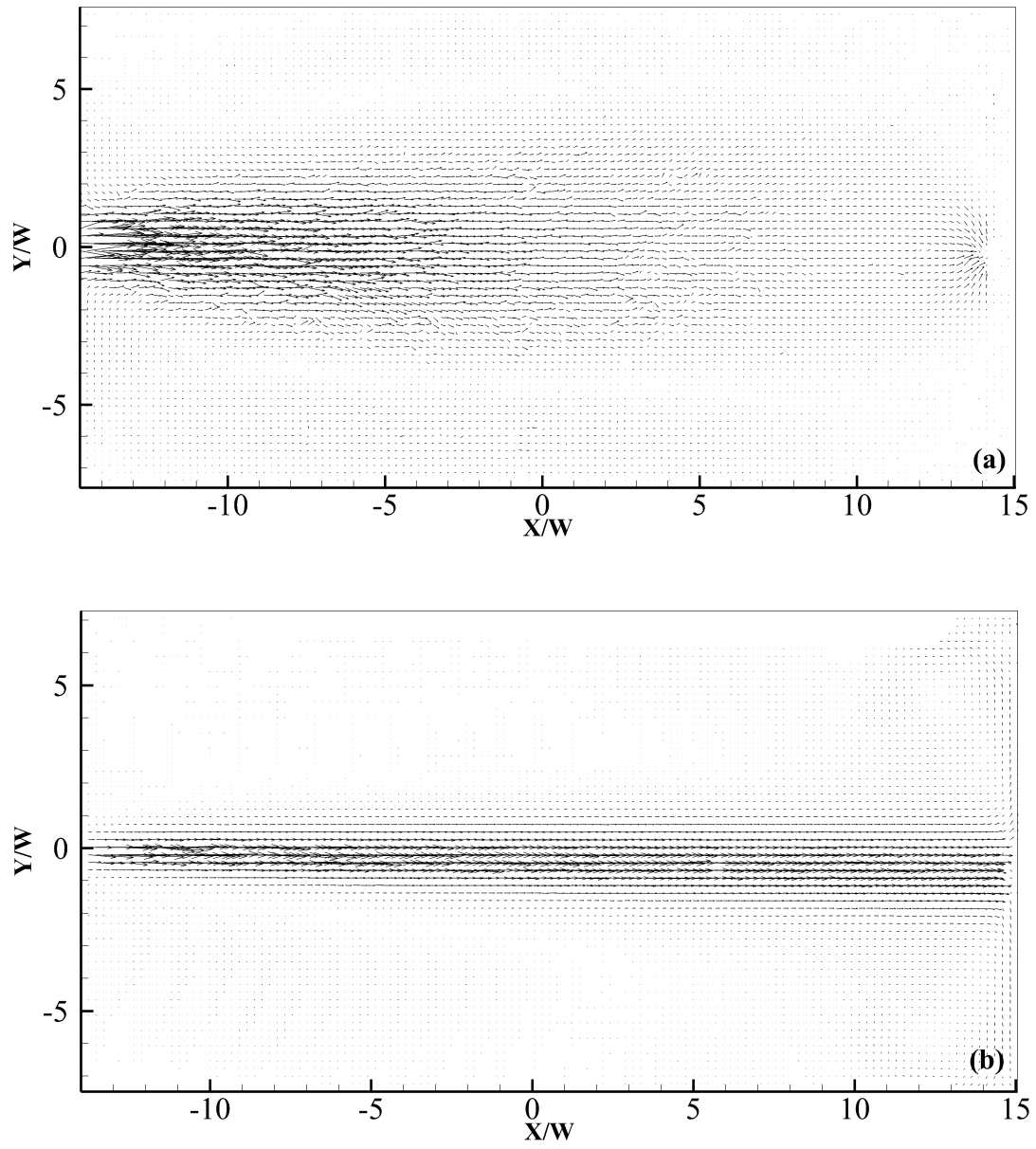


Figure 4.3. Snapshots of velocity fields, (a) $Re=60$ , (b) $Re=600$ .

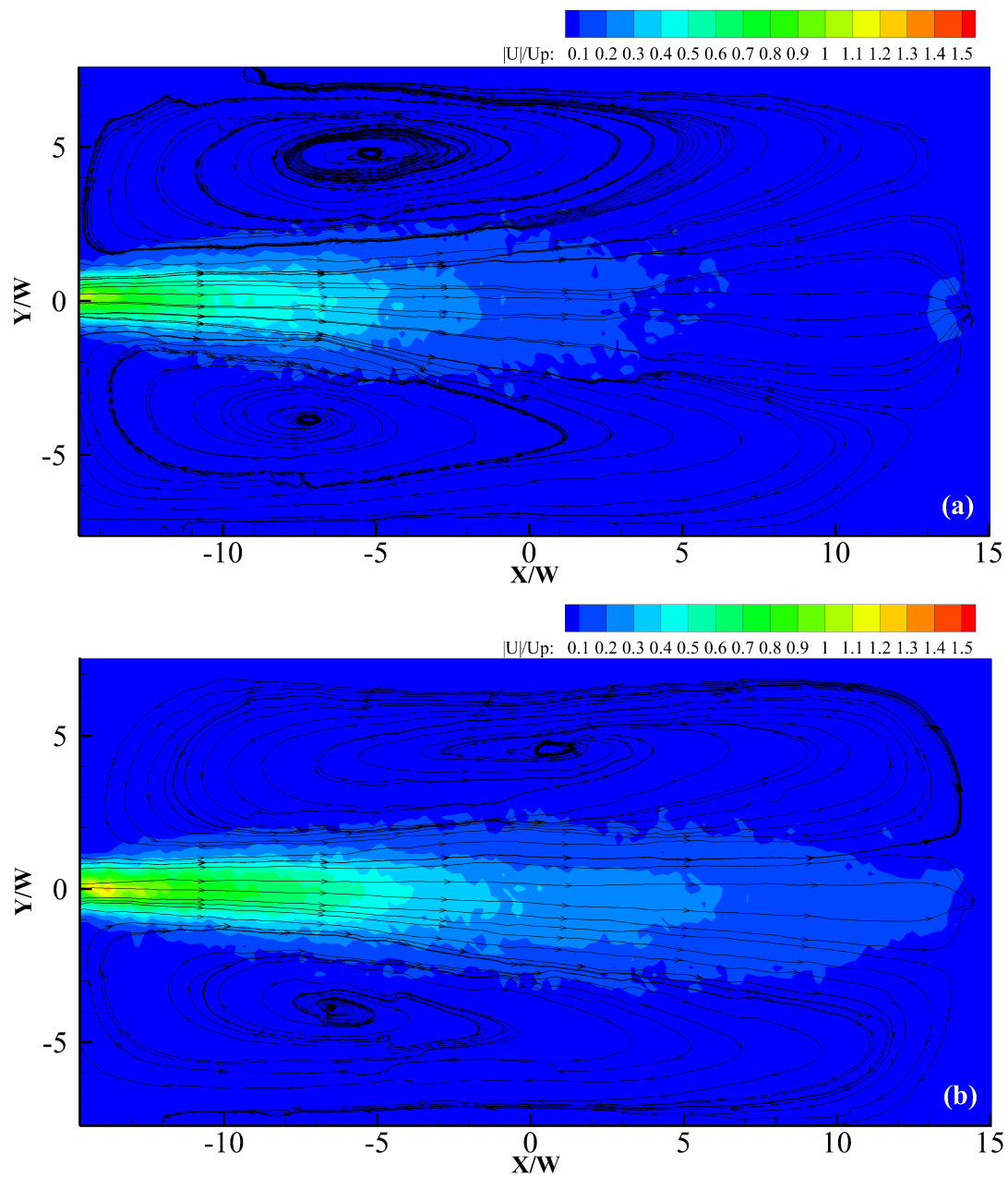


Figure 4.4. Velocity fields and streamlines for different Reynolds numbers, (a) $Re=60$ , (b) $Re=80$ , (c) $Re=100$ , (d) $Re=200$ , (e) $Re=300$ , (f) $Re=400$ , (g) $Re=500$ , (h) $Re=600$ , (i) $Re=700$ .

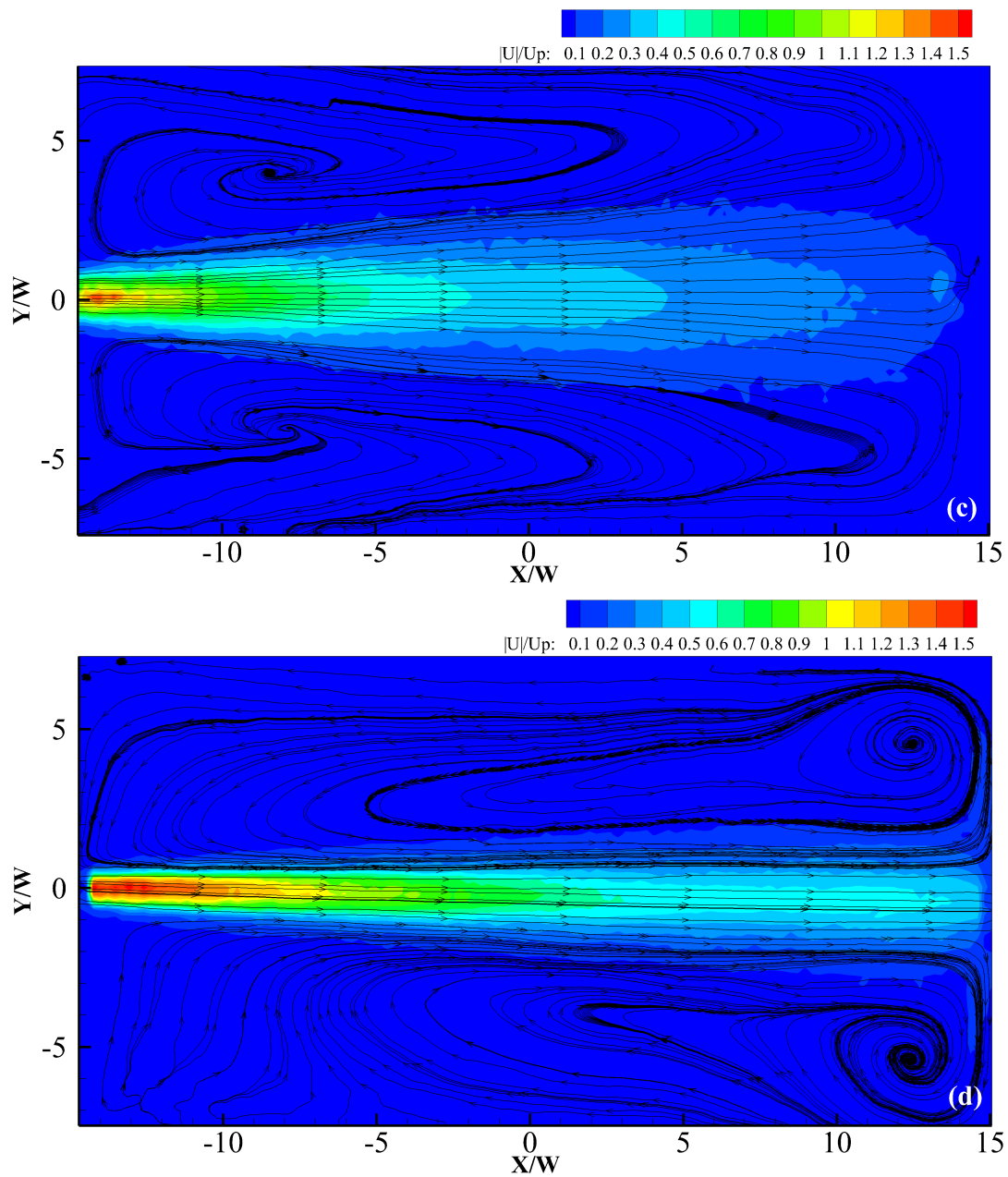


Figure 4.4. Continued.

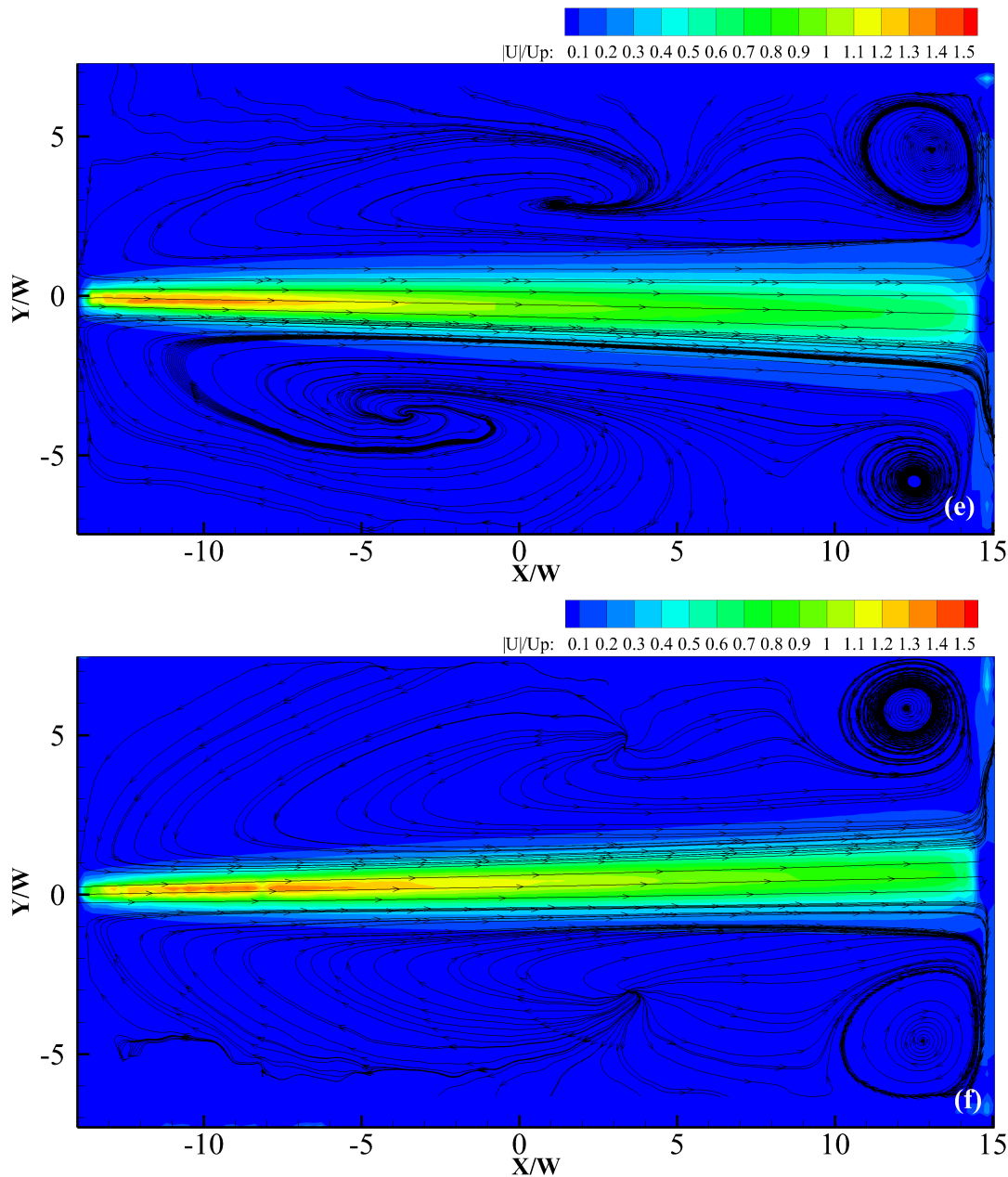


Figure 4.4. Continued.

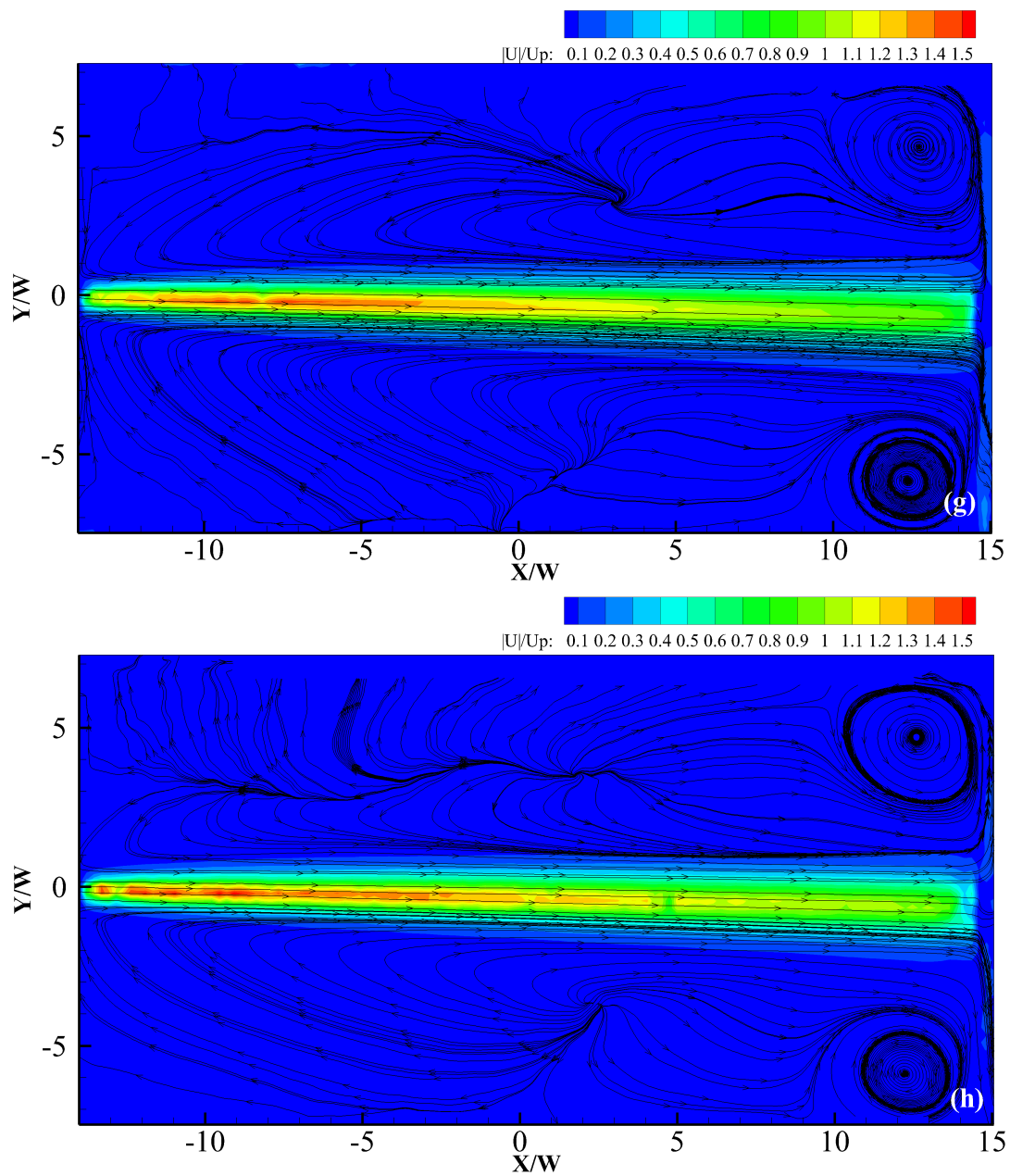


Figure 4.4. Continued.

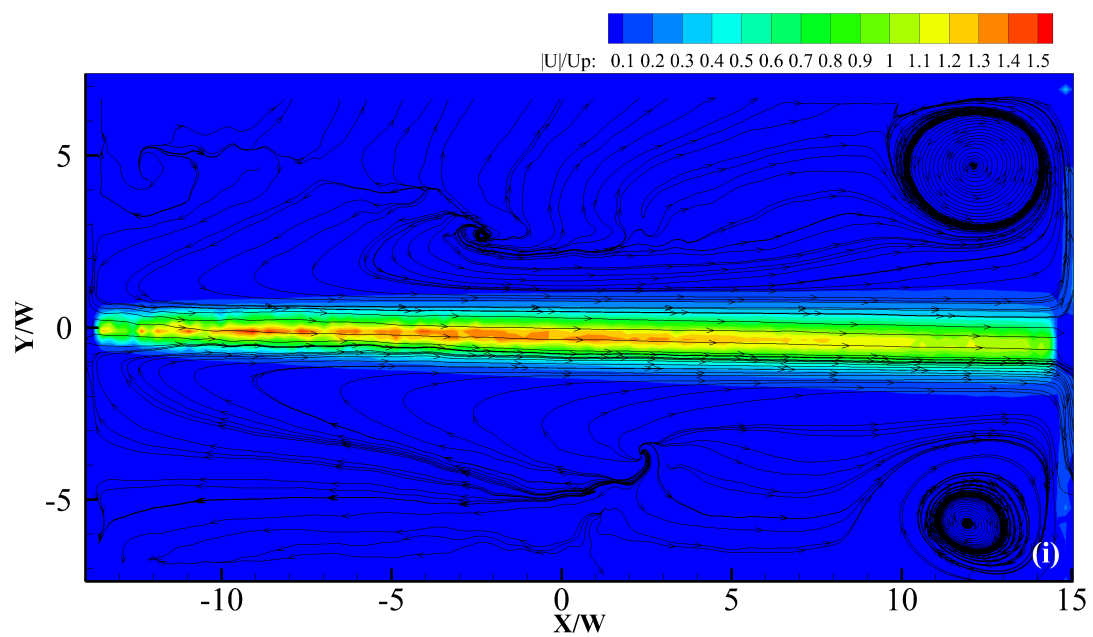


Figure 4.4.Continued.

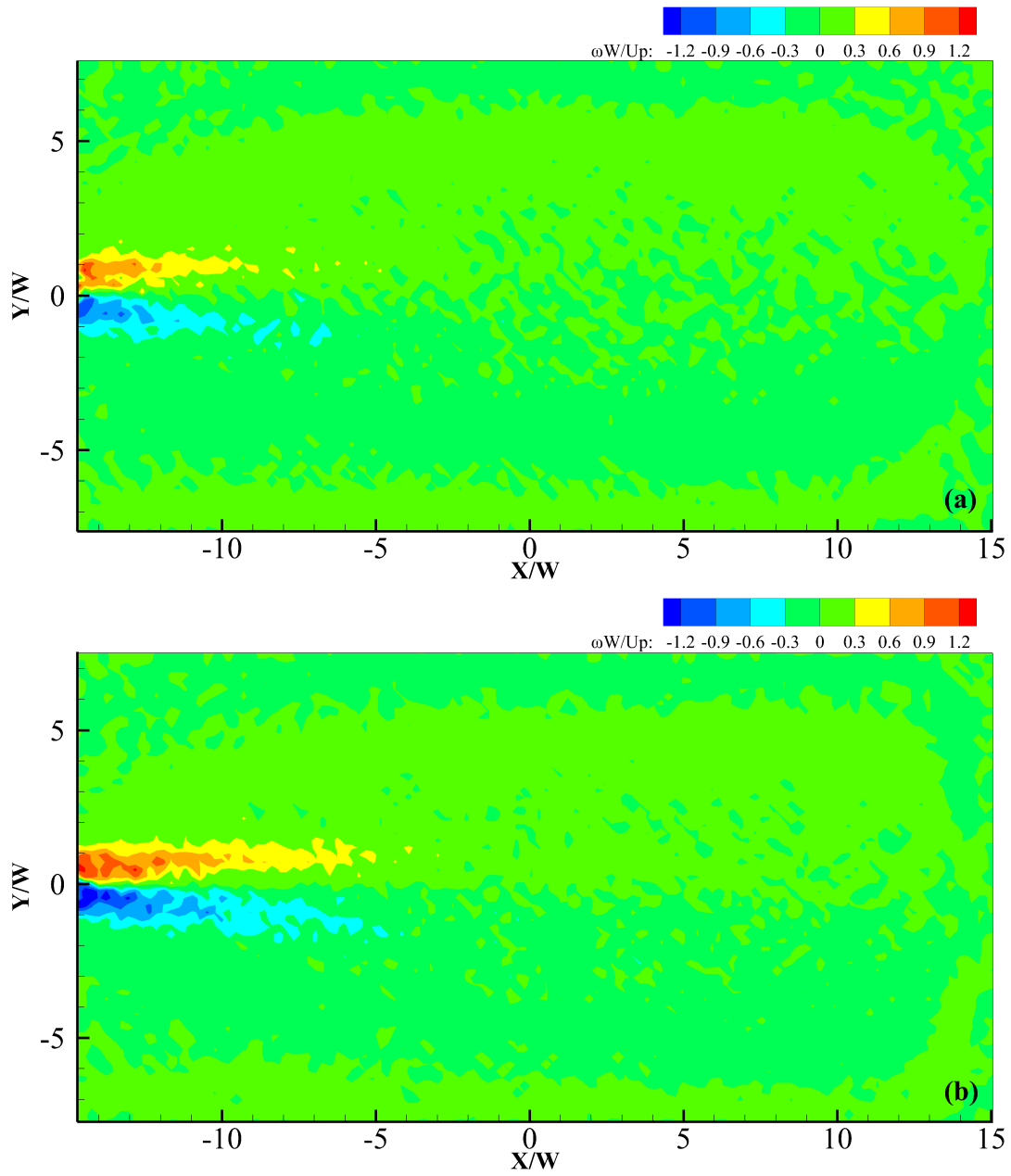


Figure 4.5. Vorticity fields for different Reynolds numbers, (a) $Re=60$ , (b) $Re=80$ , (c) $Re=100$ , (d) $Re=200$ , (e) $Re=300$ , (f) $Re=400$ , (g) $Re=500$ , (h) $Re=600$ , (i) $Re=700$ .



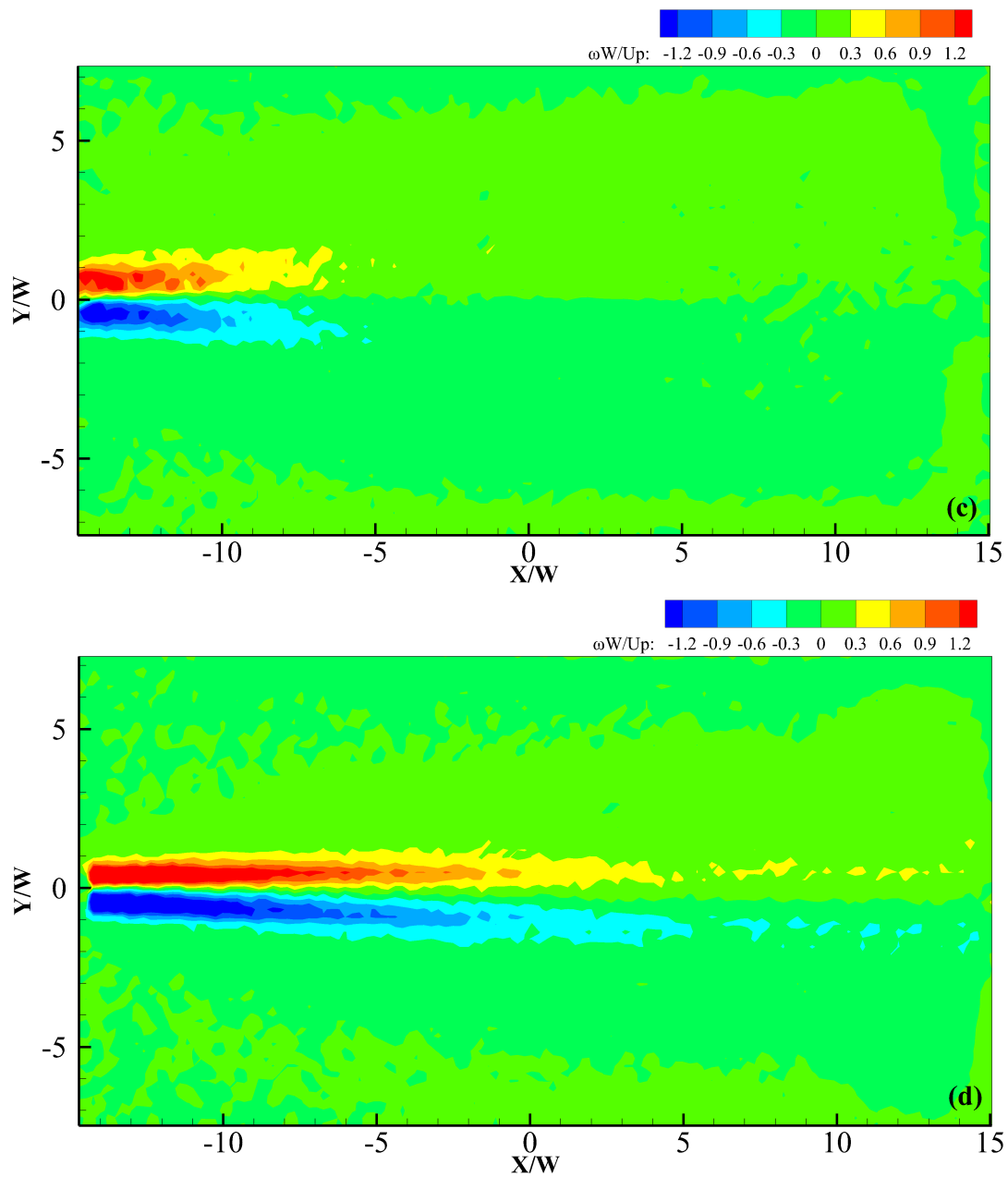


Figure 4.5. Continued.

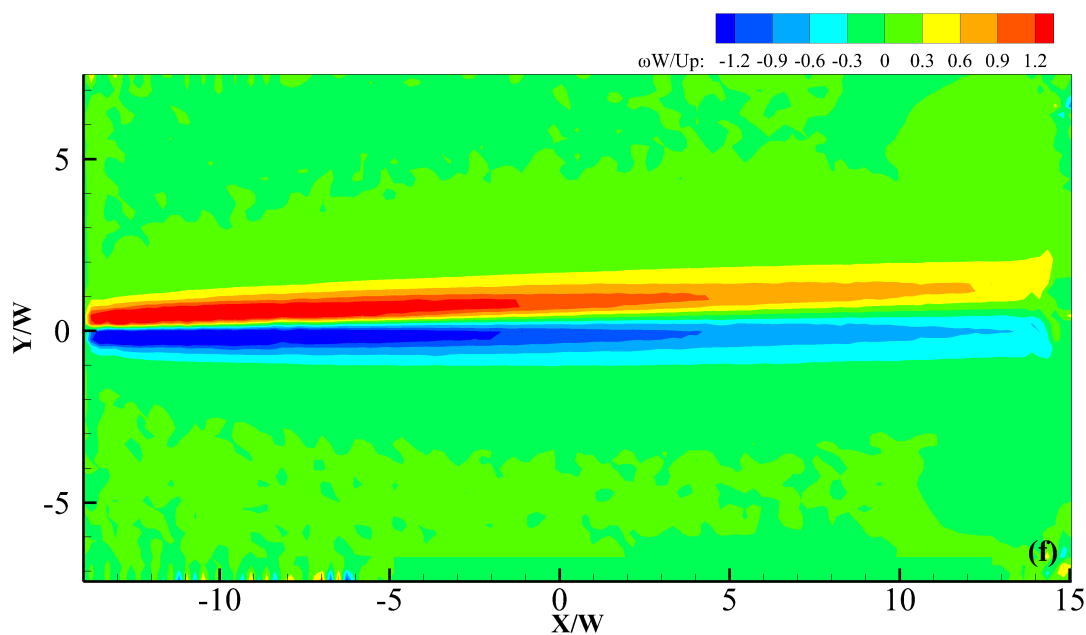
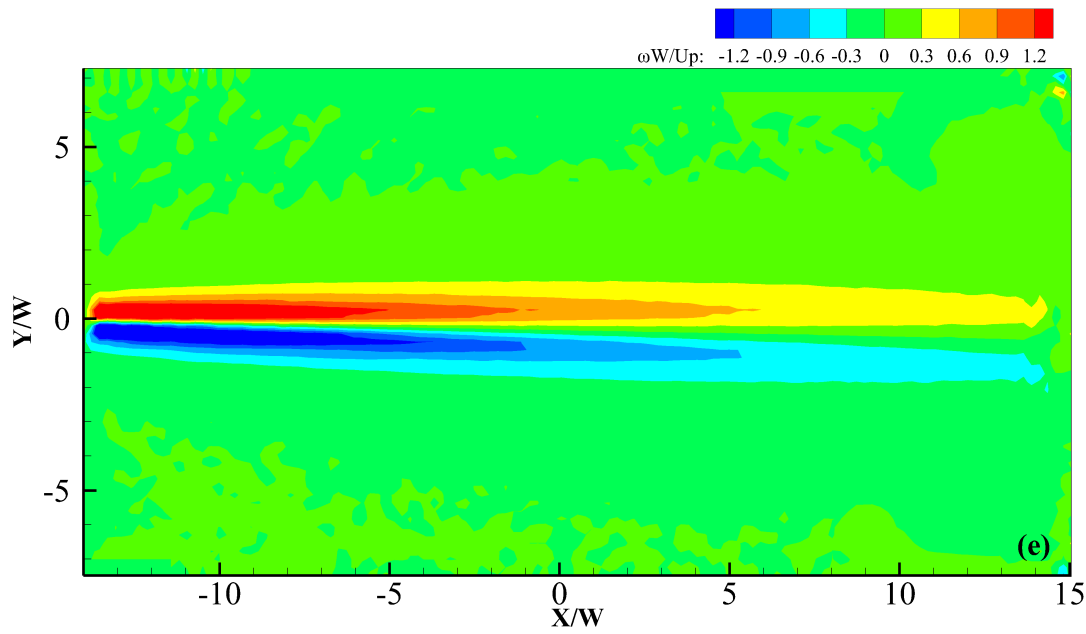


Figure 4.5.Continued.

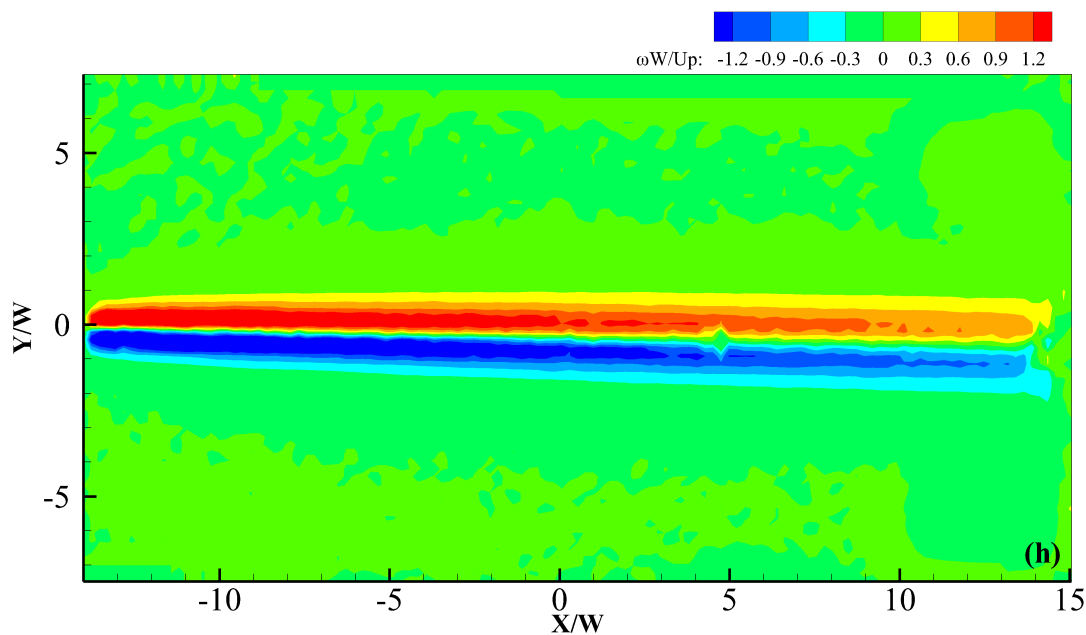
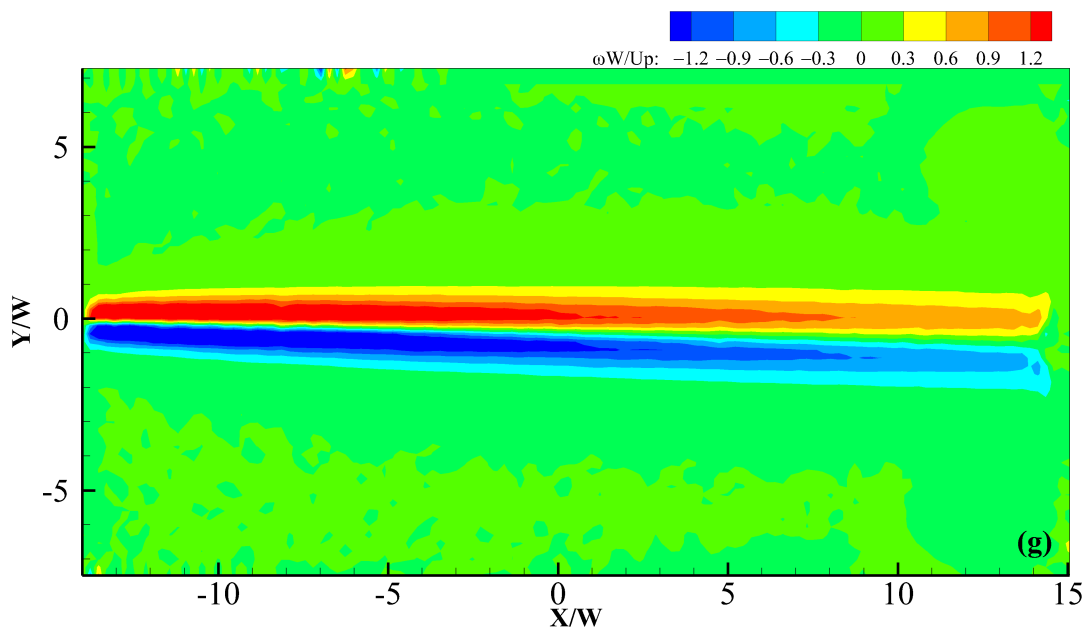


Figure 4.5.Continued.

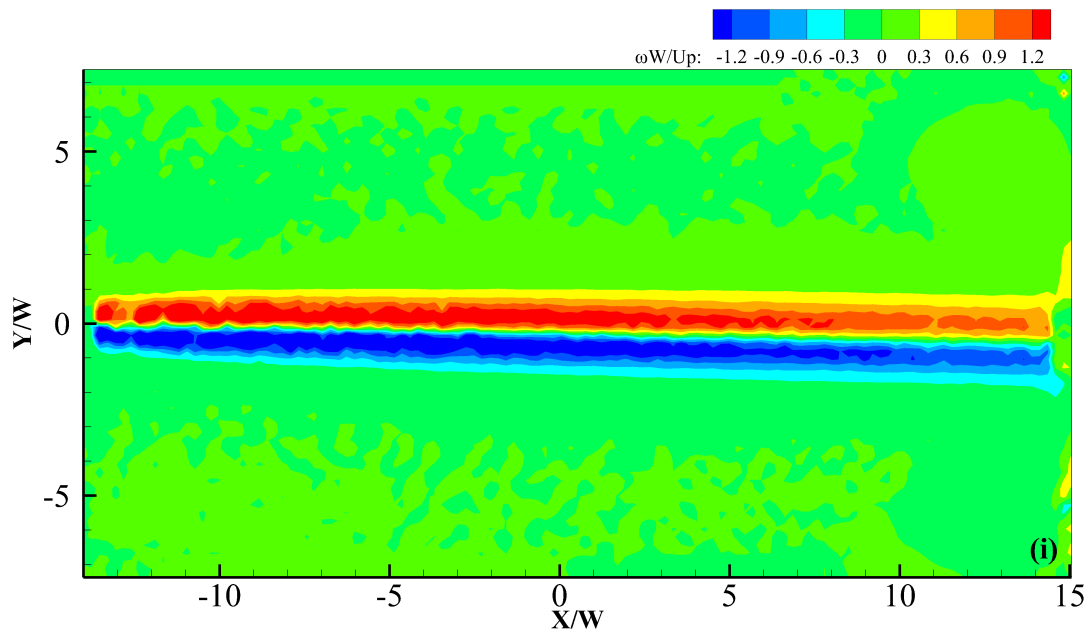


Figure 4.5.Continued.

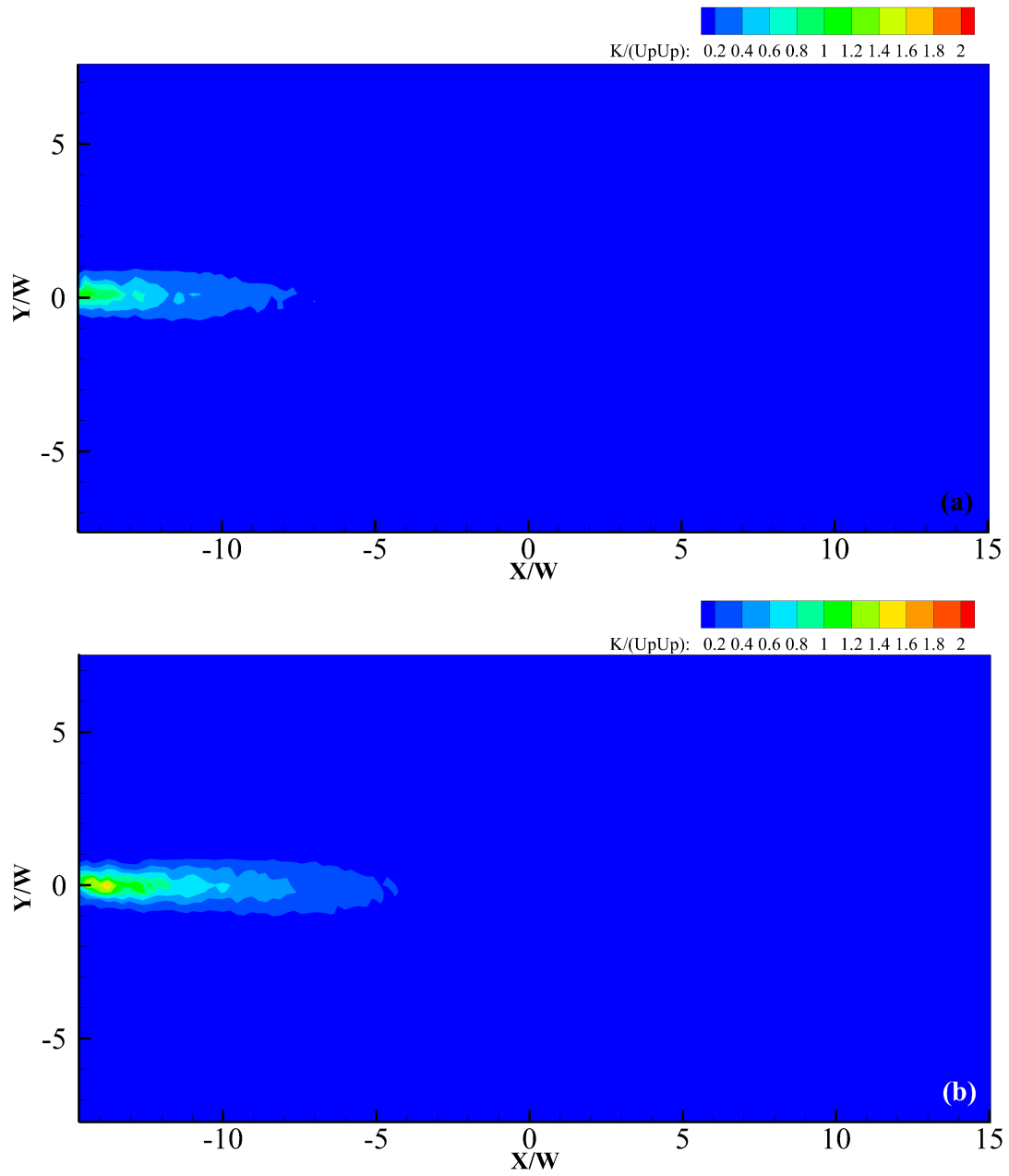


Figure 4.6. Kinetic energy fields for different Reynolds numbers, (a)  $Re=60$ , (b)  $Re=80$ , (c)  $Re=100$ , (d)  $Re=200$ , (e)  $Re=300$ , (f)  $Re=400$ , (g)  $Re=500$ , (h)  $Re=600$ , (i)  $Re=700$ .

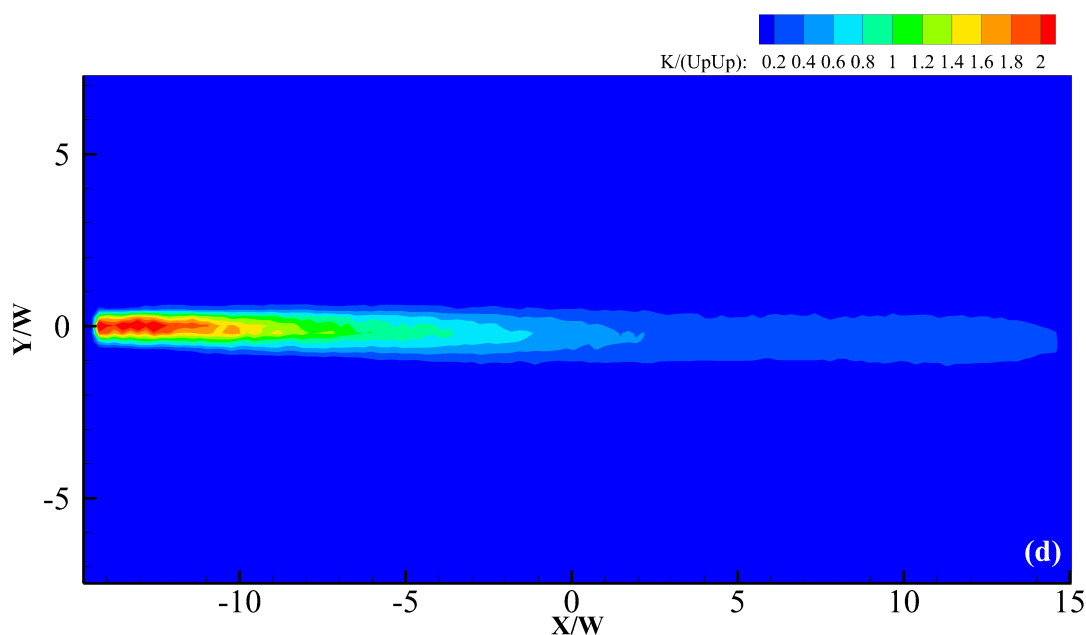
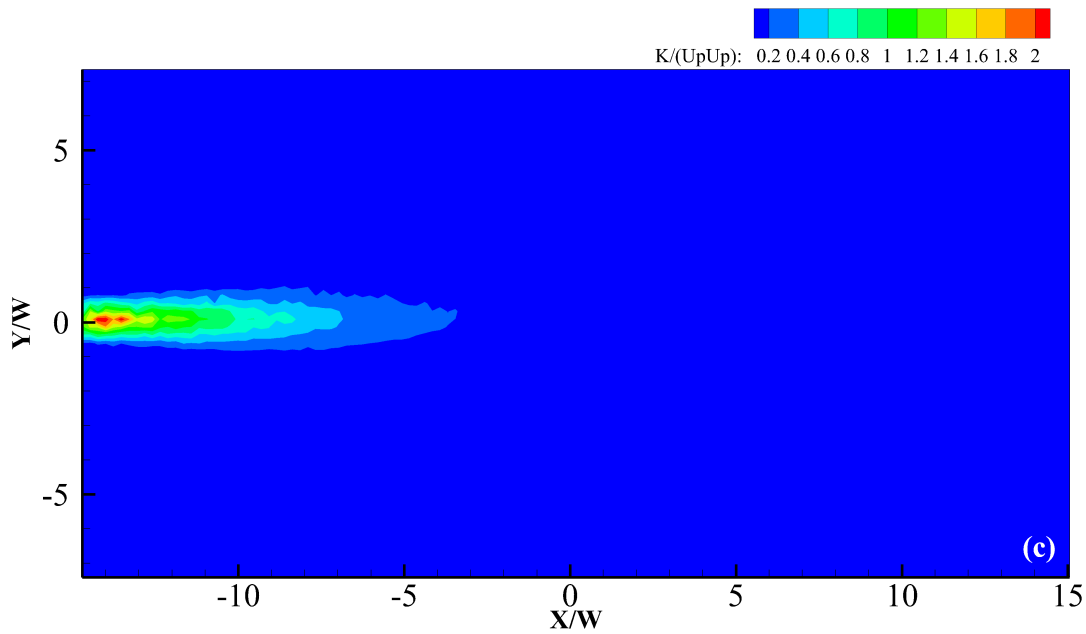


Figure 4.6.Continued.

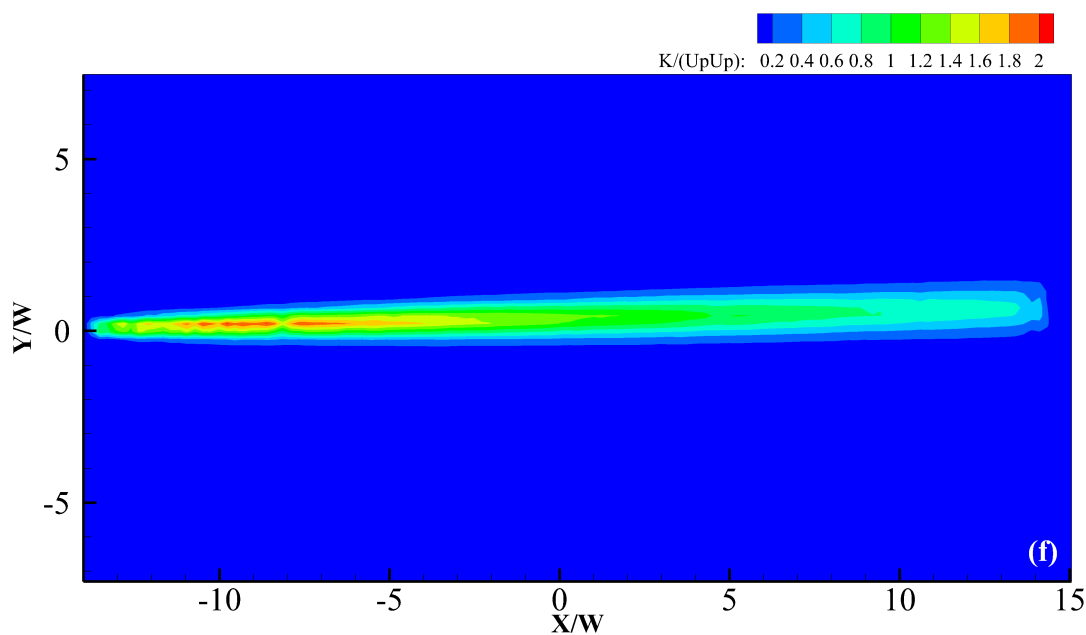
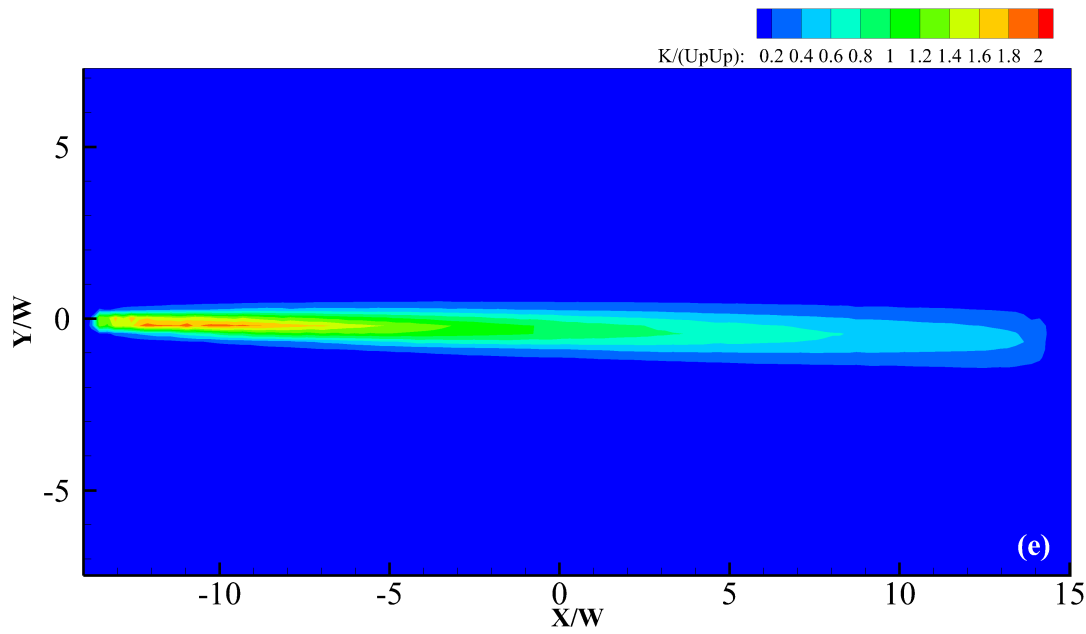


Figure 4.6.Continued.

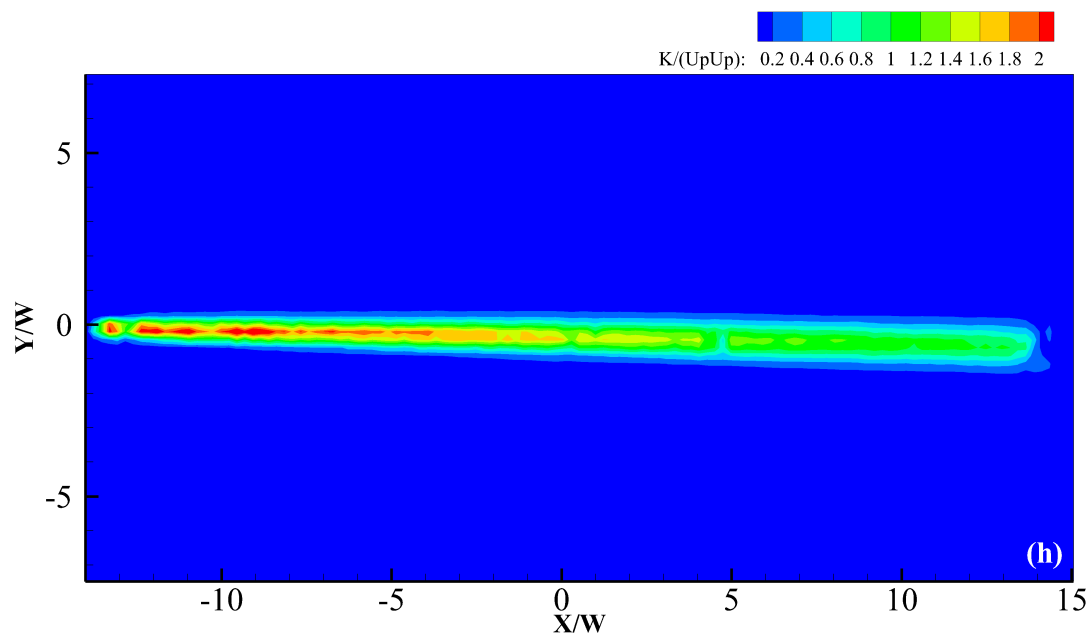
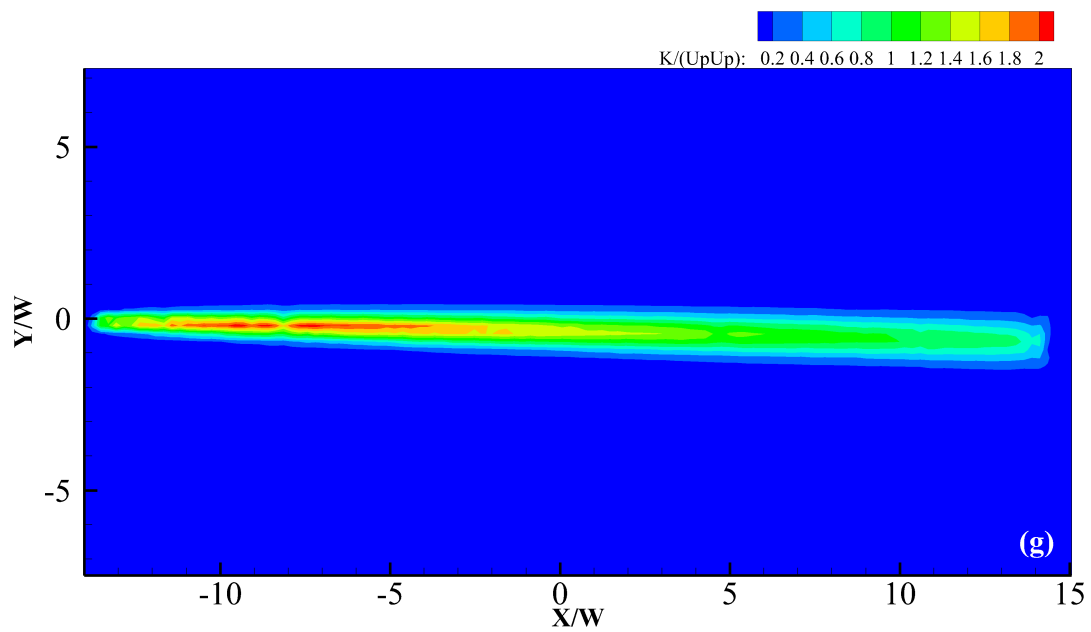


Figure 4.6.Continued.



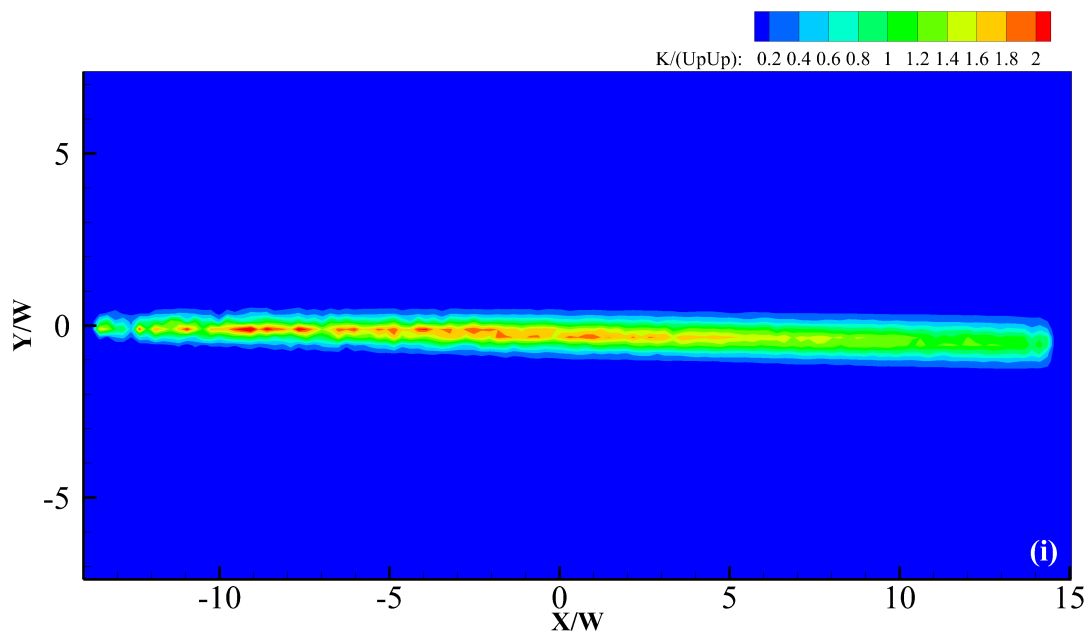


Figure 4.6.Continued.

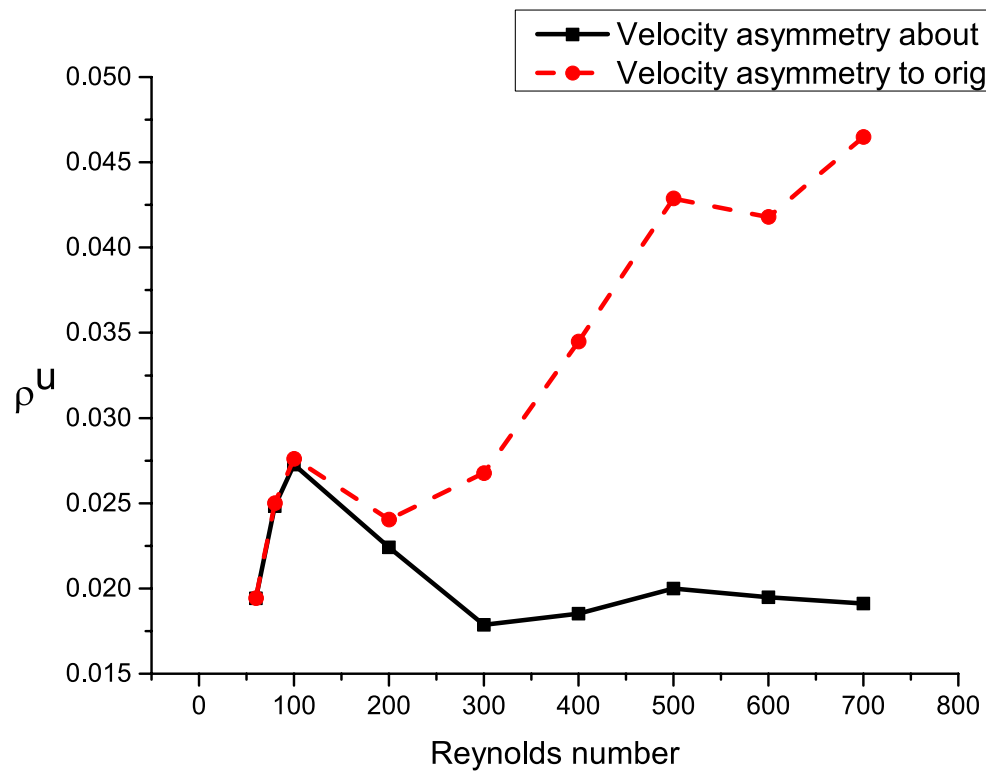


Figure 4.7. Velocity asymmetry at different Reynolds number.

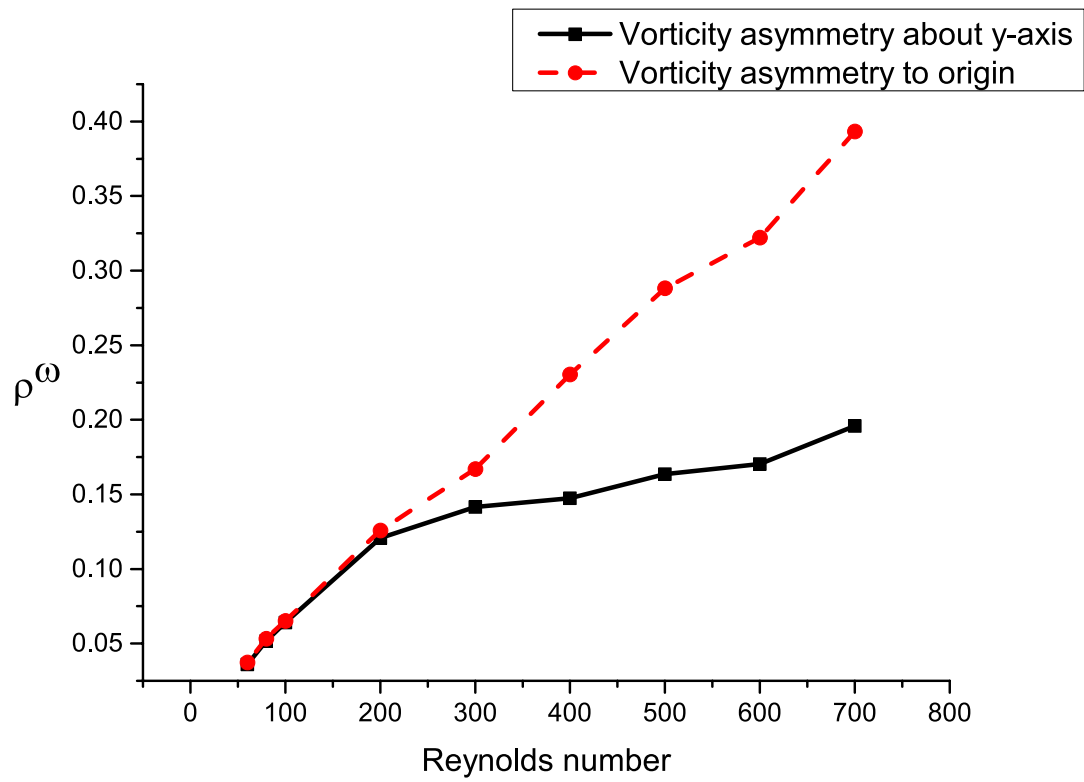


Figure 4.8. Vorticity asymmetry at different Reynolds number.

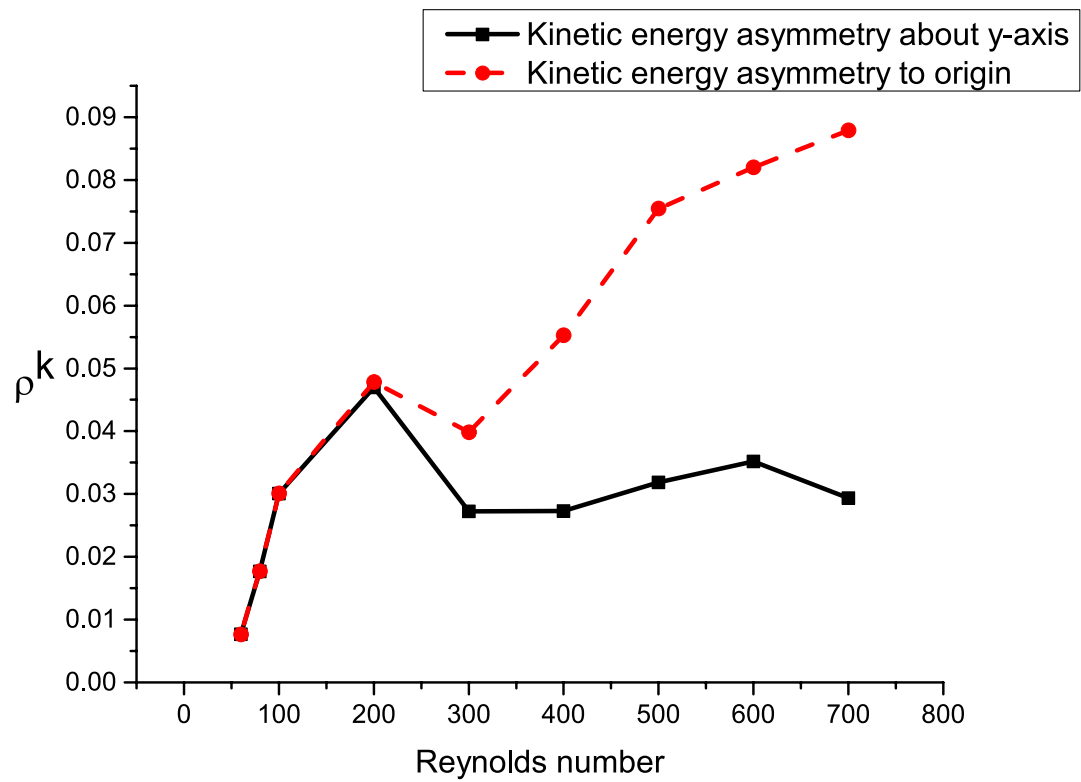


Figure 4.9. Kinetic energy asymmetry at different Reynolds number.

## 5. $\mathcal{PT}$ -SYMMETRIC FLOW FIELD WITH MAIN FLOW

To further explore the features of  $\mathcal{PT}$ -symmetric flow field. Another test section, shown in Figure 2.1 (b) and Figure 2.2 (b), is set up to retrieve the flow field. In this test section, a pair of perturbation inflow/outflow is introduced as main flow. Theoretically  $\mathcal{PT}$ -symmetric flow field will not be influenced by a symmetric main flow.

### 5.1 Experimental Condition

The experiment is similar to the one mentioned in chapter 4. The geometry of the test section is the same as the previous one the is listed in Table 2.1. In this experiment three syringe pumps are used to control the boundary condition of the flow field. The volumetric flow rate at the inlet and outlet marked as 1, 2 and 3 in Figure 2.2 is controlled using syringe pumps and by the incompressible assumption we will have the flow rate at 4 fixed. The newly added inlet/outlet tubings 3/4 have the same cross section dimension as the original ones, their length is 70mm each. Inlet/outlet 1/2 is the symmetric flow same as previous experiment and they are controlled using Dual NE-1000 syringe pump. The boundary condition at inlet 3 is controlled using another NE-1000 syringe pump. The boundary conditions for each inlet and outlet are shown in Table 5.1. In table 5.1 we use Reynolds number to represent volumetric flow rate and positive values represent inflow while negative values represent outflow. Inlet/outlet-3/4 is set up as main flow and for each main flow we change the volumetric flow rates of symmetric inlet/outlet-1/2. 4 sets of main flow is introduced including  $Re=60$ ,  $Re=100$ ,  $Re=300$  and  $Re=500$ . The Reynolds number for symmetric flow is also 60, 100, 300 and 500. Therefore we will have 16 flow fields in total. Plus, we retrieve the main flow fields individually by closing

inlet/outlet-1/2 for different Reynolds number. There are two snapshots in Figure 5.1, one is the individually main flow at Reynolds number 500, the other is the symmetric flow at Reynolds number 300 combined with main flow at Reynolds number 500.

## 5.2 Formalism

Like in the previous experiment, the dimensionless  $\mathcal{PT}$  asymmetries of velocity, vorticity, and kinetic energy at different Reynolds number are calculated based on the velocity field. The definition for  $\rho_1$  and  $\rho_2$  is the same as mentioned in the previous chapter. In this experiment, one cannot calculate the asymmetry solely using any of the velocity field. First of all, the main velocity field is subtracted from the combined situation by using

$$u_x = u_x^{combined} - u_x^{main}, \quad (5.1)$$

and

$$u_y = u_y^{combined} - u_y^{main} \quad (5.2)$$

where  $u_x^{combined}$  and  $u_y^{combined}$  are the x, y velocity components for the combined situation and  $u_x^{main}$  and  $u_y^{main}$  are the x, y velocity components for the main flow respectively, then the same procedure is followed for  $u_x$  and  $u_y$  using equation (4.16) and (4.19).

For kinetic energy fields, we first calculate the kinetic energy fields separately for main flow and for combined flow using

$$K_{combined}(x, y) = 0.5\rho[(u_x^{combined})^2 + (u_y^{combined})^2], \quad (5.3)$$

and

$$K_{main}(x, y) = 0.5\rho[(u_x^{main})^2 + (u_y^{main})^2] \quad (5.4)$$

then we subtract the kinetic energy field of main flow from the combined flow using

$$K(x, y) = K_{combined}(x, y) - K_{main}(x, y). \quad (5.5)$$

Finally the kinetic energy asymmetry is retrieved by applying  $K(x,y)$  to equation (4.17) and (4.20).

For vorticity field, we first calculate the vorticity fields separately for main flow and for combined flow using

$$\boldsymbol{\omega}_{combined}(x, y) = \nabla \times \mathbf{u}_{combined}(\mathbf{r}), \quad (5.6)$$

and

$$\boldsymbol{\omega}_{main}(x, y) = \nabla \times \mathbf{u}_{main}(\mathbf{r}) \quad (5.7)$$

then we subtract the vorticity field of main flow from the combined flow using

$$\boldsymbol{\omega}(x, y) = \boldsymbol{\omega}_{combined}(x, y) - \boldsymbol{\omega}_{main}(x, y). \quad (5.8)$$

Finally the vorticity asymmetry is retrieved by applying  $\boldsymbol{\omega}(x, y)$  to equation (4.18) and (4.21). Here  $\boldsymbol{\omega}(x, y)$  is in z direction only, therefore we can treat it as a scalar.

### 5.3 Results

An example of the asymmetry calculation is shown in Figure 5.2-Figure 5.4. In Figure 5.2 the velocity field, vorticity field and kinetic energy field of the main flow at Reynolds number 500 are plotted using *Tecplot*.  $U_p$  used for normalization is the averaged velocity at Reynolds number 500. In Figure 5.3 the velocity fields, vorticity field and kinetic energy field of the combined flow with main flow (Re=500) are plotted, the Reynolds number of symmetric inflow and outflow is 300.  $U_p$  used for normalization is the averaged velocity at Reynolds number 500. In Figure 5.3, the velocity field, vorticity field and kinetic energy field of the subtracted field are plotted.  $U_p$  used for normalization is the averaged velocity at Reynolds number 500. It could be observed that the contour for the subtracted flow field is similar to the original one (combined one). The flow field shown in Figure 5.4 is one of the subtracted flow

field and there are 15 else used to calculate the asymmetries. The asymmetries are shown in Figure 5.5-Figure 5.7.

#### 5.4 Discussion

From Figure 5.5-5.7 we can observe that the trend for each plot is similar. There are four lines in each figure and each line represents a different main flow, the x-axis is the Reynolds number of symmetric inlet/outlet flow while the y-axis stands for the dimensionless asymmetry number. Clearly for each main flow the asymmetry decrease as the flow rate of symmetric inlet/outlet flow goes up and the larger the Reynolds number of main flow will be the faster the rate of decreasing at the beginning. Moreover, for a fixed symmetric inlet/outlet flow, the larger Reynolds number of main flow will lead to a larger asymmetry of flow field. This phenomenon is more salient when the Reynolds number of symmetric flow is smaller. When the Reynolds number of symmetric flow goes up to 500, there is only a slight difference between the asymmetry for different main flow.

Therefore, exponential fitting is used to explore the relationship between asymmetries and Reynolds number. The curves plotted are the exponential fitted curve, the model used is

$$\rho = A_1 \times \exp(-Re/t_1) + \rho_0 \quad (5.9)$$

where  $A_1$ ,  $t_1$  and  $\rho_0$  are the constants for each model that need to be determined. From the plotted result, most of the points locate precisely on the fitting curve which indicates there is a strong exponential relationship between the asymmetries and Reynolds number in this experiment.  $A_1$ ,  $t_1$  and  $\rho_0$  for each fitting curve are shown in Table 5.2-Table 5.7.



Table 5.1. Boundary condition for  $\mathcal{PT}$ -symmetric flow field with main flow.

<b>1-inlet</b>	<b>2-outlet</b>	<b>3-inlet</b>	<b>4-outlet</b>
60	-60	60	-60
60	-60	100	-100
60	-60	300	-300
60	-60	500	-500
100	-100	60	-60
100	-100	100	-100
100	-100	300	-300
100	-100	500	-500
300	-300	60	-60
300	-300	100	-100
300	-300	300	-300
300	-300	500	-500
500	-500	60	-60
500	-500	100	-100
500	-500	300	-300
500	-500	500	-500
0	0	60	-60
0	0	100	-100
0	0	300	-300
0	0	500	-500

Table 5.2. Fitting constant for velocity asymmetry about y-axis.

Mainflow (Re)	$\rho_0$	$A_1$	$t_1$
60	0.02092	2.704	13.54
100	0.02041	1.282	26.02
300	0.05961	24.871	23.40
500	0.14001	41.022	26.63

Table 5.3. Fitting constant for velocity asymmetry to origin.

Mainflow (Re)	$\rho_0$	$A_1$	$t_1$
60	0.02135	0.254	29.26
100	0.02732	2.787	20.35
300	0.07273	27.237	22.58
500	0.14429	40.209	26.73

Table 5.4. Fitting constant for vorticity asymmetry about y-axis.

Mainflow (Re)	$\rho_0$	$A_1$	$t_1$
60	0.14901	3.298	46.48
100	0.2166	6.339	31.84
300	0.61482	100.247	36.09
500	1.48407	455.466	33.27

Table 5.5. Fitting constant for vorticity asymmetry to origin.

Mainflow (Re)	$\rho_0$	$A_1$	$t_1$
60	0.17863	5.538	36.63
100	0.25985	7.927	30.15
300	0.62644	81.752	40.99
500	1.50984	474.853	33.99

Table 5.6. Fitting constant for kinetic energy asymmetry about y-axis.

Mainflow (Re)	$\rho_0$	$A_1$	$t_1$
60	0.02736	110760.9	4.10
100	0.02536	33955.1	5.33
300	0.06038	2230.6	16.28
500	0.34800	27747.2	15.27

Table 5.7. Fitting constant for kinetic energy asymmetry to origin.

Mainflow (Re)	$\rho_0$	$A_1$	$t_1$
60	0.02731	103275.2	4.12
100	0.02717	40005.7	5.25
300	0.06026	2238.5	16.27
500	0.34584	27680.2	15.27

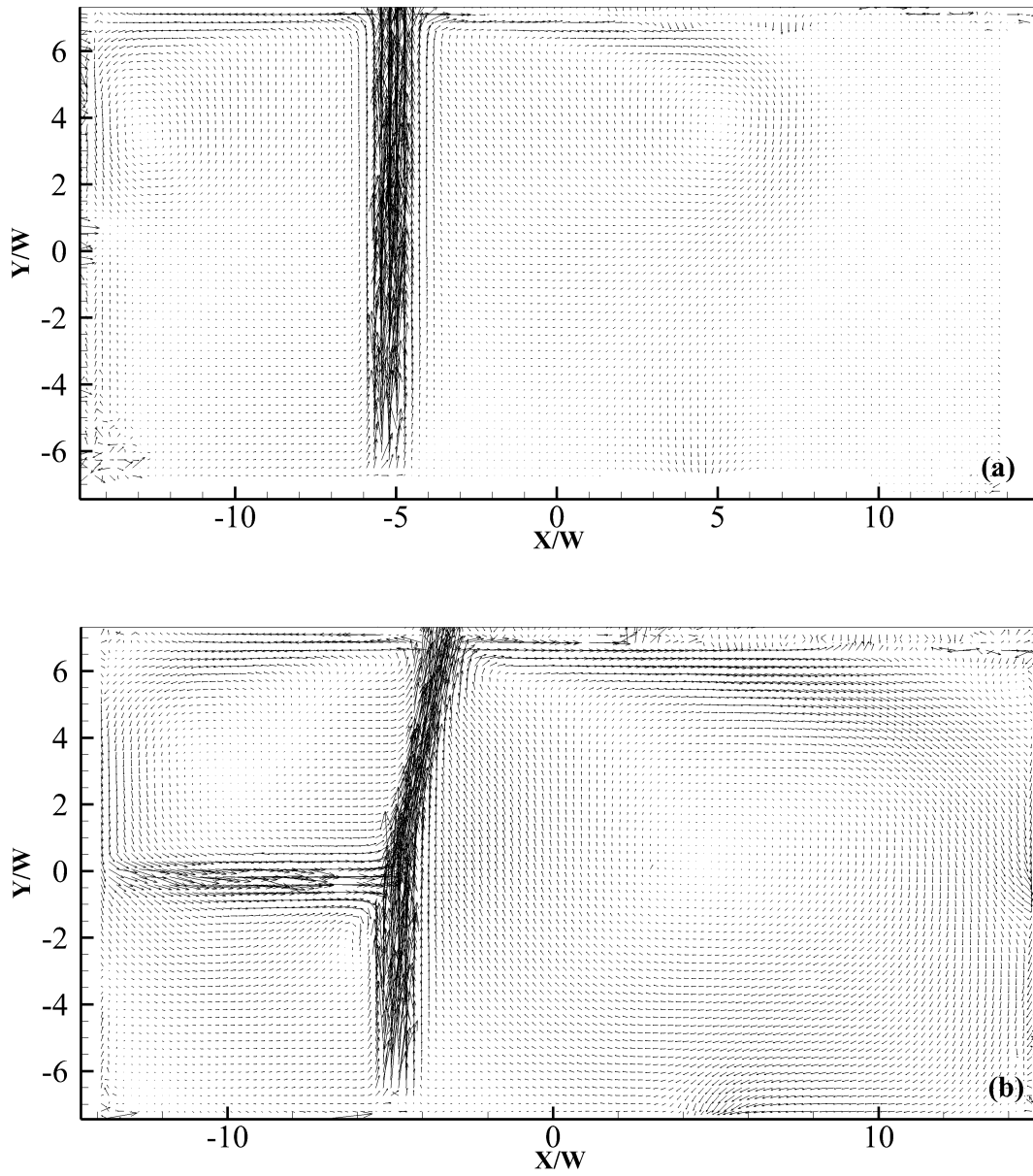


Figure 5.1. Snapshots for velocity field with main flow, (a) Main flow individually  $Re=500$ , (b) Symmetric flow  $Re=300$  combined with main flow  $Re=500$ .

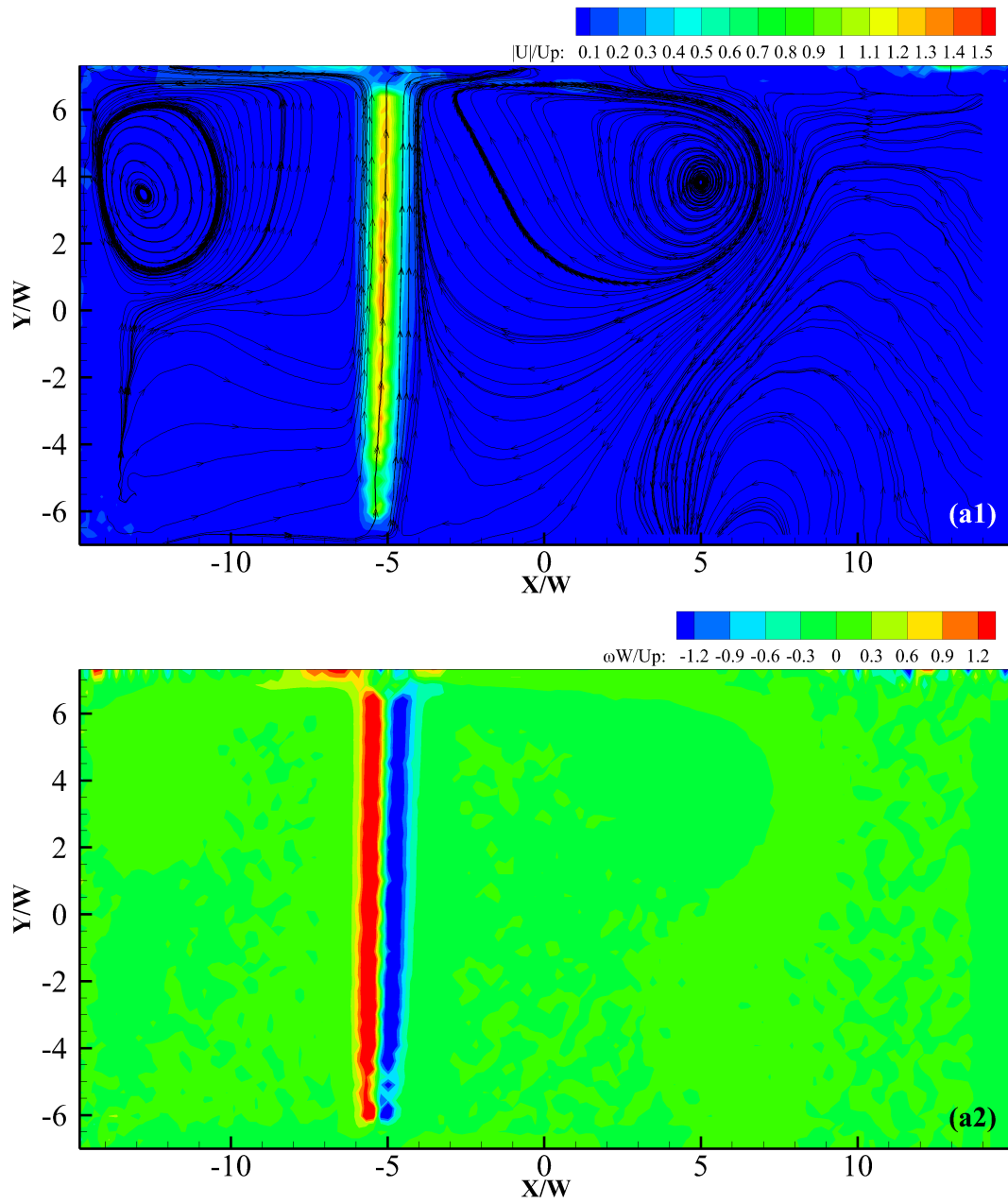


Figure 5.2. Velocity field, vorticity field and kinetic energy field of main flow at Reynolds number 500, (a1)Velocity field, (a2)Vorticity field, (a3)Kinetic energy field.

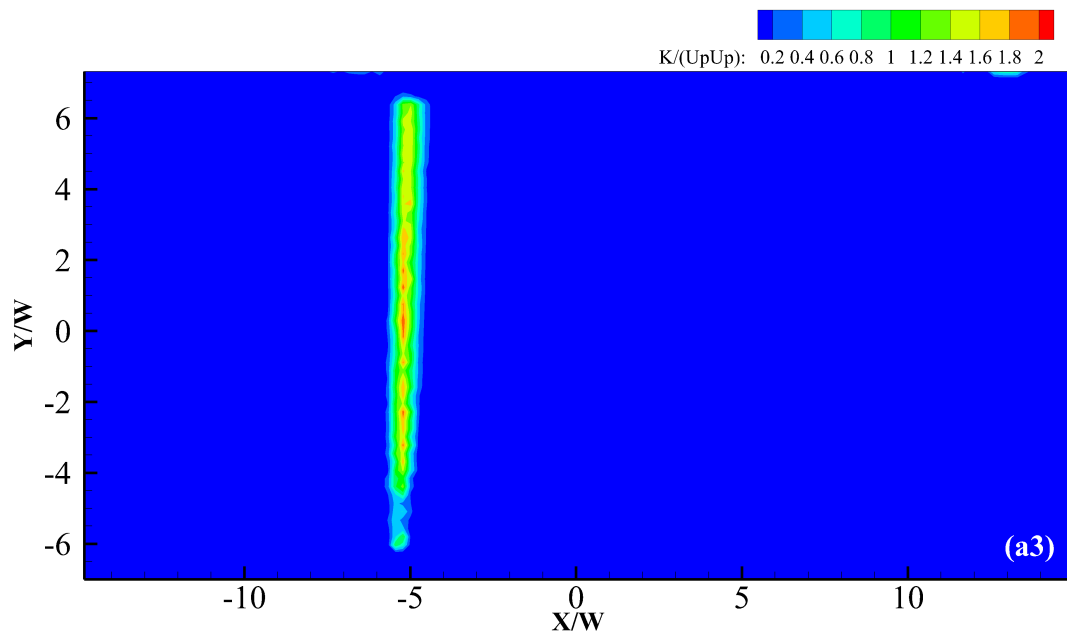


Figure 5.2.Continued.

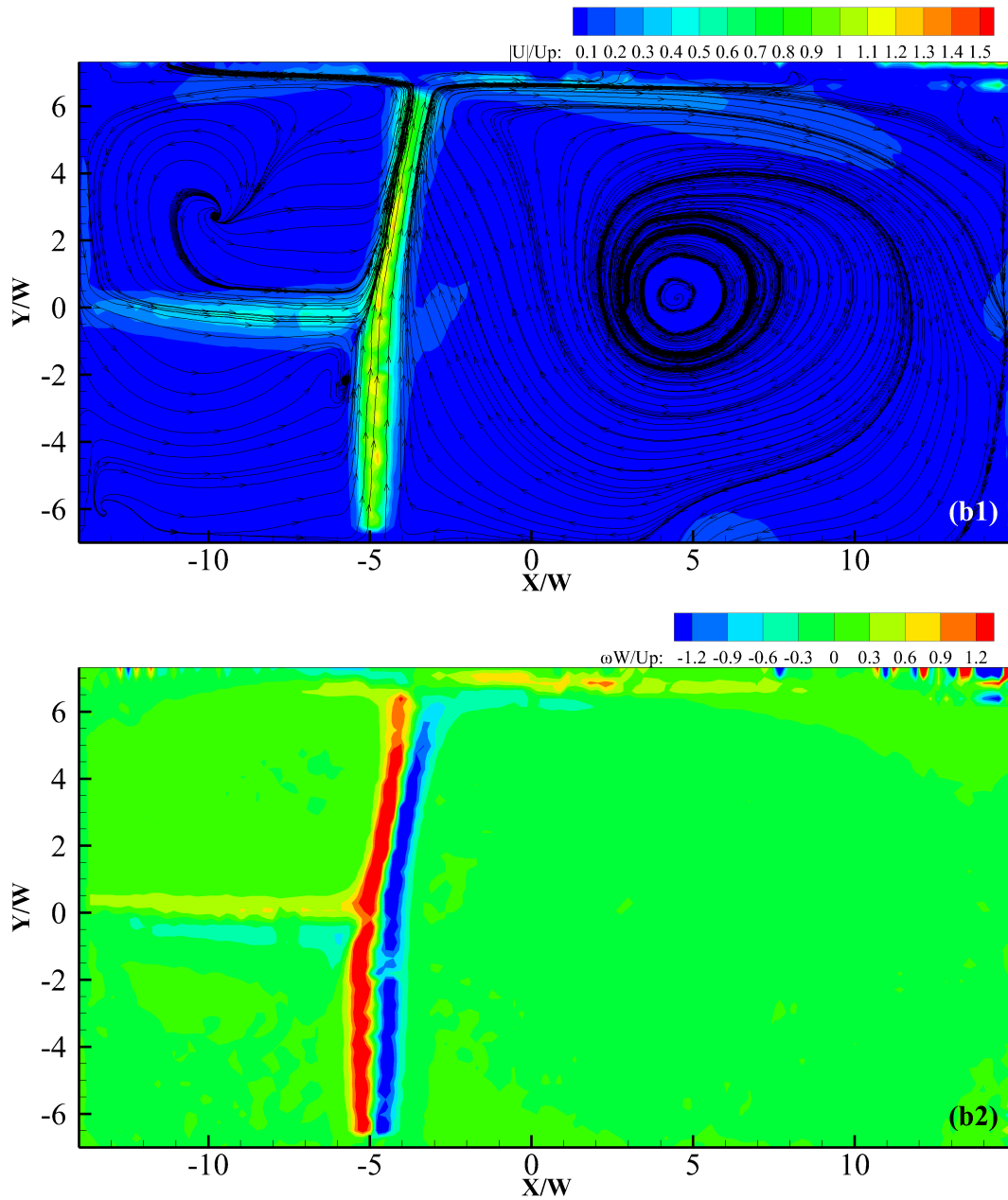


Figure 5.3. Velocity field, vorticity field and kinetic energy field of combined flow, main flow  $Re=500$ , symmetric inflow and outflow  $Re=300$ , (b1)Velocity field, (b2)Vorticity field, (b3)Kinetic energy field.

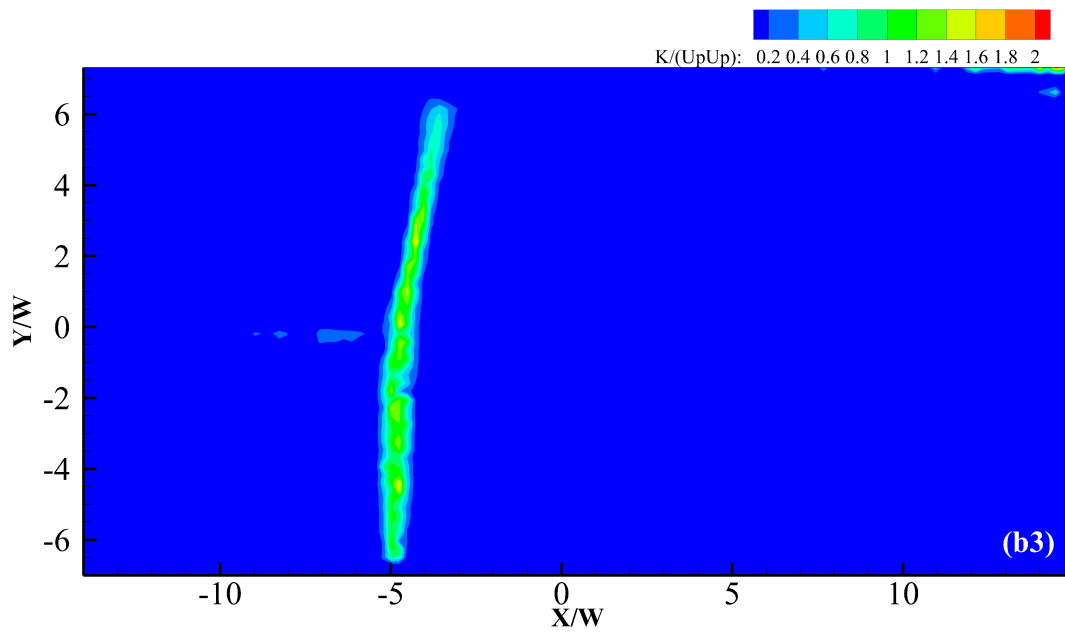


Figure 5.3.Continued.



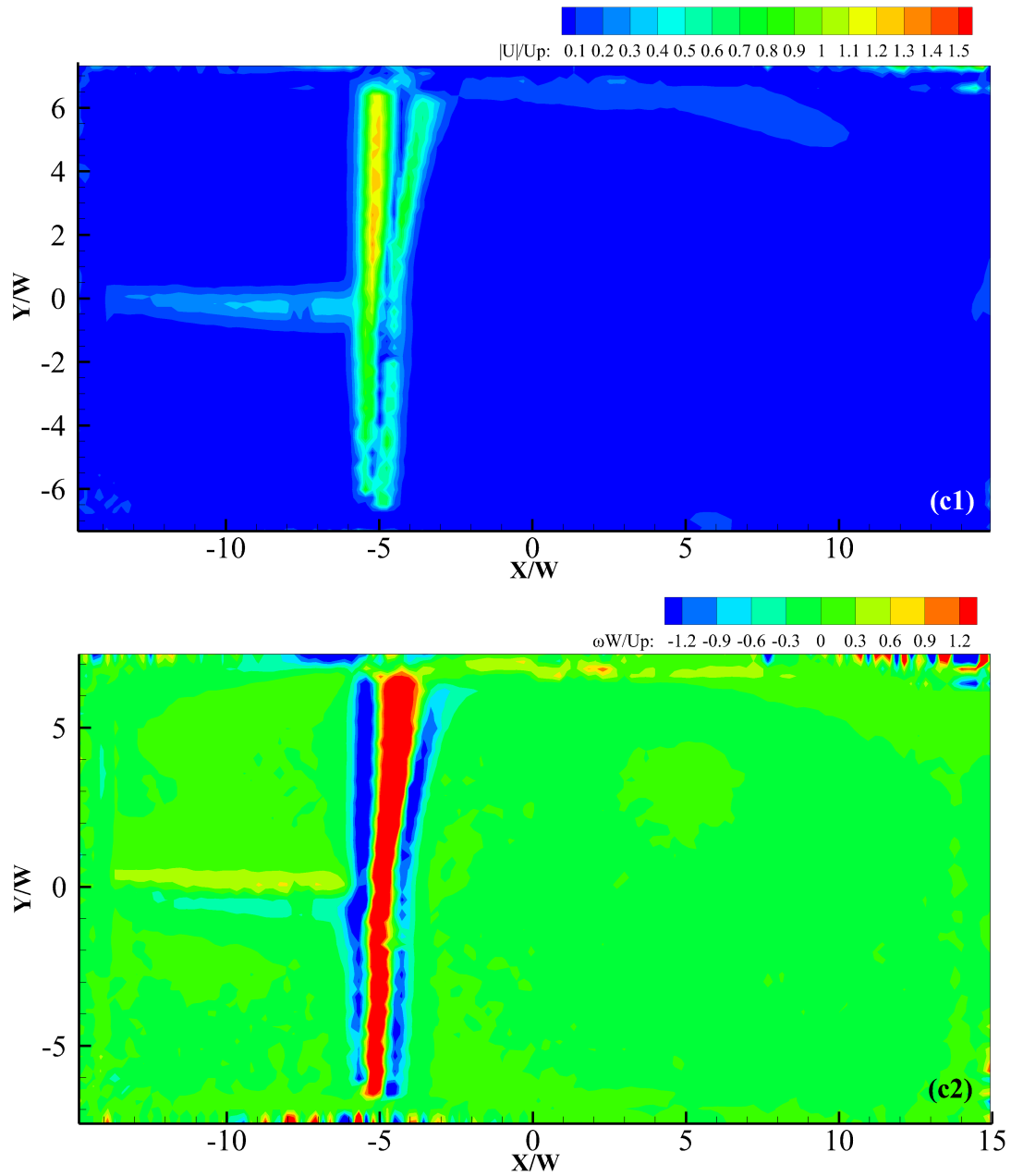


Figure 5.4. Velocity field, vorticity field and kinetic energy field subtracted flow, (c1)Velocity field, (c2)Vorticity field, (c3)Kinetic energy field.

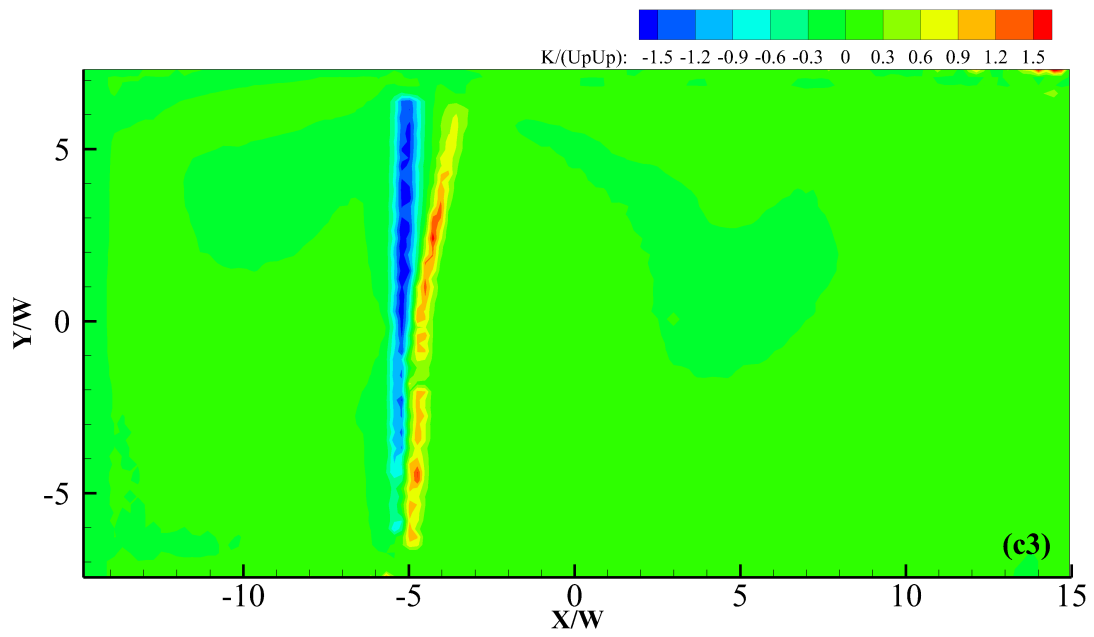


Figure 5.4.Continued.

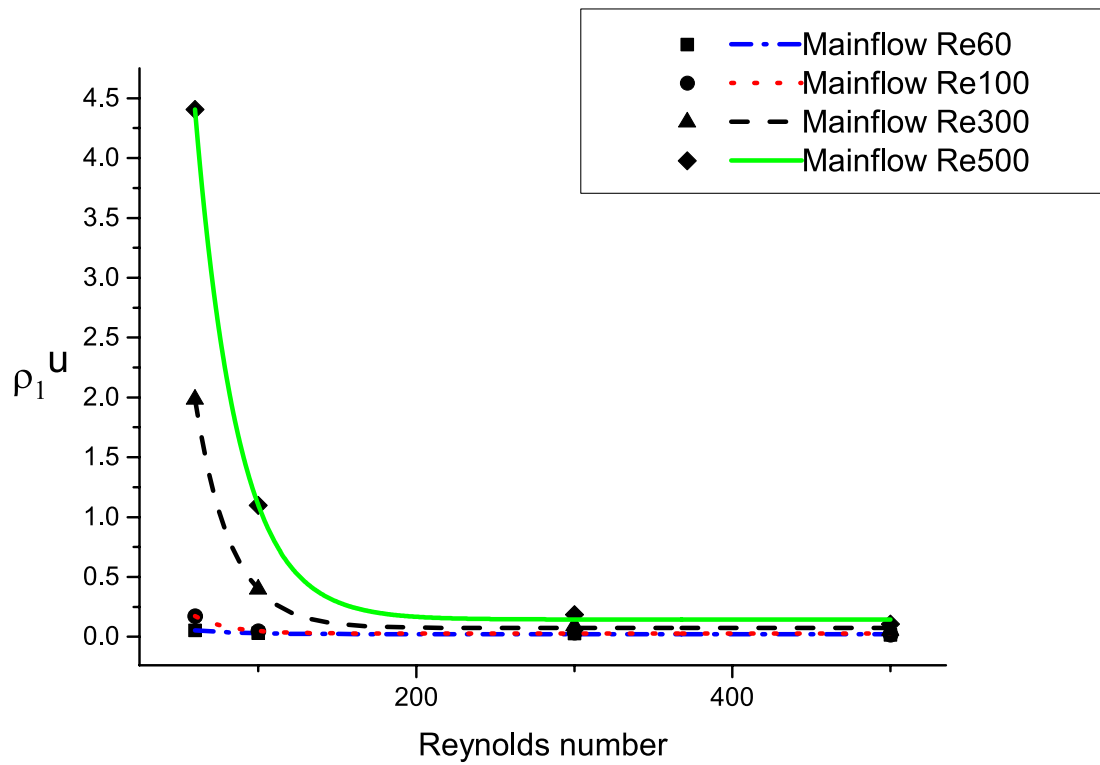


Figure 5.5. Velocity asymmetry for  $\mathcal{PT}$ -symmetric flow field with main flow.

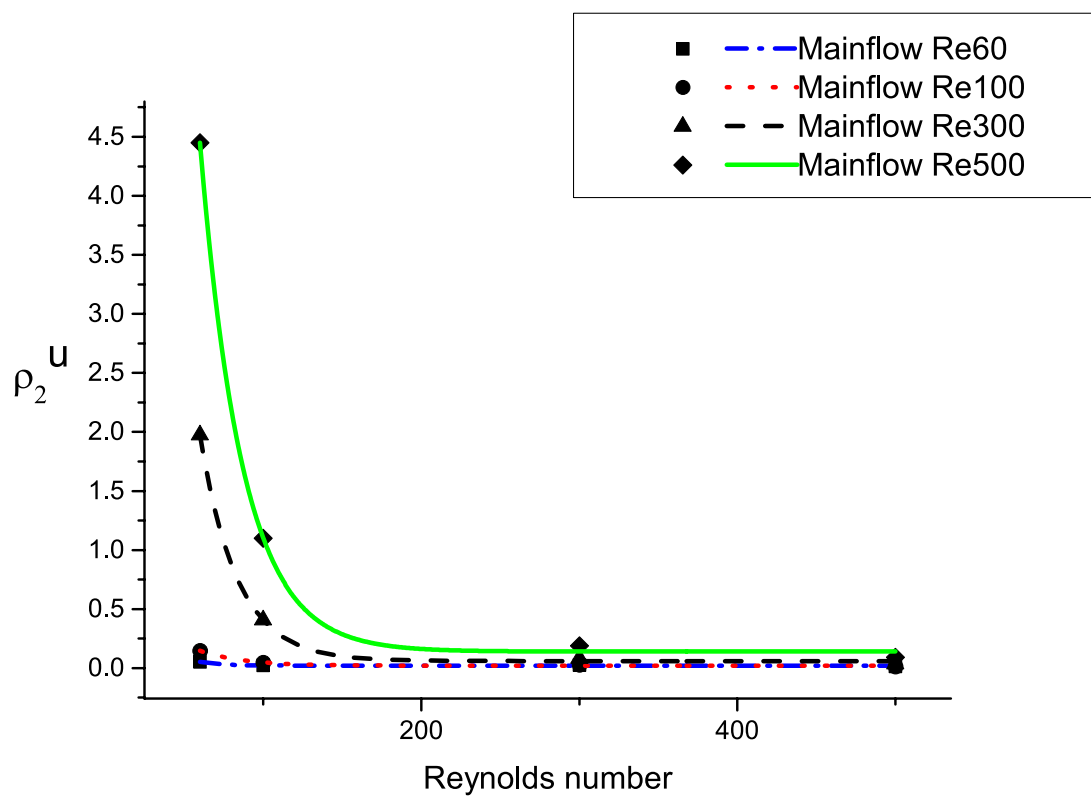


Figure 5.5.Continued.

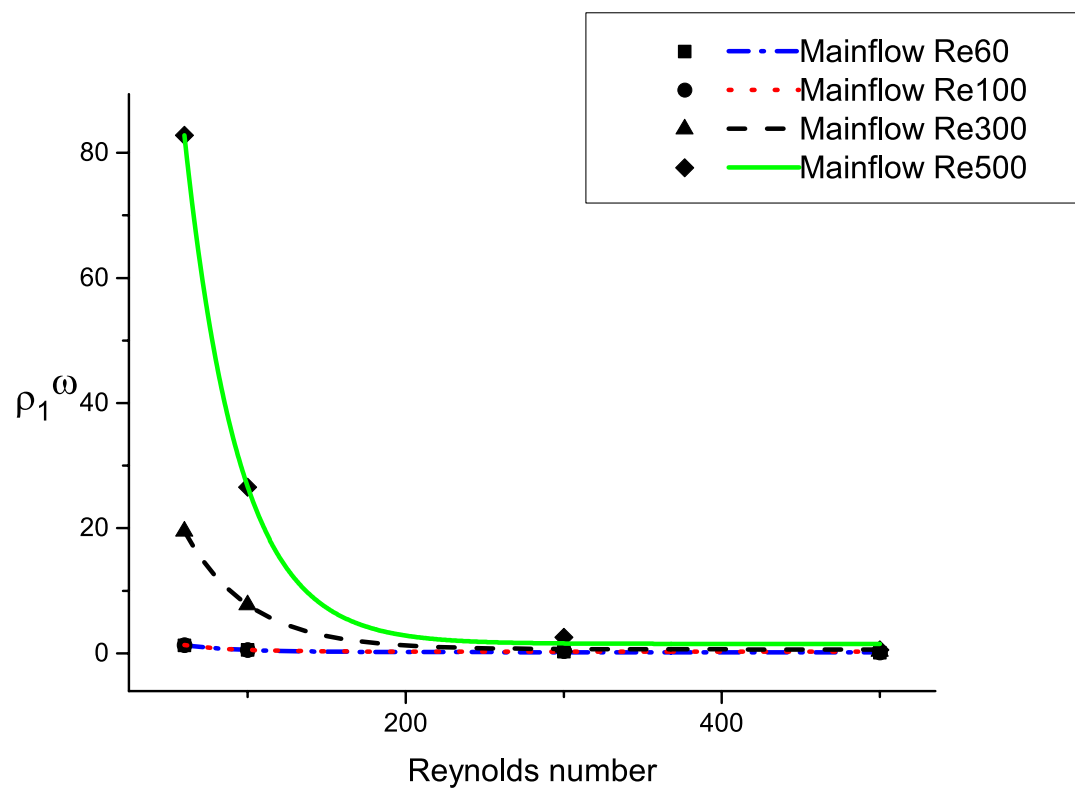


Figure 5.6. Vorticity asymmetry for  $\mathcal{PT}$ -symmetric flow field with main flow.

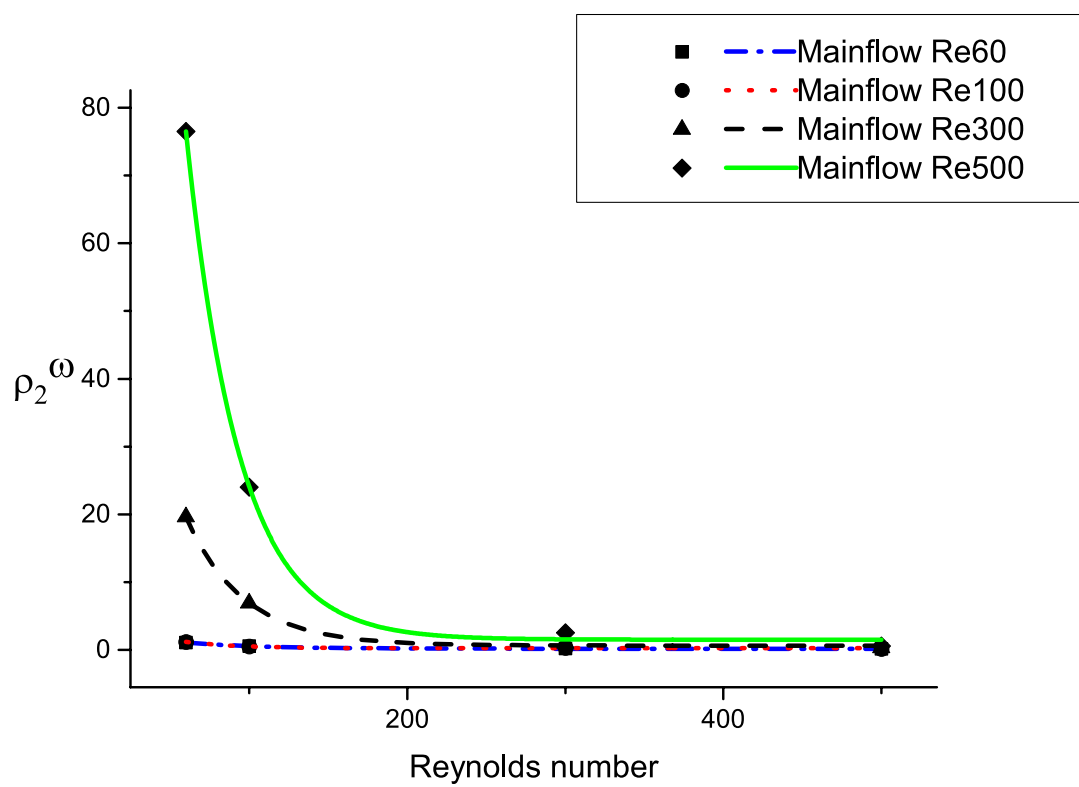


Figure 5.6.Continued.

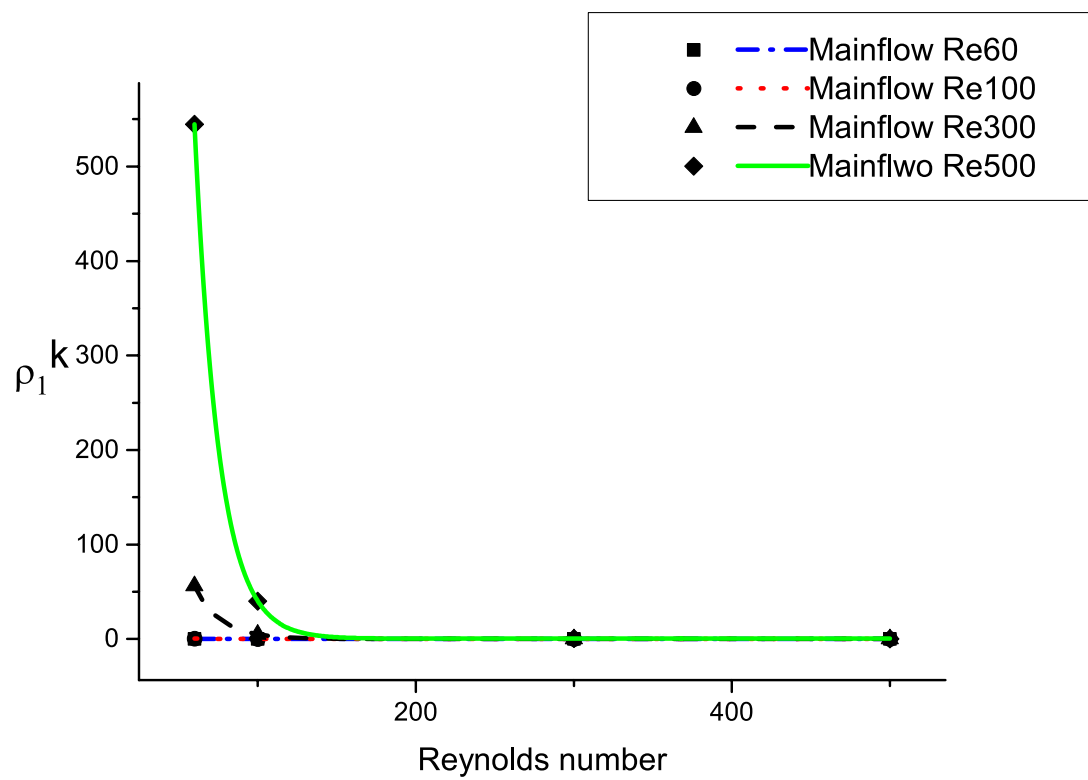


Figure 5.7. Kinetic energy asymmetry for  $\mathcal{PT}$ -symmetric flow field with main flow.

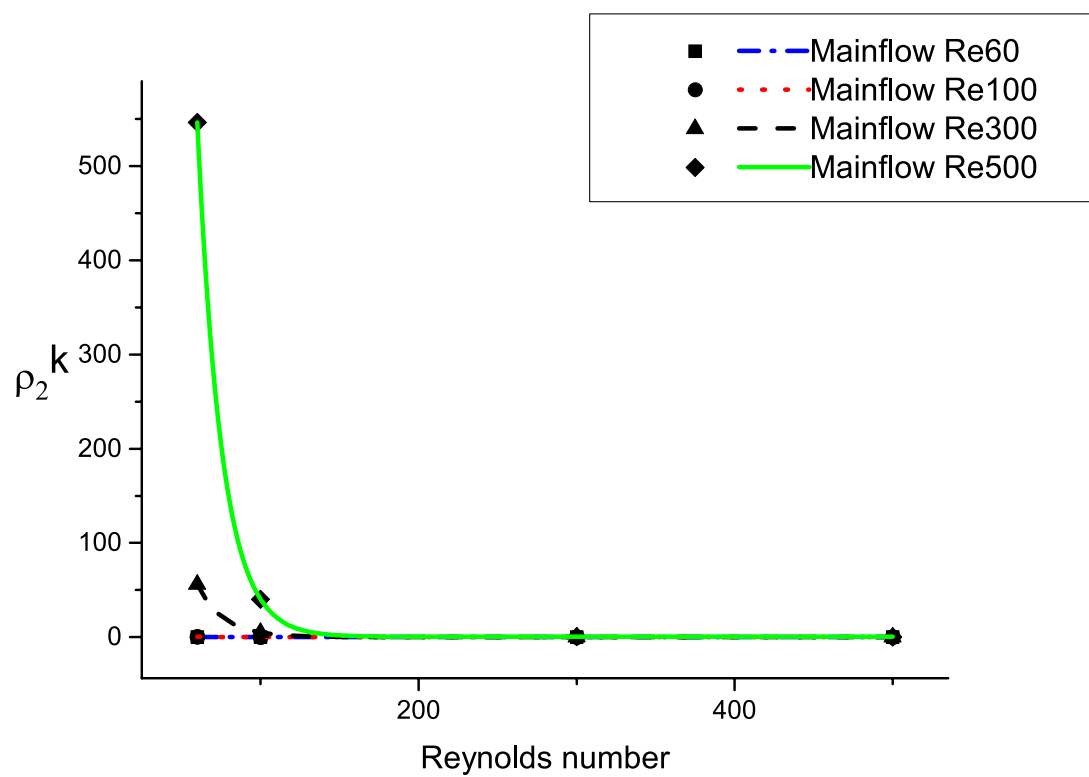


Figure 5.7.Continued.



## 6. SUMMARY AND CONCLUSIONS

In the present study, two separate experiments are performed to explore the asymmetries of velocity field, vorticity field and kinetic energy field with respect to Reynolds number. The first experiment is to explore the asymmetries of a flow field with balanced inflow and outflow (symmetric boundary condition) at different Reynolds number. Dimensionless asymmetry numbers are calculated and plotted with respect to Reynolds numbers. In the second experiment, a pair of perturbation inflow and outflow which is viewed as main flow is introduced to the original flow field (in the first experiment). The flow fields under combined boundary condition (main flow and symmetric inflow/outflow) and the main flow fields are retrieved using PIV. The main flow is then subtracted from the combined flow the asymmetries of the rest part are calculated and plotted with respect to Reynolds number.

### 6.1 Overview of Experiments and Discussion

In the first experiment, the flow fields are generated using a symmetric inflow and outflow at different Reynolds numbers. The velocity fields are retrieved using both continuous PIV system and pulsed PIV system. Vorticity fields and kinetic energy fields are calculated using velocity fields. Dimensionless asymmetry numbers ( $\rho_1$  and  $\rho_2$ ) are calculated receptively. The relationship between the asymmetry and Reynolds number dose not follow the linear relationship as the computational results predicted. There are three main factors that may lead to the result, one is the velocity field is three-dimensional instead of two-dimensional, however only a two-dimensional velocity field can be retrieved because of the experiment limitation. The computational results are either three-dimensional or two-dimensional, using asymmetry of two-dimensional velocity fields to describe the asymmetry of three-dimensional flow

field may introduce unexpected errors. The other is the velocity field in the aluminum tubing is not retrieved. The boundary conditions are strictly symmetric only when the velocity fields within the tubing are added. However, since the tubing is not transparent the velocity field cannot be retrieved using PIV. The missing velocity fields may bring errors to the asymmetry analysis. The last one is the computational result assumes the velocity profile for inflow and outflow are uniform which contradict the real scenario.

The second experiment is to explore the asymmetry of flow fields with main flow. The results show an exponential relationship between asymmetries and Reynolds numbers. Besides the factors that may bring errors to the results mentioned above. It may not be feasible to subtract the velocity vectors of main flow directly from the combined situation since the governing equation (Navier-Stokes equation) is not linear. In addition, since the inlet/outlet tubing 3/4 is short, the pipe flow within 3/4 is not fully developed when Reynolds number is large. The boundary condition for main flow is not symmetric as a result. This may bring errors to the asymmetry analysis.

## 6.2 Recommendation for Future Research

This study has largely turned a blind eye to  $\mathcal{PT}$  asymmetries in flow field with balance inflow and outflow using experimental method. Future analysis should settle the problems mentioned in the previous section. Test sections with different geometries should be build up for flow field generation. The ranges of Reynolds number should be expanded in future study.

## LIST OF REFERENCES

## LIST OF REFERENCES

- [1]Carl M. Bender, “Complex Extension of Quantum Mechanics,” *Physical Review Letters* 89:270401,2002
- [2]Carl M. Bender, Dorje C. Brody and Hugh F. Jones, “MUST A HAMILTONIAN BE HERMITIAN,” *American Journal of Physics* 71 (2003) 1095-1102
- [3]Carl M. Bender, Jun-Hua Chen, Daniel W. Darg, and Kimball A. Milton, “Classical Trajectories for Complex Hamiltonians,” *Journal of Physics A: Mathematical and General* 39, 4219-4238 (2006)
- [4]Carl M. Bender, “Introduction to  $\mathcal{PT}$ -Symmetric Quantum Theory,” *Contemporary Physics* 46:277-292,2005
- [5]Carl M. Bender, Stefan Boettcher, and Peter N. Meisinger, “ $\mathcal{PT}$  -Symmetric Quantum Mechanics,” *J.Math.Phys.* 40 (1999) 2201-2229
- [6]Miloslav Znojil, “What is  $\mathcal{PT}$  symmetry” *American Journal of Physics* March 20 2001
- [7]Carl M. Bender, Peter N. Meisinger, and Qinghai Wang, “All Hermitian Hamiltonians Have Parity,” *J. Phys. A: Math. Gen.* 36 1029
- [8]R. Resnick, R. Eisberg, John Wiley and Sons, “Quantum Physics of Atoms, Molecules, Solids, Nuclei and Particles (2nd Edition),” 1985
- [9]P.W. Atkins, “Quanta: A handbook of concepts,” Oxford University Press, 1974
- [10]I.S. Grant and W.R. Phillips, “Electromagnetism (2nd edition),” Manchester Physics Series, 2008
- [11]Arfken. G, “Hermitian (Self-Adjoint) Operators.” Chapter 9.2 in *Mathematical Methods for Physicists, 3rd ed.* Orlando, FL: Academic Press, pp. 504-506 and 510-516, 1985.
- [12]A. Guo and G. J. Salamo, “Observation of  $\mathcal{PT}$ -Symmetry Breaking in Complex Optical Potentials,” *Phys. Rev. Lett.* 103, 093902
- [13]Liang Feng, Maurice Ayache, Jingqing Huang, Ye-Long Xu, Ming-Hui Lu, Yan-Feng Chen, Yeshaiahu Fainman and Axel Scherer1, “Nonreciprocal Light Propagation in a Silicon Photonic Circuit,” *Science* 5 August 2011: Vol. 333 no. 6043 pp. 729-733
- [14]V. V. Konotop and D. A. Zezyulin, “Stochastic  $\mathcal{PT}$  -symmetric coupler,” *Optics Letters* 39, 1223-1226 (2014)
- [15]Joseph Schindler, Ang Li, Mei C. Zheng, F. M. Ellis and Tsampikos Kottos, “Experimental Study of Active LRC Circuits with  $\mathcal{PT}$  - Symmetries” *Phys. Rev. A* 84, 040101(R) (2011)
- [16]Carl M. Bender and Stefan Boettcher, “Real Spectra in Non-Hermitian Hamiltonians Having  $\mathcal{PT}$  Symmetry,” *Physical Review Letters* VOLUME 80, NUMBER 24

- [17]Christian E. Rter, Konstantinos G. Makris, Ramy El-Ganainy, Demetrios N. Christodoulides, Mordechai Segev and Detlef Kip, “Observation of paritytime symmetry in optics,” *Nature Physics* 6, 192 - 195 (2010)
- [18]Yogesh N. Joglekar, Clinton Thompson, Derek D. Scott and Gautam Vemuri, “Optical waveguide arrays: quantum elects and PT symmetry breaking,” *Eur. Phys. J. Appl. Phys.* 63, 30001 (2013)
- [19]Huidan (Whitney) Yu, Xi Chen, Nan Chen, Yousheng Xu, and Yogesh N. Joglekar, “PT asymmetry in viscous fluids with balanced inflow and outflow” *Fluid Dynamics (physics.flu-dyn); Quantum Physics (quant-ph)*
- [20]C.M. Bender, B.K. Berntson, D. Parker, and E. Samuel, “Observation of  $\mathcal{PT}$  phase transition in a simple mechanical system,” *Am. J. Phys.* 81, 173 (2013).
- [21]A. V. Yulin and V. V. Konotop, “Conservative and  $\mathcal{PT}$ -symmetric compactons in waveguide networks,” *Optics Letters*, Vol. 38, Issue 22, pp. 4880-4883 (2013)
- [22]Andrey A. Sukhorukov, Sergey V. Dmitriev, Sergey V. Suchkov, and Yuri S. Kivshar, “Nonlocality in  $\mathcal{PT}$ -symmetric waveguide arrays with gain and loss,” *Optics Letters*, Vol. 37, Issue 11, pp. 2148-2150 (2012)
- [23]M. Raffel, C. Willert, S. Wereley and J. Kompenhans, “Particle Image Velocimetry- A practical guide (2nd edition),” Springer
- [24]Duo Xu and Jun Chen, “Accurate estimate of turbulent dissipation rate using PIV data,” *Experimental Thermal and Fluid Science* 44 (2013), 662672
- [25]Duo Xu and Jun Chen, “Experimental study of stratified jet by simultaneous measurements of velocity and density fields,” *Experiments in Fluids* 53 (2012), 145162
- [26]Duo Xu and Jun Chen, “Experimental test of revised similarity hypotheses without Taylors hypothesis,” *Physics Review E* 87 (Jan 2013), 013018
- [27]Duo Xu and Jun Chen, “EXPERIMENTAL STUDY OF SUB-GRID SCALE PHYSICS IN STRATIFIED FLOWS,” *Proceedings of ASME 2013 Fluids Engineering Summer*, Incline Village, Nevada, July 7-11, 2013
- [28]Reid Adam Berdanier, “DESIGN OF A MULTI-STAGE RESEARCH COMPRESSOR FOR CANTILEVERED STATOR HUB CLEARANCE FLOW INVESTIGATIONS,” Purdue University, West Lafayette, IN, MSME Thesis, 2012
- [29]Kimball A. Milton, E. K. Abalo, Prachi Parashar, Nima Pourtolami and J. Wagner, “ $\mathcal{PT}$ -Symmetric Quantum Electrodynamics and Unitarity,” *High Energy Physics - Theory (hep-th); Quantum Physics (quant-ph)*
- [30]Ali Mostafazadeh, “Comment on Complex Extension of Quantum Mechanics,” *Quantum Physics (quant-ph); High Energy Physics - Theory (hep-th); Mathematical Physics (math-ph)*
- [31]Philipp Ambichl, Konstantinos G. Makris, Li Ge, Yidong Chong, A. Douglas Stone and Stefan Rotter, “Breaking of  $\mathcal{PT}$ -symmetry in bounded and unbounded scattering systems,” *Physical Review X* 3, 041030 (2013)
- [32]Katherine Jones-Smith and Rudolph Kalveks, “Vector Models in PT Quantum Mechanics,” *Int. J. Theo. Phys.*, Jan 2013

- [33]Bhabani Prasad Mandal (BHU), Brijesh Kumar Mourya (BHU) and Rajesh Kumar Yadav (BHU), “ $\mathcal{PT}$  phase transition in higher-dimensional quantum systems,” *Physics Letters A* 377, 1043 (2013)
- [34]Daniel Leykam, Vladimir V. Konotop and Anton S. Desyatnikov, “Discrete vortex solitons and  $\mathcal{PT}$  symmetry,” *Opt. Lett.* 38, 371-373 (2013)
- [35]Tomaz Prosen, “ $\mathcal{PT}$ -symmetric quantum Liouvillian dynamics,” *Phys. Rev. Lett.* 109, 090404 (2012)
- [36]B.H. Bransden, C.J.Joachain and Longman, “Physics of Atoms and Molecules,” 1983
- [37]Carl M. Bender, “Making Sense of Non-Hermitian Hamiltonians,” *Rept.Prog.Phys* 70:947,2007
- [38]R. Shankar, “Principles of Quantum Mechanics,” (Springer, New York, 1994).
- [39]Matrox Imaging Company, “Matrox Imaging Library Version 9.0 with Processing Pack 1 User Guide,” *Manual No.Y10513-301-0910* July 29, 2009
- [40]Matrox Imaging Company, “Camera Interface Guide”
- [41]IO Industries, “*Flare<sup>TM</sup>* High-Speed CMOS Area Scan Camera Series 2M360 / 4M180 Camera Link User’s Manual Revision 1.0,” 2011
- [42]Matrox Imaging Company, “Matrox Intellicam version 8.0 User Guide,” *Manual no. 10521-301-0800* May 19, 2005
- [43]Matrox Imaging Company, “Matrox Solios eVCL Camera Interface Application Note,” May 9, 2011
- [44]Matrox Imaging Company, “Matrox Solios eV Installation and Hardware Reference,” *Manual no. Y11113-101-0100* July 13, 2009
- [45]LaVision Company, “ImagerPro Item-Number(s): 1101200, 1101201, 1101202 Product Manual,” May 8, 2008
- [46]LaVision Company, “Double-pulse Nd:YAG Item-Number(s): 1103031 Product Manual,” March 16, 2007
- [47]H Huang, D Dabiri and M Gharib “On errors of digital particle image velocimetry,” *Measurement Science and Technology* Volume 8 Number 12
- [48]Chen J, Meneveau C and Katz J, “Scale interactions of turbulence subjected to a straining-relaxation-destraining cycle,” *J Fluid Mech* 562:123150
- [49]Robert W. Fox, Philip J. Pritchard and Alan T. McDonald, “Introduction to fluid mechanics,” 7-th edition
- [50]Huidan (Whitney) Yu1, Xi Chen, Yousheng Xu, and Yogesh N. Joglekar, “Power-law scaling of asymmetries in viscous flow with  $\mathcal{PT}$  -symmetric inflow and outflow,” *physics.flu-dyn* Submitted on 19 Apr 2013.
- [51]R.J. Adrian, J. Westerweel, “Particle Image Velocimetry,” Cambridge University, 2010
- [52]X. Chen, H. Yu, J. Yogesh, Y. Zheng, Y. Xu, and F. Wu, “The influence of different driving patterns on parity time-reversal symmetry,” *Acta. Phys. Sin.*, 63(6) (2014) 060206

## APPENDIX

## Appendix

```

/*
 * File name: ContinuousPIVImageGrabbing.cpp
 */
#include <mil.h>
#include <iostream>
#include <conio.h>
#include <string>
using namespace std;

/* Number of images in the buffering grab queue.
   Generally, increasing this number gives better real-time
   grab.
 */
#define BUFFERING_SIZE_MAX 100

/* User's processing function prototype. */
MIL_INT MFTYPE ProcessingFunction(MIL_INT HookType, MIL_ID
    HookId,
                                void
                                MFTYPE
                                *
                                HookDataPtr
                                );

/* User's processing function hook data structure. */
typedef struct
{
    MIL_ID  MilImageDisp;
    MIL_INT ProcessedImageCount;
} HookDataStruct;

/* Main function. */

```



```

/* ----- */

int MosMain(void)
{
    MIL_ID MilApplication;
    MIL_ID MilSystem      ;
    MIL_ID MilDigitizer   ;
    MIL_ID MilDisplay     ;
    MIL_ID MilImageDisp   ;
    MIL_ID MilGrabBufferList [BUFFERING_SIZE_MAX] = { 0 };
    MIL_INT MilGrabBufferListSize;
    MIL_INT ProcessFrameCount = 0, ProcessFrameMissed = 0,
        ProcessFrameCorrupted = 0;
    MIL_INT NbFrames          = 0, Selection=1, n=0;
    MIL_DOUBLE ProcessFrameRate= 0;
    HookDataStruct UserHookData;

    /* Allocate defaults. */
    MappAllocDefault (MSETUP, &MilApplication, &MilSystem, &
        MilDisplay,
                                &MilDigitizer,
                                &
                                MilImageDisp
        );

    /* Allocate the grab buffers and clear them. */
    MappControl(MERROR, M_PRINT_DISABLE);

    for (MilGrabBufferListSize = 0;
        MilGrabBufferListSize < BUFFERING_SIZE_MAX;
        MilGrabBufferListSize++)
    {
        MbufAllocColor (MilSystem,
                        MdigInquire (MilDigitizer,
                                    M_SIZE_BAND, M_NULL),
                        MdigInquire (MilDigitizer, M_SIZE_X, M_NULL)
                        ,
                        MdigInquire (MilDigitizer, M_SIZE_Y, M_NULL)
                        ,
                        M_DEF_IMAGE_TYPE,
                        M_IMAGE+M_GRAB+M_PROC,
                        &MilGrabBufferList [MilGrabBufferListSize] );
    }
}

```

```

    if (MilGrabBufferList [ MilGrabBufferListSize ])
        {
            MbufClear( MilGrabBufferList [ MilGrabBufferListSize ],
                0xFF);
        }
    else
        break;
}
MapControl(MERROR, MPRINT_ENABLE);

/* Free buffers to leave space for possible temporary
   buffers. */
for (n=0; n<2 && MilGrabBufferListSize; n++)
    {
        MilGrabBufferListSize--;
        MbufFree( MilGrabBufferList [ MilGrabBufferListSize ] );
    }

/* Grab continuously on the display and wait for a key
   press. */
MdigGrabContinuous( MilDigitizer , MilImageDisp);

/* Print a message. */
MosPrintf(MIL_TEXT("\nMULTIPLE_BUFFERED_PROCESSING.\n"));
MosPrintf(MIL_TEXT("-----\n\n"));

/* Halt continuous grab. */
MdigHalt( MilDigitizer );

/* Initialize the User's processing function data
   structure. */
UserHookData.MilImageDisp          = MilImageDisp;
UserHookData.ProcessedImageCount = 0;

/* Start the processing. The processing function is called
   for every frame grabbed. */
MdigProcess( MilDigitizer , MilGrabBufferList ,
    MilGrabBufferListSize ,
    MSEQUENCE, MDEFAULT,
    ProcessingFunction , &
    UserHookData);

```

```

/* NOTE: Now the main() is free to perform other tasks
                                                while the
                                                processing
                                                is
                                                executing
                                                . */

/* Print a message and wait for a key press after a
   minimum number of frames. */
MosPrintf(MIL_TEXT(" Press <Enter> to stop.\n\n"));
MosGetch();

/* Print statistics. */
MdigInquire( MilDigitizer , MPROCESS_FRAME_COUNT, &
             ProcessFrameCount);
MdigInquire( MilDigitizer , MPROCESS_FRAME_RATE, &
             ProcessFrameRate);
MdigInquire( MilDigitizer , MPROCESS_FRAME_MISSED, &
             ProcessFrameMissed);
MdigInquire( MilDigitizer , MPROCESS_FRAME_CORRUPTED, &
             ProcessFrameCorrupted);
MosPrintf(MIL_TEXT("\n\n%d frames grabbed at %.1f frames/
                  sec (%.1f ms/frame).\n"),
          ProcessFrameCount, ProcessFrameRate
          , 1000.0/ProcessFrameRate);
MosPrintf(MIL_TEXT("%d frames missed.\n"),
          ProcessFrameMissed);
MosPrintf(MIL_TEXT("%d frames corrupted.\n"),
          ProcessFrameCorrupted);
MosPrintf(MIL_TEXT(" Press <Enter> to end.\n\n"));
MosGetch();

/* Free the grab buffers. */
while( MilGrabBufferListSize > 0)
    MbufFree( MilGrabBufferList[--MilGrabBufferListSize] );

/* Release defaults. */

```

```

MappFreeDefault(MilApplication , MilSystem , MilDisplay ,
    MilDigitizer , MilImageDisp);

    return 0;
}

/* User's processing function called every time a grab buffer
   is modified. */

/* Local defines. */
#define STRING_LENGTH_MAX    20
#define STRING_POS_X        20
#define STRING_POS_Y        20

MIL_INT MFTYPE ProcessingFunction(MIL_INT HookType, MIL_ID
    HookId ,

                                void
                                MPTYPE
                                *
                                HookDataPtr
                                )
{
    HookDataStruct *UserHookDataPtr = (HookDataStruct *)
        HookDataPtr;

    MIL_ID ModifiedBufferId;
    MIL_TEXT_CHAR Text [STRING_LENGTH_MAX]= {MIL_TEXT( '\0' ) ,};
    MIL_TEXT_CHAR junkoutput [STRING_LENGTH_MAX]= {MIL_TEXT( '\0
        ' ) ,};

    /* Retrieve the MIL_ID of the grabbed buffer. */
    MdigGetHookInfo(HookId , M_MODIFIED_BUFFER+M_BUFFER_ID, &
        ModifiedBufferId);

    /* Print and draw the frame count. */
    UserHookDataPtr->ProcessedImageCount++;
    MosPrintf(MIL_TEXT(" Processing _frame _##%d.\r" ) ,
        UserHookDataPtr->ProcessedImageCount);
    MosPrintf(Text , STRING_LENGTH_MAX, MIL_TEXT("%ld" ) ,
        UserHookDataPtr->
            ProcessedImageCount
        );
}

```

```
MgraText(MDEFAULT, ModifiedBufferId , STRING_POS_X,  
         STRING_POS_Y, Text);  
  
/* Perform the processing and update the display. */  
MbufCopy(ModifiedBufferId , UserHookDataPtr->MilImageDisp);  
  
/* Create file name base on the index of the frame that is  
   being processed*/  
MosPrintf(Text , STRING_LENGTH_MAX, MIL_TEXT(" Image%d.tif  
"),  
          UserHookDataPtr->  
          ProcessedImageCount  
          );  
  
/* Save image to disk */  
MbufSave(Text , UserHookDataPtr->MilImageDisp);  
  
return 0;  
}
```